COHERENT CONTROL OF ELECTRON SPINS

IN SEMICONDUCTOR QUANTUM WELLS

by

TIMOTHY MICHAEL SWEENEY

A DISSERTATION

Presented to the Department of Physics
and the Graduate School of the University of Oregon
in partial fulfillment of the requirements
for the degree of
Doctor of Philosophy

September 2011

DISSERTATION APPROVAL PAGE

Student: Timothy Michael Sweeney

Title: Coherent Control of Electron Spins in Semiconductor Quantum Wells

This dissertation has been accepted and approved in partial fulfillment of the requirements for the Doctor of Philosophy degree in the Department of Physics by:

Dr. Miriam Deutsch	Chairperson
Dr. Hailin Wang	Advisor
Dr. Steven van Enk	Member
Dr. Raghuveer Parthasarathy	Member
Dr. Catherine Page	Outside Member

and

Kimberly Andrews Espy   Vice President for Research and Innovation/Dean of the Graduate School

Original approval signatures are on file with the University of Oregon Graduate School.

Degree awarded September 2011

DISSERTATION ABSTRACT

Timothy Michael Sweeney

Doctor of Philosophy

Department of Physics

September 2011

Title: Coherent Control of Electron Spins in Semiconductor Quantum Wells

Approved: _____
                        Dr. Hailin Wang

      Electron spin states in semiconductors feature long coherence lifetimes, which
have stimulated intense interest in the use of these spins for applications in spin based
electronics and quantum information processing (QIP). A principal requirement for these
spins to be viable candidates in QIP is the ability to coherently control the spins on
timescales much faster than the decoherence times. The ability to optically control the
spin state can meet this requirement. The spin states of electrons exhibit strong radiative
coupling to negatively charged exciton (trion) states, and this radiative coupling makes
coherent optical control of spin states possible.

      This dissertation presents experimental demonstration of coherent control of an
electron spin ensemble in a two-dimensional electron gas in a CdTe quantum well. We
present two complimentary techniques to optically manipulate these electron spins using
a Raman transition. The first demonstration is with a single off-resonant ultrafast optical
pulse. This ultrafast pulse acts like an effective magnetic field in the propagation
direction of the optical pulse. The second experiment utilizes phase-locked Raman
resonant pulse pairs to coherently rotate the quantum state, where the relative phase of

the pulse pair sets the axis of rotation. The Raman pulse pair acts like a microwave field driving the spin states.

This research demonstrates two significant contributions to the field of coherent optical interactions with semiconductors. First, we have advanced the potential use of electron spin ensembles in semiconductors for optics based quantum information processing hardware through our demonstration of coherent spin flips and complete coherent control. Second, we have experimentally realized full coherent control through the use of phase-locked Raman pulse pairs that overcomes inherent limitations of the single-pulse optical rotation technique, which is the current standard technique used in coherent control.

This dissertation includes previously published and unpublished co-authored material.

CURRICULUM VITAE

NAME OF AUTHOR: Timothy Michael Sweeney

GRADUATE AND UNDERGRADUATE SCHOOLS ATTENDED:

University of Oregon, Eugene
University of New Orleans, New Orleans, Louisiana
Chico State University, Chico, California

DEGREES AWARDED:

Doctor of Philosophy in Physics, 2011, University of Oregon
Master of Science in Physics, 2004, University of New Orleans
Bachelor of Science in Physics, 2003, Chico State University

PROFESSIONAL EXPERIENCE:

Graduate Teaching Fellow, Department of Physics, University of Oregon,
    Eugene, 2005-2011

National Science Foundation GK-12 Fellow, University of Oregon,
    Eugene 2007-2010

GRANTS, AWARDS, AND HONORS:

National Science Foundation GK-12 Fellow, 2006-2008

National Science Foundation STEP Mentoring Fellow, 2007 and 2010

PUBLICATIONS:

T. M. Sweeney, C. Phelps, H. Wang, "Quantum control of electron spins in the two-dimensional electron gas of a CdTe quantum well with a pair of Raman-resonant phase-locked laser pulses," *Physical Review B,* (Accepted July, 2011).

T. M. Sweeney, H. Wang, "Quantum Control of Electron Spins in Semiconductors with Phase-Locked Raman Pulse Pairs," *CLEO/QELS*, *OSA Technical Digest CD*, 2011, paper: QTuO3

G.D. Metcalfe, G.A. Garrett, P. Rotella, A.V. Sampath, J. Wright, H. Shen, M. Wraback, **T.M. Sweeney**, H. Wang, "UV Pump-THz Probe Study of Mechanisms Limiting Luminescence from Nanoscale Compositionally Inhomogenous AlGaN," *CLEO/QELS*, *OSA Technical Digest CD*, 2011, paper JTuB3

T. Sweeney, T. Baldwin, and H. Wang, "Probing Heavy-Hole and Light-Hole Excitonic Beats in a GaAs Quantum well with Phase-Locked Raman Pulse Pairs," *CLEO/QELS, OSA Technical Digest CD*, 2010, paper QFI4.

C. Phelps, **T. Sweeney**, and H. Wang, "Ultrafast Coherent Electron Spin Flip in a 2-D Electron Gas," *CLEO/QELS, OSA Technical Digest CD*, 2009, paper JTuC3.

Phelps, C.**, T. Sweeney**, R. T. Cox , H. L. Wang "Ultrafast Coherent Electron Spin Flip in a Modulation-Doped CdTe Quantum Well," *Physical Review Letters,* 102**,** 4 (2009).

Shen, Y., **T. M. Sweeney**, H. Wang, "Zero-phonon linewidth of single nitrogen vacancy centers in diamond nanocrystals," *Physical Review B,* 77**,** 3 (2008).

ACKNOWLEDGMENTS

There have been several key people at the University of Oregon who have molded me into the scientist I have become. I would first like to thank my advisor, Hailin Wang, for the opportunity to pursue the research presented in this dissertation. I am thankful for the trust, guidance, and freedom I was given to explore the physics I found interesting. I am indebted to my dissertation chair Miriam Deutsch for the insight and openness she has shown me, and for her willingness to critique and guide my professional development.

I would like to thank the past and present members of the Wang Lab who I've had the pleasure to get to know. These individuals have made the group a delightful, stimulating, and cooperative place to do science: Tom Baldwin, Nima Dinyari, Shannon O'Leary, Young-Shin Park, Yumin Shen, Yan Guo, Mats Larsson, Victor Fiore, Russell Barbour, Thein Oo, Andrew Cook, Andrew Golter, and Yong Yang.

I am thankful for the ideas Carey Phelps has shared, and for his work on the experiments presented in Chapters V and VI. I would also like to acknowledge Hayden McGuinness for his physical insight and friendship. Carey and Hayden are two brilliant scientists and people who have thoroughly enriched my life. They are truly curious about the world we live in, and have always been willing to talk about challenges and concepts associated with my research.

Finally I would like to thank my friends, my parents, and my sisters and their families for their support.

TABLE OF CONTENTS

CHAPTER I

INTRODUCTION

A particularly powerful optical process at the heart of many active areas of research from biology (*1, 2*), to chemistry (*3, 4*), to physics (*5-9*) began with an optics experiment in 1928 (*10*), at the University of Calcutta. The experiment showed that light, when passing through a sample liquid, can be shifted in frequency as a result of inelastic scattering. This previously unknown mechanism for light scattering was soon named the "Raman effect" after the experimentalist, Sir C. V. Raman, who was awarded the Nobel Prize for his discovery in 1930. At the root of the Raman effect is a two-photon, or "Raman," transition between two states that are not directly coupled via a dipole optical transition.

The Λ-type three-level system shown in Figure 1.1, where the three energy levels are labeled $|0\rangle$, $|1\rangle$ and $|e\rangle$, illustrates a Raman transition. Transitions to the excited state $|e\rangle$ from either of the ground states ($|0\rangle$ or $|1\rangle$) are dipole-allowed. The transition between $|0\rangle$ and $|1\rangle$, however, is dipole forbidden. Instead, states $|0\rangle$ and $|1\rangle$ are coupled via a two-
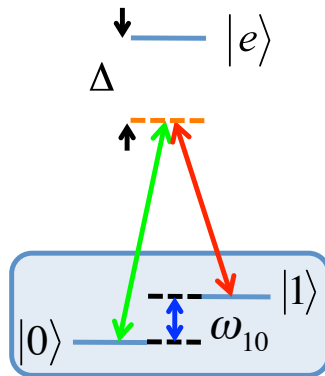
Figure 1.1. An energy level diagram for a three-level Λ-type system with highlighted ground states responsible for Raman coherence.

photon transition through radiative coupling to a common excited state. The Raman

transition can be driven resonantly when the frequency difference between two driving

fields matches the energy difference of the lower states, as illustrated in Figure 1.1. By

using two Raman-resonant laser beams, one can transfer populations between dipole-

forbidden states and establish coherent superpositions known as Raman coherences. It is

often the case that the exploitation of off-resonant coupling to the excited state is most

beneficial, as it avoids decoherences associated with populating the real excited state $|e\rangle$.

Figure 1.1 illustrates resonant Raman coupling, with off-resonant dipole coupling to the

excited state.

1.1. Raman Coherences: Applications and Processes

Raman coherences have been exploited in a number of different physical systems.

Examples include the vibrational states of molecules, the electronic states of atoms, as well

as spin states in semiconductors. Exploitation of these coherences has resulted in various

applications, such as powerful biological imaging techniques (*1, 2*) and proposals toward

quantum information processing (QIP) (*11-17*). In optical imaging based on Coherent anti-

Stokes Raman spectroscopy (CARS) (*1*), the beat frequency of two lasers is used to drive

coherent superpositions of vibrational states in Raman-active molecules in biological

systems. Inelastic scattering of the laser light by the molecules results in coherent scatter of

light that is frequency shifted by the frequency of the molecular vibration. Collecting only

the most blue anti-Stokes photons, one can generate 3-dimensional images of the density

distribution of particular molecules found throughout a biological organism (*1*).

In QIP, Raman coherences can be used for the storage, manipulation, and retrieval

of quantum information. Quantum information can be stored as a coherent superposition of a two-level system, or qubit. The two lower state of a Λ-system can serve as a qubit. A particular benefit of Λ-type systems is that non-radiative Raman coherence can far out live two-level systems that are coupled via dipole optical transitions. For example, a Raman coherence in trapped ions can last for as long as 15 seconds (*18*) before it is lost, which is 7 orders of magnitude longer than a typical radiative coherence. For these long-lived coherences to be useful in QIP, it is necessary to implement full quantum control by exploiting the Raman transition, which is the primary focus of this dissertation.

1.2. Raman Coherence and Electron Spins in Semiconductors

This dissertation centers on the study of coherent optical processes of Raman coherence in semiconductors, more specifically Raman coherence associated with electron spin coherence. The optical processes responsible for interacting with electron spins result from band edge optical excitations in semiconductors that are characterized by excitons. An exciton is a Hydrogen-like bound state of an electron in the conduction band and a hole in the valence band. An exciton can be bound to an excess electron or hole, forming a charged exciton, or trion. In a semiconductor with an excess electron population, these electrons can be radiatively coupled to a (negatively-charged) trion state. The dipole optical transitions involved are specific to the spin states of the excess electron population. The radiative coupling of electron spins to an excited state can result in a Λ-type three-level system, similar to Figure 1.1, in which the spin state forms the two ground states and the trion state is the excited state. The resulting Λ-type system can then be used for the study of Raman coherence (*15-17*). The Raman coherence in this context is the electron spin

coherence.

Most forms of quantum coherences (i.e. superposition of quantum states) in semiconductors are fragile because of the interactions of the quantum states with the surrounding semiconductor environment (*19*), which result in coherence times on the order of picoseconds. In contrast, the spins of electrons in the conduction band of a semiconductors are only weakly coupled to the semiconductor environment, which leads to coherence times on the order of nanoseconds or longer (*20*). The dominant mechanism for the spin decoherence is the relatively weak coupling of electron spins to nuclear spins. Recent work to negate the decoherence effects of electron spins coupling to nuclear spins has resulted in coherence times extendable to 3 microseconds in modest magnetic fields (*21, 22*), and 0.3 seconds in the absence of an external magnetic field (*23*).

The long lifetime of electron spin coherence in semiconductors has stimulated intense interest in exploiting electron spins for applications in spin-based electronic or photonic devices as well as QIP (*24-27*). The spin of a single electron could be used as a stationary qubit for a quantum computer (*27*). Spin ensembles can also play an important role for information storage in a distributed quantum network (*28*). Other uses for spins and spin ensembles in QIP include quantum repeaters and the generation of entangled photon pairs (*13, 29*). Central to the goal of using electron spins in QIP is the ability to initialize and control electron spins.

Recently, significant advances have been made toward the optical initialization of the electron spins to a fiduciary state, with state preparation efficiency of (98.9+/- 0.4) % (*30*). However, the ability to control spins has proven to be more challenging. In early studies (2001) researchers had initially attempted to rotate the polarization of electron spin

4

ensemble systems using optical pulses (*31*). However, only partial rotations of spin

polarization had been observed, while complete control had remained elusive. The

principal limitation in the ability to control spins optically was the high degree of

decoherence induced by the optical excitation (*31*).

While optical control of electron spins posed a significant hurdle, researchers in

2005 were able to bypass the optical control approach and manipulate an electron spin in a

more direct manner (*32*). They fabricated a gate-defined double quantum dot, with one

electron confined to each dot. The control of one electron spin was obtained through

exchange interactions with the spin of the electron in the neighboring gate-defined dot.

Within the next year the same group used a radio frequency pulse to drive the

electron spin directly (*33*), arguably the most straightforward approach to control a two-

level system. For this experiment, a magnetic field was used to impart an energy, or

"Zeeman," splitting between the two spin states, and a radio frequency (RF) pulse was

tuned into resonance with the Zeeman splitting. Complete control of the spin state was

obtained by way of control over the phase and the area of the RF pulse. The control of the

electron spins in gate-defined quantum dot research is limited by conventional electronics

that result in control times on the order of a nanosecond (*32-34*). The relatively slow

control times, when compared to the spin coherence time, result in a maximum of $\sim 10^3$

operations before the spin decoheres. This ratio is not sufficient to perform the large

number of quantum gates required for reasonably complex quantum algorithms.

The ability to coherently control the state of the spins in timescales much shorter

than the decoherence time is imperative to using these spins for QIP. Recent theoretical

proposals have suggested the use of ultrafast optical pulses to control spins, which could

conduct ~10^5 operations within the decoherence time of an electron spin (*15-17*). These

proposals exploit a Raman transition, in which the two spin states of an electron couple to a

charged exciton state, via dipole-allowed optical transitions. Coherent rotations with

optical pulses can take advantage of ultrafast laser technology, thus performing control

rotations on time scales several orders of magnitude faster than those achieved with

conventional electronics. A second and equally valuable advantage to optically addressing

the electron spins is the potential for coherent exchange of a matter qubit state with a

photon state, which is important for the use of these spins in quantum networks (*12, 13, 29*)

and in some quantum computation protocols (*35*).

Significant progress has been made within the last several years (2008-present)

toward using a single ultrafast optical pulse to control electron spins, following the

proposed technique by Economou, et al. (*15*). Examples of this progress include complete

control of a single electron spin (*36*), electron spin echoes in a single charged quantum dot

(*22*) and an ensemble of singly charged quantum dots (*37*), and the ultrafast control of

entanglement between electron spins in an InAs quantum dot molecule (*38*). These

demonstrations have firmly placed electron spins in semiconductors as potential candidates

for spin-based devices and for QIP.

The fidelity obtained in studies using the single-pulse control technique in InAs

quantum dots is ~90% for a π pulse (*36*), which is far from what is required to maintain

coherence over ~10^5 operations. The degradation of the fidelity is, to large extent, due to

unintended excitations induced by the strong ultrafast optical control pulses. These

excitations can not only complicate the coherent spin rotation process, but they can also

lead to excessive decoherence. Optical control techniques such as the phase-locked pulse

pair approach, which drive the Raman transition resonantly (*16, 17*), can minimize or circumvent these unintended excitations, leading to improved fidelity for optical spin control.

1.3. Dissertation Outline

The research presented in this dissertation demonstrates optical control of an ensemble of electron spins in a semiconductor using two different but closely related approaches (*15-17*). For the first approach, we used an ultrafast optical pulse that featured a spectral bandwidth large compared to the electron Zeeman splitting, to impulsively drive the Raman transition associated with the electron spins. The ultrafast optical pulse induces an additional energy splitting between the two electron spin states, thus acting like an effective magnetic field along the propagation direction of the optical pulse. The optical pulse generates a coherent spin rotation about the optical axis (*15, 39*). This technique is similar to that used in the InAs quantum dot experiments discussed above.

For the second approach, we used a pair of phase-locked laser pulses to resonantly drive the Raman transition. In this approach, a Raman-resonant pulse pair acts like an effective radio frequency field with a phase determined by the relative optical phase of the pulse pair, mapping the relative optical phase directly onto the phase of the electron spin polarization. The relative initial phase of the pulse pair sets the axis of rotation, and the effective pulse area determines the angle of rotation. Arbitrary spin rotation can thus be realized with this approach. Our work represents the first experimental demonstration of optical spin control with phase-locked Raman pulse pairs.

Among various semiconductor spin systems, optical spin control in two-

dimensional electron gases (2DEGs) is especially challenging. 2DEGs do not feature atomic-like, spectrally sharp optical transitions such as those in epitaxially-grown quantum dots. In addition to the rapid decoherence associated with relevant dipole optical transitions, coherent optical processes in 2DEGs are also complicated by inherent manybody interactions between optical excitations. In this regard, the successful experimental demonstration of optical spin control in a 2DEG indicates the feasibility of extending optical spin control to most semiconductor systems, including gate-defined quantum dots that do not feature atomic-like optical transitions. We have thus chosen to explore optical spin control in a 2DEG formed in a modulation-doped quantum well. For a proof-of-principle demonstration, we have used CdTe quantum wells because optical transitions in CdTe quantum wells are accessible with the ultrafast Ti:Sapphire laser system in our laboratory and also because of the availability of high quality modulation-doped CdTe samples.

In addition to the experimental studies, we have also developed a detailed theoretical model for optical spin control based on the use of the optical Bloch equations. The experimental results are in good agreement with the theoretical calculations.

This dissertation is organized as follows. Chapter II discusses fundamentals of optical interactions in a direct band gap semiconductor -including band structures, excitons, and trions -and introduces the optical polarization selection rules that lead to a three-level Λ-type system for the electron spin states.

Chapter III develops the theoretical description of optical spin control using the optical Bloch equations (OBE). The three-level Λ-type system is reduced to an effective two-level system in the limit of the adiabatic approximation. This chapter also presents the

detailed physical processes and mechanisms for optical spin control based on a single off-resonant laser pulse and on a pair of Raman resonant laser pulses.

Chapter IV describes in detail pertinent experimental setups and techniques, including the detection of electron spin orientation with a transient pump-probe technique and the generation of phase-locked laser pulse pairs with an optical pulse-shaper based on the use of a liquid-crystal spatial light modulator. Optical pulse-shaping techniques are also analyzed in the context of a time-invariant linear filtering process.

Some of the research presented in Chapter V has been published *(39)* and was co-authored by Carey Phelps. Chapter V presents the experimental realization of optical spin rotations of electron spins in a 2DEG with the use of a single off-resonant ultrafast laser pulse. Complete electron spin flips are demonstrated via a comparison of coherent spin dynamics before and after the arrival of the control pulse. Detailed comparisons between the experimental results and theoretical calculations are also discussed.

Some of the research presented in Chapter VI was co-authored by Carey Phelps. Chapter VI presents the experimental realization of optical spin control of electrons in a 2DEG with the use of a pair of phase-locked Raman-resonant laser pulses. In contrast to single-pulse optical spin control, which features a fixed spin-rotation axis, manipulation of the initial relative phase of the pulse pair enables us to control the axis of the optical spin rotation. The Raman pulse pair maps the relative optical phase onto the phase of the electron spin polarization, making ultrafast, all-optical, and full quantum control of the electron spins possible. Detailed comparison between the experimental results and the theoretical calculations highlights several special features of the Raman pulse pair approach.

Chapter VII summarizes the research described in this dissertation and proposes a future project using chirped optical pulses to enhance control fidelity. It also discusses an extension of this work for applications in cavity QED, which can enable the coherent coupling between distant electron spins, is also discussed.

CHAPTER II

OPTICAL EXCITATIONS IN SEMICONDUCTORS: FUNDAMENTALS

The radiative coupling of electron spins to an excited state allows for coherent manipulation of spins via a Raman transition. To better understand the physical environment and optical processes associated with electron spin coherence we discuss the fundamentals of optical interactions in a direct band gap semiconductor.

We begin with a description of the semiconductor band gap, followed by the band structure. From the band structure we discuss optical excitations that lead to the creation of electrons and holes. We discuss two static interactions that alter the energy eigenstates of electrons and holes: one is confinement and the other is a magnetic field. We present the formation of bound states called excitons and trions, including the optical polarization selection rules associated with their optical excitation. We end the chapter with a description of how a three-level Λ-type system for the electron spin states is established with the aid of a magnetic field.

Please note: *Only* in Sections 2.2-2.4, in the development of optical interactions with semiconductors, do we follow the conventional method for labeling the optic axis and growth axis as the z-axis. In the *rest* of this dissertation we define the optic axis and growth axis as the x-axis because the eigenstates of interest, the electron spin states, are perpendicular to the optic axis with a transverse magnetic field present. Therefore, we define the z-axis to be in the plane of the sample, and the optic axis is defined as the x-axis, as illustrated in Figure 2.6.

2.1. Band Gap

The energy band gap is crucial to a theoretical description of semiconductors because it differentiates insulators and semiconductors from metals. Energy bands arise from the overlap of electronic states for a large number (10^{20}) of atoms, and gaps between allowed energy bands are called band gaps. To understand the behavior of a large number of atoms in a solid, we begin with the electronic structure of an individual, isolated, atom. A single atom will have allowed atomic orbitals, which form discrete energy levels. One such level is diagrammed in Figure 2.1a. When two atoms are brought together to form a molecule, each allowed energy level splits. Each additional atom to the molecule will contribute another allowed energy level; therefore, the total number of allowed energy levels will be equal to the total number of atoms. In the case of a solid where the number of atoms brought together is on the order of Avogadro's number, the very large number of energy levels becomes densely packed into a finite window of allowed energies. This dense packing effectively merges to form continuous bands of allowed energies, rather than the discrete energy levels observed for atoms and molecules. This is illustrated in Figure 2.1b.

Depending on the particular atoms that are brought together to form a solid, allowed energy bands may overlap or may be separated by energy band gaps. In semiconductors and insulators, electrons are confined to a number of allowed bands of energy and forbidden from other energy regions, as shown in Figure 2.1c. The term "band gap" refers to the energy difference between two allowed energy bands, typically the valence band and the conduction band. The structure of these bands determines to a large extent the optical and electronic properties of a semiconductor.
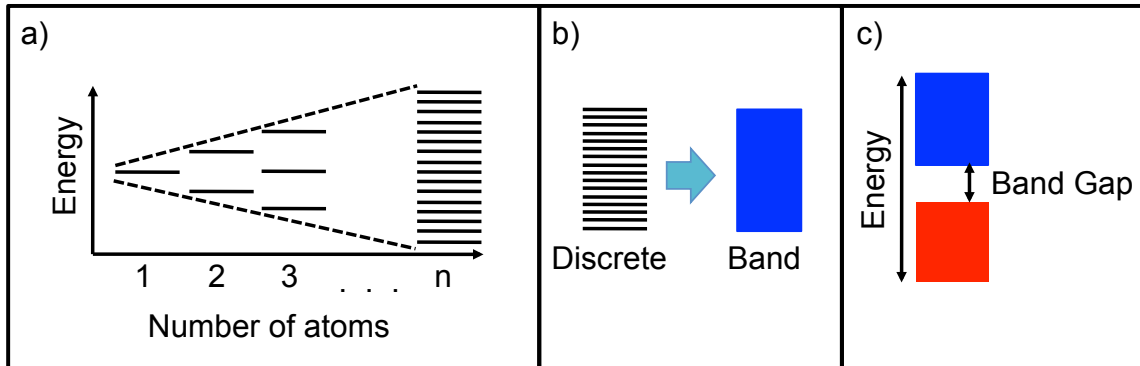
Figure 2.1. The transformation from discrete energy levels to a continuum of states is shown in (a). With an increased number of atoms, the number of allowed energy states becomes densely packed into a finite window of allowed energies until the discrete energy states merge into a band of states, as diagrammed in (b). Semiconductors and insulators have bands of electronic energy states that are forbidden, called band gaps shown, in figure (c).

2.2. Band Structure

To understand the optical properties of semiconductors, one must know the electronic structure and wave functions for the various bands. Optical transitions near band edges in direct band gap materials are predominately used in optical devices and are of particular interest to this dissertation. An example of the band structure for a direct band gap semiconductor, CdTe, is shown in Figure 2.2, where the blue line indicates the conduction band of CdTe, and the red curves are the heavy- and light-hole valence bands. An extremely useful method for modeling the band structure bands is the **k·p** method.

13
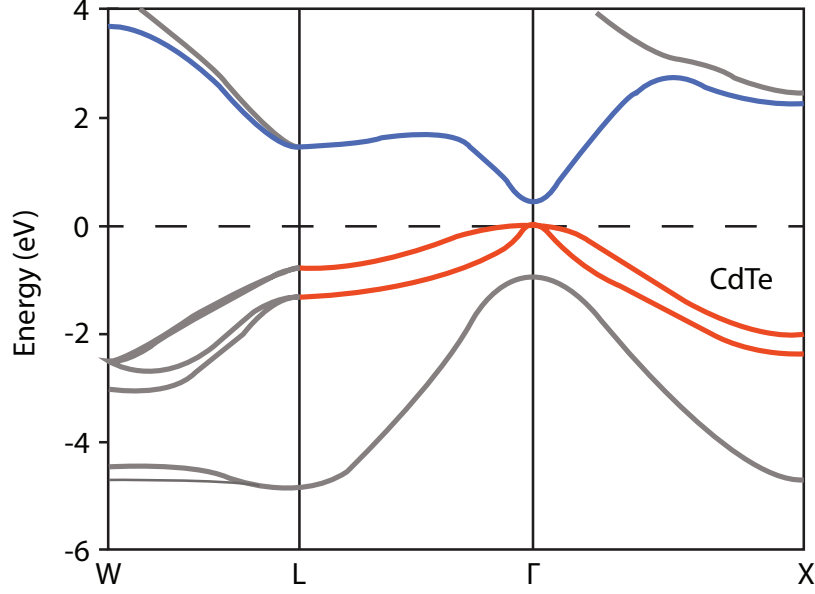
Figure 2.2. The band structure for CdTe. Direct band gap transitions of interest occur at the Γ-point.

2.2.1. Band Structure: **k•p** Method

The **k•p** method is developed from the Schrödinger equation of a single electron in a periodic potential

$$V(\vec{r}) = V(\vec{r} + \vec{R}),$$ (2.1)

which is invariant under crystal translation. Hence, $\vec{R}$ is an integer distance between lattice sites inside the crystal. The Schrödinger equation for the single electron is then given by

$$H\psi(\vec{r}) = \left(\frac{\hbar^2}{2m_0}\nabla^2 + V(\vec{r})\right)\psi(\vec{r}) = E(\vec{k})\psi(\vec{r}).$$ (2.2)

The general solution for the above Hamiltonian with a periodic potential is given by the Bloch wave function

$$\psi_{n\vec{k}}(\vec{r}) = e^{i\vec{k}\cdot\vec{r}}u_{n\vec{k}}(\vec{r}),$$ (2.3)

where $u_{n\vec{k}}(\vec{r}) = u_{n\vec{k}}(\vec{r} + \vec{R})$ is a periodic wavefunction. Plugging the Bloch wave function

(2.3) into the Schrödinger equation (2.2), one can arrive at the equation in which the **k•p** method begins, namely

$$\left(\frac{p^2}{2m_0} + \frac{\hbar}{m_0} \vec{k} \bullet \vec{p} + V(\vec{r}) \right) u_{n\vec{k}}(\vec{r}) = \left(E(\vec{k}) - \frac{\hbar^2 k^2}{2m_0} \right) u_{n\vec{k}}(\vec{r}) .$$ (2.4)

For a full description of the bands, numerical solutions to equation 2.4 are required to calculate the general energy band along the different $\vec{k}$ directions. Our research focuses on dynamics near small values of $\vec{k}$ near $\vec{k} = 0$, the Γ point, shown in Figure 2.2. Assuming that Bloch wave equations and energies for bands at $\vec{k} = 0$ are known, we can treat the terms $\frac{\hbar}{m_0} \vec{k} \bullet \vec{p}$ and $\frac{\hbar^2 k^2}{2m_0}$ as perturbations in either degenerate or non-degenerate perturbation theory to calculate the wave equations and energies near $\vec{k} = 0$. In general, the **k•p** method can be applied to calculate the band dispersion near any point $\vec{k} = \vec{k}_0$ by doing a perturbative expansion around $\vec{k}_0$, provided that the wave functions and the energies at $\vec{k}_0$ are known.

Calculations of the conduction band dispersion near the Γ point can be performed in a fairly straightforward manner using the **k•p** method. By exploiting symmetry properties of the conduction band near $\vec{k} = 0$, the energy dispersion calculated in the **k•p** method to second order in k is

$$E_c(\vec{k}) = E_g - \frac{\hbar^2 k^2}{2m_e^*} ,$$ (2.5)

where m_e^* is the effective mass of the electron and E_g is the energy band gap. The effective mass is given by

$$m_e^* \approx E_g \frac{m_0^2}{2P^2} , \qquad\qquad (2.6)$$

where m_0 is the electron mass and

$$P = -i \frac{\hbar}{m_0} \langle c | p_z | v \rangle \qquad\qquad (2.7)$$

is the Kane's parameter, which is the momentum matrix element between the conduction band, c, and the valence band, v. The fact the P is nearly identical for group IV, III-V, and II-VI materials results in a useful ratio for calculation the effective mass of conduction band electrons: $\frac{2P^2}{m_0} \approx 20 meV$.

2.2.2. Band Structure: Kane's Model

In order to describe the valence bands of a direct band gap semiconductor, it is imperative to account for the effects of spin-orbit coupling. The spin-orbit interaction is a result of torque exerted on the spin of the electron by a magnetic field generated by a positively charged nucleus, as viewed from the rest frame of the electron.

The Kane's model for calculating band structure incorporates the spin orbit interaction into the **k•p** method. One simply adds the spin orbit interaction Hamiltonian

$$H_{SO} = \frac{\hbar}{4m_0^2 c^2} (\nabla V \times \vec{p}) \bullet \sigma , \qquad\qquad (2.8)$$

where σ is the Pauli-spin matrix, to the Schrödinger equation (2.4). Then one uses the interaction Hamiltonian

$$H_{int} = \frac{\hbar}{m_0} \vec{k} \bullet \vec{p} + \frac{\hbar}{4m_0^2 c^2} \nabla V \times \vec{p} \bullet \sigma , \qquad\qquad (2.9)$$

as a perturbation.

The wave functions that are used as basis functions in the Kane's model are based on atomic *s*-like and *p*-like wave functions. In addition to orbital angular momentum, the spin angular momentum of charges in the conduction and valence bands must also be taken into account. The basis functions are chosen as

$$\left| iS \downarrow \right\rangle, \left| \frac{X - iY}{\sqrt{2}} \uparrow \right\rangle, \left| Z \downarrow \right\rangle, \left| -\frac{X + iY}{\sqrt{2}} \uparrow \right\rangle \tag{2.10}$$

and $\quad \left| iS \uparrow \right\rangle, \left| -\frac{X + iY}{\sqrt{2}} \downarrow \right\rangle, \left| Z \uparrow \right\rangle, \left| \frac{X - iY}{\sqrt{2}} \downarrow \right\rangle,$ (2.11)

where the first term is the conduction band state (s-like), followed by the three p-like valance band states, represented in terms of spherical harmonics. The eigen energies for the unperturbed Hamiltonian,

$$H_0 = \frac{p^2}{2m_0} + V(\vec{r}), \tag{2.12}$$

are degenerate for the two conduction band states, and are six fold degenerate for the valence band states. We use these basis functions to obtain the matrix elements to the interaction Hamiltonian (2.9), and thus to obtain the energy and wave function corrections. After diagonalizing the resultant Hamiltonian to obtain the new eigen energies for the bands, we find that the spin-orbit coupling term results in an energy offset, $-\Delta$, for the split off band.

The energy dispersion calculated from the **k•p** method, with spin orbit coupling included, is summarized below:

Conduction band:
$$E_c(k) = E_g + \frac{\hbar^2 k^2}{2m_e^*}$$
(2.13)

Heavy-hole band:
$$E_{hh}(k) = -\frac{\hbar^2 k^2}{2m_{hh}^*}$$
(2.14)

Light-hole band:
$$E_{lh}(k) = \frac{\hbar^2 k^2}{2m_0} - \frac{2P^2 k^2}{3E_g} = -\frac{\hbar^2 k^2}{2m_{lh}^*}$$
(2.15)

Split-off band:
$$E_{so}(k) = -\Delta + \frac{\hbar^2 k^2}{2m_0} - \frac{2P^2 k^2}{3(E_g + \Delta)} = -\Delta - \frac{\hbar^2 k^2}{2m_{so}^*},$$
(2.16)

where P is Kane's parameter, E_g is the band gap, and Δ is the split-off energy. Each dispersion curve can be represented with an energy offset: either the band gap or the split off energy and a parabolic function with curvature defined by an effective mass. The effective mass for an electron in the conduction band of CdTe is $m_c^* = 0.1\ m_0$, where m_0 is the mass of an electron. The heavy hole and light hole effective masses are $m_{hh}^* = 0.45\ m_0$ and $m_{lh}^* = 0.1\ m_0$ respectively (40).

With these energy corrections, we then obtain the new eigen functions for the different bands. We present them below in terms of the spherical-harmonic and spin-state vector and the total angular momentum and its z-projection $|J,\ J_z\rangle$:

Conduction band:
$$\left| iS \downarrow \right\rangle = \left| \frac{1}{2}, \frac{-1}{2} \right\rangle$$
(2.17)

$$\left| iS \uparrow \right\rangle = \left| \frac{1}{2}, \frac{1}{2} \right\rangle$$
(2.18)

Heavy-hole band:
$$\left| -\frac{X + iY}{\sqrt{2}} \uparrow \right\rangle = \left| \frac{3}{2}, \frac{3}{2} \right\rangle$$
(2.19)

$$\left| \frac{X - iY}{\sqrt{2}} \downarrow \right\rangle = \left| \frac{3}{2}, \frac{-3}{2} \right\rangle$$
(2.20)

18

Light-hole band:
$$\frac{1}{\sqrt{6}}\left|\frac{X-iY}{\sqrt{2}}\uparrow\right\rangle+\sqrt{\frac{2}{3}}\left|Z\downarrow\right\rangle=\left|\frac{3}{2},\frac{-1}{2}\right\rangle \tag{2.21}$$

$$\frac{-1}{\sqrt{6}}\left|\frac{X+iY}{\sqrt{2}}\downarrow\right\rangle+\sqrt{\frac{2}{3}}\left|Z\uparrow\right\rangle=\left|\frac{3}{2},\frac{1}{2}\right\rangle \tag{2.22}$$

Split-off band
$$\frac{1}{\sqrt{3}}\left|\frac{X-iY}{\sqrt{2}}\uparrow\right\rangle+\sqrt{\frac{1}{3}}\left|Z\downarrow\right\rangle=\left|\frac{1}{2},\frac{-1}{2}\right\rangle \tag{2.23}$$

$$\frac{1}{\sqrt{3}}\left|\frac{X+iY}{\sqrt{2}}\downarrow\right\rangle+\sqrt{\frac{1}{3}}\left|Z\uparrow\right\rangle=\left|\frac{1}{2},\frac{1}{2}\right\rangle. \tag{2.24}$$

From the Kane's model we are able to obtain the eigen functions for the conduction band and valence bands, and the energy shift for the split-off band, shown as $-\Delta$ in Figure 2.3. The solution based on these four bands does not give the correct curvature for the heavy-hole valence band. However, incorporation of higher bands corrects this. A diagram for the dispersion curves is shown in Figure 2.3.
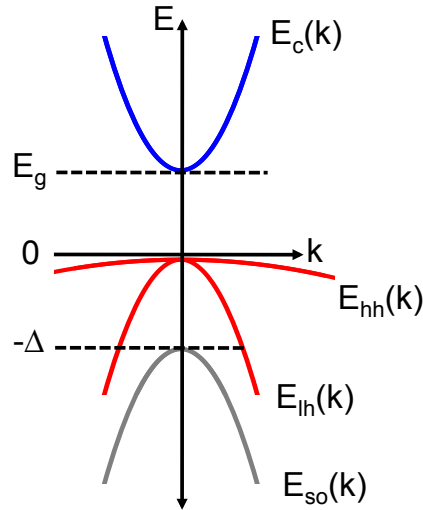
Figure 2.3. Energy dispersion curves near k=0 for the conduction, heavy-hole, light-hole, and split-off band.

2.3. Effects of Confinement

The energy level structures of semiconductors can be engineered or tailored with

heterostructures. This can be illustrated with the classical "particle in a box" problem. The energy eigenstates for the solution to the Schrödinger equation for a particle in a 1D box with infinite barriers is

$$E_n = n^2 \frac{\hbar^2 \pi^2}{2mL^2} ,$$ (2.25)

where n is an integer, m is the mass of the particle, and L is the width of the well. The first few wave functions are plotted at their corresponding energy levels in Figure 2.4.
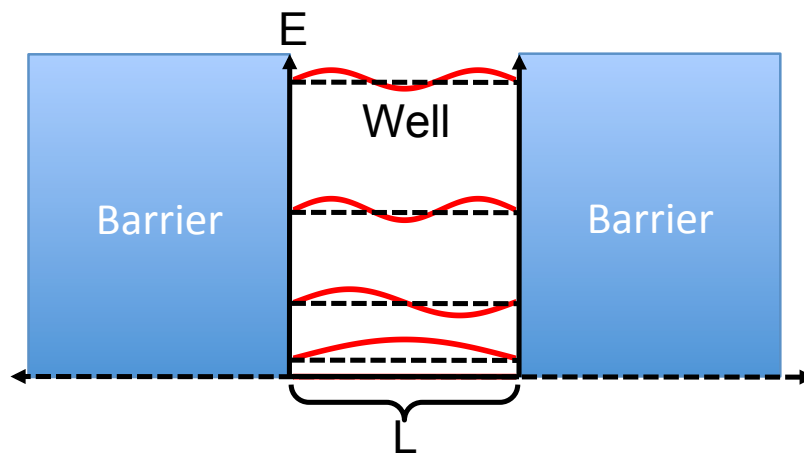
Figure 2.4. The energy levels and wave functions for a particle in a one-dimensional infinite well for n=1, 2, 3 and 4. The black dashed lines are at the eigen energies, and the red curves are the wave functions at the respective energy level.

Confinement of electrons and holes in a semiconductor is possible by layering materials with different energy band gaps, and it can be one dimensional, two-dimensional or three-dimensional. The corresponding structures are called quantum wells (QW), wires, and dots. Of interest to this dissertation is confinement due to a QW; therefore, the discussion of semiconductor heterostructures here will be limited to one-dimensional confinement.

A semiconductor QW features finite barrier height. For a given barrier and well

20

material the lowest energy state for an electron or hole in a semiconductor QW is determined by its mass and the well width. The energy of a particle within a well is inversely proportional to the mass of the particle. Therefore, the more massive a particle is the lower its energy within a well. The different effective mass for heavy and light holes results in a lifting of the energy degeneracy at k=0, shown in Figure 2.2 and 2.3.

2.4. Optical Excitations

To understand how electrons are promoted from the valence band to the conduction band, it is useful to consider the wave functions for the various bands of interest, which are the conduction, heavy-hole, and light-hole bands. The split-off band is energetically far removed due to spin-orbit interactions; therefore, it will be ignored for the remainder of this dissertation. The dipole matrix elements governing the interband optical excitations are given by

$$\mu_{cv} = e \langle c | \vec{r} | v \rangle, \tag{2.26}$$

where v represents the various valence band states, c represents the conduction band states, e is the electron, and $\vec{r}$ is the position operator.

The allowed optical transitions for circularly polarized light propagating in the growth direction of the QW are presented graphically in Figure 2.5. The states are labeled according to total angular momentum, J, and z-component of the angular momentum (or spin) as $|J, J_z\rangle$. The heavy-hole states are $\left|\frac{3}{2}, \pm\frac{3}{2}\right\rangle$, the light-hole states $\left|\frac{3}{2}, \pm\frac{1}{2}\right\rangle$, and the conduction band states are $\left|\frac{1}{2}, \pm\frac{1}{2}\right\rangle$. Notice the light- and heavy-hole states are diagrammed as energetically split due to confinement.

$\lvert 1/2,\ 1/2\rangle$ ____	____ $\lvert 1/2,\ -1/2\rangle$	Conduction band
$\sigma-$	$\sigma+$	
$\lvert 3/2,\ 3/2\rangle$ ____	____ $\lvert 3/2,\ -3/2\rangle$	Heavy-hole band
$\lvert 3/2,\ 1/2\rangle$ ____	____ $\lvert 3/2,\ -1/2\rangle$	Light-hole band
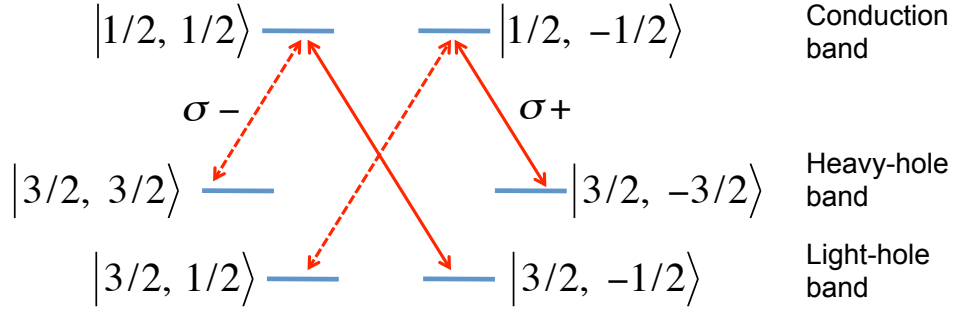
Figure 2.5. Polarization selection rules for coupling electron states in the valence band to the conduction band for a CdTe QW. The states are labeled by their total and z-component (spin) of angular momentum $|J, J_z>$. Hole states have total angular momentum J= 3/2, and conduction band states have total angular momentum J=½. Dipole coupling with circular polarized light is indicated by red arrows, solid for σ+ and dotted for σ -.

2.5. Magnetic Field Effects on Spins in QWs

Experiments presented in this dissertation are focused on transitions between the heavy-hole band and the conduction band in the presence of a magnetic field in the Voigt geometry (Figure 2.6c). The Voigt configuration defines the optic axis as normal to the growth direction of the sample and a magnetic field applied transverse to optic axis (i.e. in the plane of the QW). For the conduction band, electron spins are aligned parallel or anti-parallel to the magnetic field, as a result of the Zeeman effect. The interaction Hamiltonian between an electron and an external magnetic field is given by

$$V_M = -\vec{\mu} \cdot \vec{B} ,\tag{2.27}$$

where $\vec{B}$ is the magnetic field, $\vec{\mu} = -\mu_B g \vec{J} / \hbar$ is the magnetic moment (μ_B being the Bohr magneton), $\vec{J}$ being the total angular momentum, and g is the effective electron g-factor. Here the energy eigenstates of the electrons are defined by the magnetic field $\vec{B}$, which is perpendicular to the optic axis.

In descriptions of band structure, Section 2.3, and optical interactions in

semiconductors, Section 2.4, we have followed conventional labeling practices for optical

interactions with semiconductors, which defines the optic axis as the z-axis. We are now

defining the optic axis the x-axis. This is because we are primarily interested in the

eigenstates of electron spins, which are defined by the magnetic field axis. Experiments in

this dissertation were performed in the Voigt geometry, with the magnetic field axis

perpendicular to the optic axis. Therefore, for the rest of this dissertation we define the

magnetic field axis as the z-axis and the optical axis as the x-axis, as shown in Figure

2.6(c).
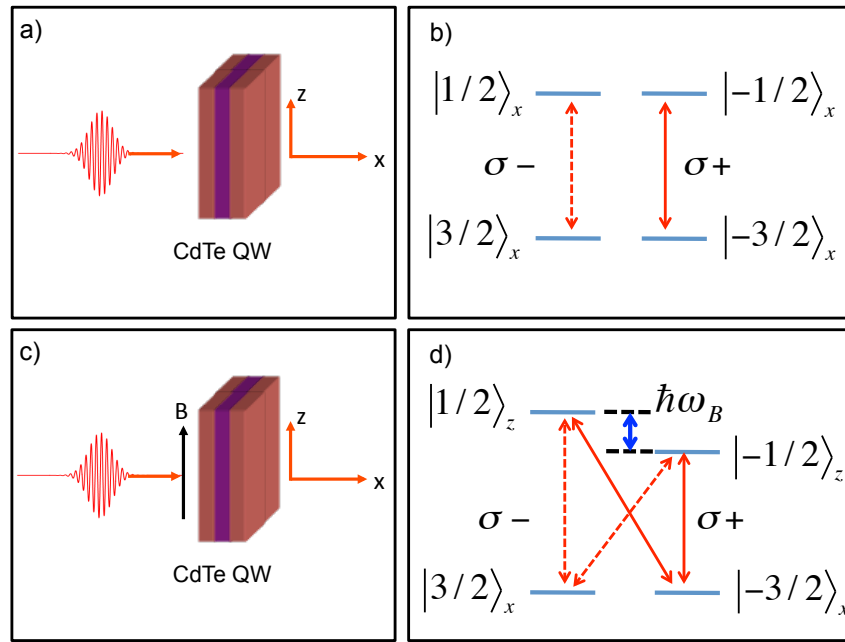
Figure 2.6. Sample geometry (a) and the polarization selection rules for coupling heavy-hole bands ($J_x=+/- 3/2$) to conduction bands ($s_x=+/- 1/2$) in the absence of a magnetic field (b). The sample geometry with an in-plane magnetic field (Voigt geometry) is diagrammed (c) with the modified polarization selection rules (d) due to electron spin quantization along the magnetic field axis ($s_x=+/- 1/2$).

Conduction band electrons are immune to the effects of spin-orbit coupling.

Therefore, they can readily align with a magnetic field. However, valance band electrons

are strongly influenced by spin-orbit coupling. In semiconductors with an in-plane

compressive strain or heterostructures resulting in quantum confinement, like a QW, the growth direction becomes a preferred quantization axis for heavy-hole spins. This results in the heavy-hole spins being constrained to project normal to the quantum well plane (*41, 42*).

The confinement potential orients the hole spins in the growth direction of the QW and scales with energy splitting between the heavy-hole and light-hole bands (*43*). In essence there are two competing factors in defining the eigenstates for the holes: one is the confinement potential (x-axis), and the other is the transverse magnetic field (z-axis). In our experiments, the confinement energy is greater than 10 meV while the Zeeman energy is ~0.5meV. As a result, the hole states defined by the growth direction of the sample remain a good quantization axis (*41-43*).

The external magnetic field in the plane of the QW modifies the optical selection rules presented earlier. The heavy-hole spin states in the growth direction, J_x, remain good quantum numbers, while s_x electron spin states are mixed by the in-plane magnetic field. As a result, s_z becomes a good quantum number for electron spins. The mixing of the electron spin states allows for radiative coupling of each hole state to both electron spin states, as diagrammed in Figure2.6d. The modification of the optical selection rules in the presence of a transverse magnetic field is essential in the optical control of electron spins and will be presented in Section 2.9.

2.6. Excitons

The optical processes of interest to this dissertation result from band edge optical excitations in semiconductors. Band edge optical excitations are characterized by excitons.

An exciton is a Hydrogen-like bound state of an electron in the conduction band and a hole in the valence band. The effective mass description of electrons and holes allows one to model the electron-hole interaction in the same way one models a Hydrogen atom. In semiconductors, electric field screening, due to a large dielectric constant, reduces the Coulomb interaction between electrons and holes. Along with the screened Coulomb interaction, the small effective masses of electrons and holes result in a binding energy ~10meV, which is 3 orders of magnitude weaker than the hydrogen atom. The resultant excitons are called Wannier-Mott excitons, which have a Bohr radius of ~10nm.

In the effective mass approximation, we only need to consider the solution to the Schrödinger equation for the Hydrogen atom,

$$\left(\frac{\hbar^2}{2m_r} \nabla^2 + V(\vec{r}) \right) \psi(\vec{r}) = E(\vec{k}) \psi(\vec{r}), \qquad (2.28)$$

to model the Coulomb interaction between an electron and a hole, where m_r is the reduced effective mass of the electron hole pair, and $V(\vec{r})$ is the coulomb potential. The binding energy of an exciton in a bulk system, modeled in three-dimensions (3D), is given as

$$E_n^{3D} = \frac{-R_y}{n^2}, \qquad (2.29)$$

where R_y is the Rydberg energy, and n is an integer. In CdTe the Rydberg energy is 12meV (*44*). The confinement along the growth direction of a QW reduces the degrees of freedom for electrons and holes to two-dimensions. The binding energy for a two–dimensional (2D) exciton is

$$E_n^{2D} = \frac{-R_y}{\left(n - \frac{1}{2} \right)^2} . \qquad (2.30)$$

The strongest exciton absorption is due to the creation of 1s excitons (n=1), and the

25

binding energy for 1s excitons is four times greater in 2D than in 3D. The exciton binding

energy results in a well-defined spectral resonance that is removed from the band edge. The

absorption spectra for the CdTe QW sample used in the experiments presented in this

dissertation is shown in Figure 2.7. The heavy-hole exciton resonance is indicated at 771

nm and to the red of the exciton resonance is another absorption peak labeled trion.
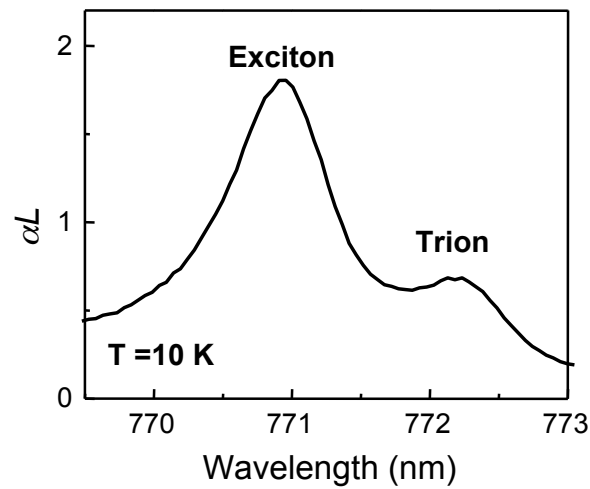
Figure 2.7. Absorption spectra showing exciton and trion peaks.

2.7. Trions

An exciton can be bound to an excess electron or hole, forming a charged exciton,

or trion, as diagrammed in Figure 2.8b. A negatively charged trion is composed of a hole

and two electrons of opposite spin. Just as one can model an exciton using the Schrödinger

equation for the Hydrogen atom, it is possible to estimate the binding energy of a charged

exciton by modeling it in the same way one models the Helium atom. That is, using the

variational method. The variational method uses a trial wavefunction that has one or more

adjustable parameters to calculate the expectation value of the energy. The parameters are

adjusted to minimize the expectation value of the Hamiltonian. To estimate the binding

energy of a negatively charged exciton, a first approach is to use the exciton wavefunction

as a trial function with the charge of the hole an adjustable parameter. The treatment of the

hole charge as a variable is a reasonable one, as it accounts for the effect hole screening by

the second electron. There are more sophisticated ways to obtain more accurate estimates

for the binding energy, which typically involve more complex trial wavefunctions (*45-47*).
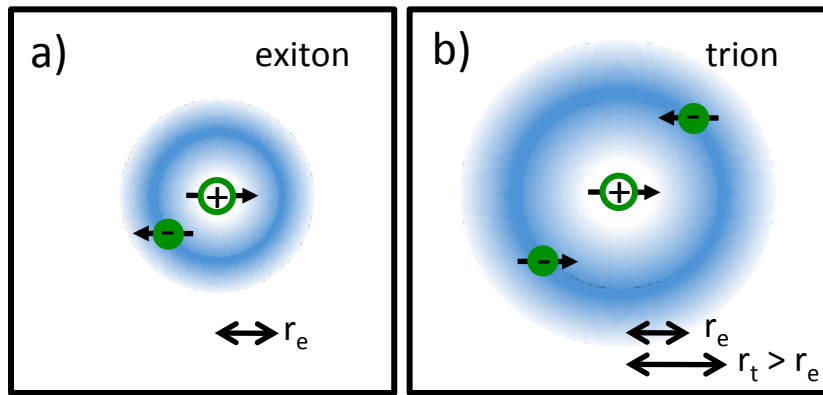
Figure 2.8. Diagram of an exciton (a), where an electron hole pair forms a hydrogenic
quasi-particle. The trion diagrammed in (b) is made up of two electrons and a single heavy
hole. Note the radius of the trion is much larger than that of the exciton, a result of the
relatively weak binding energy.

The theoretical analysis of trion binding energy demonstrates that the binding

energy of trions increases with confinement, from about 10% of the exciton binding energy

in 3D to about ~50% in the 2D limit (*46, 47*). Also, there is no theoretical or experimental

evidence for an excited state for trions (*47*). A simple relation that can be used to estimate

the binding energy of trions in quantum wells is given as

$$E_B^T \approx \frac{R_y}{3\sqrt{L/a_B}} ,$$
(2.31)

where a_B is the exciton Bohr radius, L is the well width, and R_y is the exciton Rydberg

energy. For our system, the calculated binding energy from the above equation is ~3 meV, and it is experimentally measured to be ~2.5 meV. Since the binding of an exciton to a charge (forming a trion) is energetically favorable, it is possible to observe a well defined spectral resonance associated with trion formation below the exciton resonance, as seen in Figure 2.7, with the trion 2.5 meV below the exciton.

To form a negatively charged trion there must be excess electrons present to which an exciton may be bound. A semiconductor quantum well with donor atoms in the barrier can supply the well region with excess electrons by shifting the Fermi energy, thus allowing for trion creation.

2.8. CdTe Quantum Well Structure

Our experiments used a high quality n-doped CdTe QW grown by molecular beam epitaxy on a $Cd_{0.88}Zn_{0.12}Te$ substrate that is transparent near the band edge. The sample consists of 10 periods of 10 nm CdTe wells and 45 nm $Cd_{0.84}Zn_{0.16}Te$ barriers (*48*). One QW period is diagrammed in Figure 2.9. By modulation doping with Indium, with a density estimated to be $3x10^{10}=cm^2$, excess electrons tunnel into the QW and form a two-dimensional electron gas (2DEG). In this sample, trion absorption is shown in Figure 2.7 and is characterized by a linewidth of 0.8 nm (1.6 meV) and a trion binding energy of 2.5 meV (1.25 nm). By tuning a laser to the trion resonance, it is possible to directly couple the spin states of the electrons in the 2DEG to trion states.
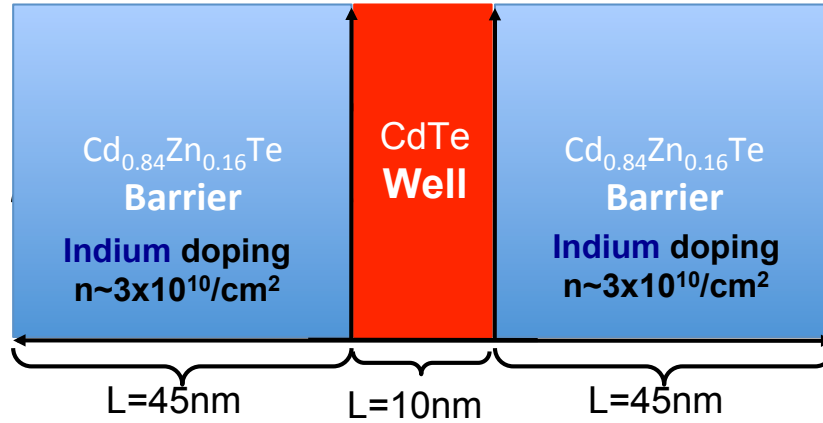
Figure 2.9. A single period of the 10 period QW sample used in our research. The sample consists of 10 nm CdTe wells and 45 nm $Cd_{0.84}Zn_{0.16}$Te barriers. Indium is doped in the barriers at $3x10^{10}$=cm^2.

2.9. Polarization Selection Rules for Trions

In a semiconductor with an excess electron population, these electrons can be radiatively coupled to a (negatively-charged) trion state. The dipole optical transitions involved are specific to the spin states of the electrons. This is graphically shown in Figure 2.10, with electron spins as the lower states and trion states as the excited states. We know from the polarization selection rules for exciting carriers from the heavy-hole band that $\sigma+$ circularly polarized laser light will create an electron with spin $|-1/2\rangle$ and a hole with spin $|3/2\rangle$. These two particles, in the presence of excess electrons with spin $|+1/2\rangle$, can form a trion. Thus, $\sigma+$ couples electrons of spin $|+1/2\rangle$ to the heavy-hole trion state with hole spin $|3/2\rangle$, labeled as $|T+\rangle$, in Figure 2.10.
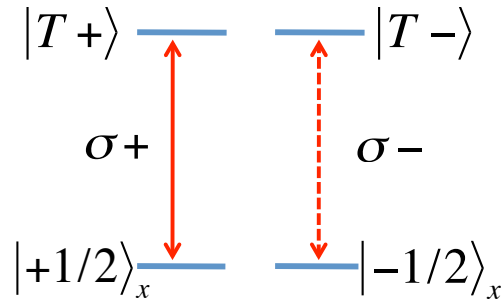
Figure 2.10. The polarization selection rules for coupling electron spins to a trion.

With the application of a magnetic field in the z-direction (Voigt geometry, Figure 2.6c), the energy eigenstates for spins are no longer along x but along the z-axis. With regard to the trion states, a trion state is defined by the eigenstates of its heavy hole because the two electrons are in a singlet state. Therefore, the trion states remain quantized in the growth direction of the sample because heavy holes in a QW are confined to orient normal to the well plane even with a modest transverse magnetic field. The polarization selection rules are thus modified to include the new eigenstates for the electrons but maintain the eigenstates of the trions. Figure 2.11 illustrates the modified polarization selection rules.
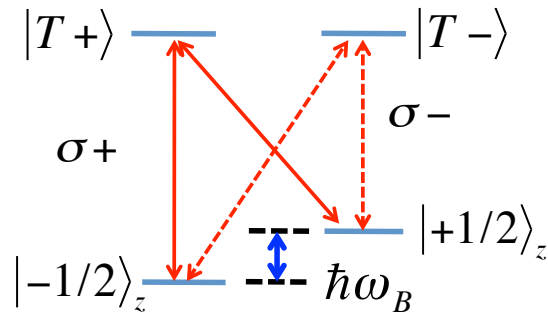
Figure 2.11. The modified polarization selection rules for coupling electrons spins to trion states in the presence of a magnetic field oriented along the z-axis (Voigt geometry).

The radiative coupling of the two electron spin states to an excited state thus results in two Λ-type three-level systems in which the electron spin states form the two ground

states and the trion states define the excited state. By selecting σ+ polarized laser radiation it is possible to address a single Λ-type system for the study of electron spin coherence in semiconductors through the exploitation of a Raman transition (*15-17*).

2.10. Chapter Summary

In this chapter we describe the fundamentals of optical interactions in a direct band gap semiconductor. We introduced neutral excitons and charged excitons (trions), and discussed the radiative processes responsible for coupling electrons in a 2DEG to the trion excited state. We described how to establish, with the aid of a magnetic field, a three-level Λ-type system for the electron spin states.

CHAPTER III

OPTICAL SPIN CONTROL: THEORY

In this chapter we develop the theoretical description of optical control of electron spins. By exploiting a Raman transition we are able to decouple the two ground states of a Λ-type three-level system from the excited state, resulting in an effective 2-level system. We present the Λ-type system that describes the radiative coupling of electron spins to a common trion state and reduce it to an effective two-level system.

This chapter begins with a review of the dynamics of two-level systems as described by the Rabi problem. Then we introduce the Λ-type three-level system, which is described by dipole optical transitions that couple the two ground states to a common excited state. The three-level Λ-type system is then reduced to an effective two-level system in the limit of the adiabatic approximation. We then investigate the resultant approximate description of the evolution of the spins with two sets of polarization selection rules.

We show that particular limits are observed governing the effectiveness of control in systems where the two dipole transitions have the same polarization selection rule, which is the case for our electron-trion Λ-system. These limitations are not present for Raman transitions with orthogonal polarization selection. We end the chapter by introducing the optical Bloch equations (OBE) to account for decays and decoherences.

3.1. Two-Level System

Coherent control of quantum systems refers to the ability to reversibly manipulate an initial quantum state to a final state, $|\psi_{initial}\rangle \Rightarrow |\psi_{final}\rangle$. To control the state of the system we design an interaction Hamiltonian $|\psi_{final}\rangle = H|\psi_{initial}\rangle$. In a two-level system, this can be accomplished using a resonant or off-resonant driving field. Figure 3.1 depicts a two-level atom coupled by a field of frequency ω.
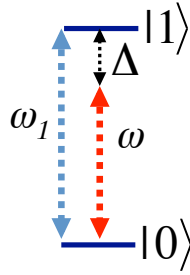
Figure 3.1 A schematic of a two-level atom with energy difference $\hbar\omega_1$ and a coupling field ω, detuned by Δ.

The Hamiltonian for the two-level system driven by an oscillating field in the $\{|1\rangle, |0\rangle\}$ basis is written as

$$H = \begin{pmatrix} \hbar\omega_1 & -\mu E\cos(\omega t) \\ -\mu E^*\cos(\omega t) & 0 \end{pmatrix}. \tag{3.1}$$

After making the rotating wave approximation (RWA) and only keeping the slowly oscillating terms, the Hamiltonian is

$$H = \begin{pmatrix} \hbar\omega_1 & -\dfrac{\mu E\exp[-i\omega t]}{2} \\ -\dfrac{\mu E\exp[i\omega t]}{2} & 0 \end{pmatrix}. \tag{3.2}$$

We can further simplify the Hamiltonian by going into the rotating frame of the field,

where the rotating frame state vector is written as

$$|\tilde{\psi}(t)\rangle = C_1 \exp(-i\omega t)|1\rangle + C_0 |0\rangle$$
$$= \tilde{C}_1 |1\rangle + C_0 |0\rangle \qquad .$$

(3.3)

and the rotating frame Hamiltonian after the RWA is

$$H = \hbar \begin{pmatrix} \Delta & \Omega/2 \\ \Omega^*/2 & 0 \end{pmatrix},$$

(3.4)

where $\Delta \equiv \omega - \omega_1$ is the detuning of the coupling field from the excited state energy, and

$\Omega \equiv -\mu E / \hbar$ is the Rabi frequency. This is the frequency of population oscillation

between the two states as a result of the driving field E. These simplifications eliminate the

explicit time dependence of the Schrödinger equation, leaving us with

$$i\hbar \frac{d}{dt}\begin{pmatrix} \tilde{C}1 \\ C0 \end{pmatrix} = \hbar \begin{pmatrix} \Delta & \dfrac{\Omega}{2} \\ \dfrac{\Omega^*}{2} & 0 \end{pmatrix}\begin{pmatrix} \tilde{C}1 \\ C0 \end{pmatrix}.$$

(3.5)

Now we can solve the coupled equations for the probability amplitudes in the

rotating frame and observe the dynamics of the two-level system. We will begin with the

population at time t=0 in the lower state $|\psi(0)\rangle = |0\rangle$. We first obtain the solution in the

case of exact resonance, followed by the more general, nearly resonant case.

3.1.1. Rabi Oscillations with Resonant Coupling Field

In the case of zero detuning and the population initially in the lower state the

probability amplitudes are

$$C_0(t) = \cos\left(\frac{1}{2}\Omega t\right)$$

(3.6)

and $\quad \tilde{C}_1(t) = -i \sin\left(\frac{1}{2}\Omega t\right).$ (3.7)

From the probability amplitudes we know the excited and ground state populations are

$$P_0(t) = |C_0(t)|^2 = \frac{1}{2}\left(1 - \cos(\Omega t)\right)$$ (3.8)

and $\quad P_1(t) = |\tilde{C}_1(t)|^2 = |C_1(t)|^2 = \frac{1}{2}\left(1 + \cos(\Omega t)\right).$ (3.9)

The solution to the Schrödinger equation shows the complete population transfer from $|0\rangle$ to $|1\rangle$ when $\Omega t = \pi$. This is a completely coherent process of population transfer between the two states. The probability of finding the atom in the excited state as a function of time, following the solution above (3.9), is shown in Figure 3.2.
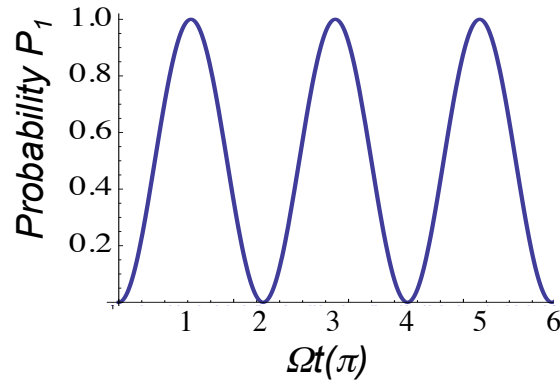
Figure 3.2. Rabi oscillations for a two-level system driven on resonance, ignoring decay. The vertical axis is the probability of finding the atom in state $|1\rangle$. The horizontal axis is in units of the Rabi period.

3.1.2. Nearly Resonant Dynamics

Now we extend the solution to the wave equation for the two-level system driven by an arbitrarly detuned monochromatic field. Again, the population is initially in the lower state. The probability amplitudes are

$$C_0(t) = e^{i\Delta t/2}\left[C_0(0)\cos\left(\frac{1}{2}\tilde{\Omega}t\right) - \frac{i}{\tilde{\Omega}}[\Delta C_0(0) + \Omega \tilde{C}_1(0)]\sin\left(\frac{1}{2}\tilde{\Omega}t\right)\right] \tag{3.10}$$

and $\quad \tilde{C}_1(t) = e^{i\Delta t/2}\left[\tilde{C}_1(0)\cos\left(\frac{1}{2}\tilde{\Omega}t\right) + \frac{i}{\tilde{\Omega}}[\Delta \tilde{C}_1(0) - \Omega C_0(0)]\sin\left(\frac{1}{2}\tilde{\Omega}t\right)\right],$ $\quad$ (3.11)

where $\tilde{\Omega} \equiv \sqrt{\Omega^2 + \Delta^2}$ is the generalized Rabi frequency.

Figure 3.3 shows the probability of finding the system in the excited state as a function of Ωt for several detunings. Figure 3.3 shows increased detuning (in units of Rabi frequency) results in a decrease in the maximum probability of the system being in the excited state result.
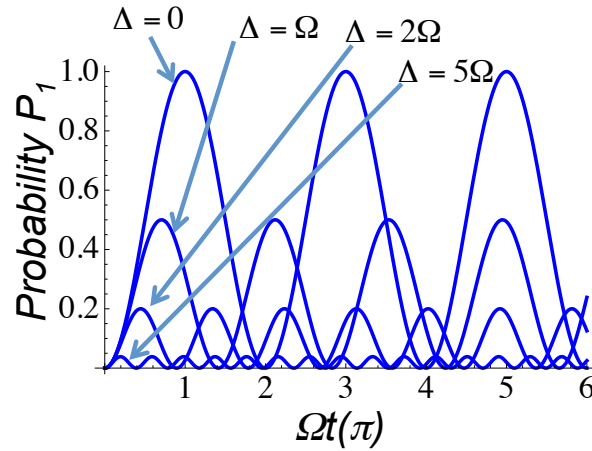
Figure 3.3. Probability of a population being in state $|1\rangle$ is plotted as a function of time, in units of Rabi period, for a series of detunings.

3.1.3. Two-Level Control and Summary

The Rabi problem shows us that the probability of finding the system in the excited state, for a resonant field, occurs when $\Omega t=(2n+1)\pi$. For pulsed fields, the probability of the system being in the excited state after a driving pulse is determined by the time integral

of the Rabi frequency, or "pulse area." For example, a π pulse is $\pi = \int \Omega(t)\, dt$ and results

in population transfer from $|0\rangle$ to $|1\rangle$.

The Rabi problem demonstrates that population can be coherently transferred

between states. However, complete control of the two-level system requires the ability to

generate arbitrary superpositions with arbitrary phase. Control over the area and phase of

the driving field results in complete control of the two-level system. To show this we allow

for the phase of the driving field ϕ to be incorporated in the probability amplitudes in the

rotating frame. The rotating frame state vector is

$$|\tilde{\psi}(t)\rangle = C_1 \exp(-i\delta t - i\phi)\,|1\rangle + C_0\,|0\rangle$$
$$= \tilde{C}_1\,|1\rangle + C_0\,|0\rangle$$

(3.12)

To show the ability to generate arbitrary rotations we simply take the solution for

the on-resonance case with the state initialized to $|0\rangle$ at t=0. The state of the two-level

system can thus be written as

$$\left|\psi_{final}(\theta,\phi)\right\rangle = -i\sin\left(\frac{1}{2}\theta\right)\exp[-i\omega t - i\phi]|1\rangle + \cos\left(\frac{1}{2}\theta\right)|0\rangle,$$

(3.13)

in the laboratory frame. With control over ϕ and $\theta \equiv \int \Omega(t)dt$, full quantum control of a

two-level system is possible.

3.2. Three-Level System

We now describe the dynamics of a Λ-type three-level system and the limits

required to reduce the Λ-type system to a more compact description. Figure 3.4 diagrams

the Λ–type system and the effective two-level system obtained by reducing the Λ-system to

an effective two-level system. The Hamiltonian that describes optical interactions in this

three-level system can be written in the $\{|T\rangle, |+\rangle, |-\rangle\}$ basis as

$$H = \begin{pmatrix} \hbar\omega_e & V_+ & V_- \\ V_+^* & \hbar\omega_B/2 & 0 \\ V_-^* & 0 & -\hbar\omega_B/2 \end{pmatrix},$$ (3.14)

where V_+ and V_- are the matrix elements for the relevant dipole optical interactions. The two ground states $|+\rangle$ and $|-\rangle$ are not directly coupled. They are only coupled through the excited state $|T\rangle$. To maintain generality, no assumptions are made at this point with respect to the polarization selection rules of the dipole transitions.
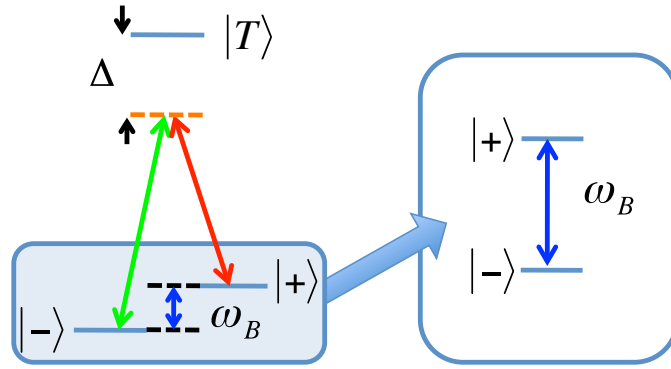
Figure 3.4. Schematic of a three-level system where the two lower spin states couple to the common excited state via two dipole optical transitions. Through the adiabatic elimination of the trion state, the dynamics of the system can be reduced to an effective two-level system for the spins.

In the rotating frame, the state vector of the three-level system can be written as

$$\left|\psi(t)\right\rangle = C_e \exp(-i\bar{\omega}t)|e\rangle + C_+|+\rangle + C_-|-\rangle,$$ (3.15)

where $\bar{\omega} \equiv (\omega_1 + \omega_2)/2$ is the average frequency of the two external optical fields. Within the rotating wave approximation, the Schrödinger equation for the state vector is given by

$$i\hbar\frac{d}{dt}\begin{pmatrix} C_e \\ C_+ \\ C_- \end{pmatrix} = \hbar\begin{pmatrix} \Delta & \Omega_+ & \Omega_- \\ \Omega_+^* & \omega_B/2 & 0 \\ \Omega_-^* & 0 & -\omega_B/2 \end{pmatrix}\begin{pmatrix} C_e \\ C_+ \\ C_- \end{pmatrix},$$ (3.16)

38

where $\Delta \equiv \omega_e - \bar{\omega}$ is the average detuning for the dipole transition, and we define

$V_+ \equiv \hbar\Omega_+ \exp(-i\bar{\omega}t)$ and $V_- \equiv \hbar\Omega_- \exp(-i\bar{\omega}t)$.

For detuning much larger than the linewidth of the excited state, the dynamics of the excited state adiabatically follow the external optical fields as well as the two lower level spin states (*16*). The adiabatic approximation assumes that the dynamics associated with coupling to the excited state quickly reach steady state when compared to the dynamics of the system. Therefore, in this adiabatic limit, we have

$$i\frac{d}{dt}C_e = \Delta C_e + \Omega_+ C_+ + \Omega_- C_- \approx 0, \tag{3.17}$$

where the change in the probability amplitude of the excited state is approximated as zero.

The three-level system can then be reduced effectively to a two-level system,

$$i\hbar\frac{d}{dt}\begin{pmatrix} C_+ \\ C_- \end{pmatrix} = H_{eff}\begin{pmatrix} C_+ \\ C_- \end{pmatrix}, \tag{3.18}$$

with an effective Hamiltonian given by

$$H_{eff} = \hbar\begin{pmatrix} \dfrac{\omega_B}{2} - \dfrac{|\Omega_+|^2}{\Delta} & -\dfrac{\Omega_+^*\Omega_-}{\Delta} \\ -\dfrac{\Omega_+\Omega_-^*}{\Delta} & -\dfrac{\omega_B}{2} - \dfrac{|\Omega_-|^2}{\Delta} \end{pmatrix}, \tag{3.19}$$

where $|\Omega_\pm|^2/\Delta$ is the optical Stark shift induced by the external fields on the eigenstates of the system. We will now apply polarization selection rules to the Λ-type system and investigate the dynamics of the effective two-level system when driven on Raman resonance.

3.2.1. *Three-Level System with Orthogonal Polarization Selection Rules*

For a three-level system where the two dipole transitions have orthogonal

polarization selection rules, two optical fields, with amplitude E_1 and E_2 and frequency ω_1 and ω_2, couple to two separate dipole transitions, respectively. In this case, we have

$$\Omega_+ = -\frac{\mu_+ E_1}{2\hbar}\exp(-i\frac{\delta t}{2} - i\phi)$$

and $\quad \Omega_- = -\dfrac{\mu_- E_2}{2\hbar}\exp(i\dfrac{\delta t}{2})$, $\hfill$ (3.20)

where μ_+ and μ_- are the respective dipole matrix elements (assumed to be real), ϕ is the initial phase difference between the two optical fields, and $\delta \equiv \omega_1 - \omega_2$. The effective two-level Hamiltonian is given by

$$H_{eff} = \hbar \begin{pmatrix} \dfrac{\omega_B}{2} - \dfrac{|\Omega_+|^2}{\Delta} & -\dfrac{\Omega_R}{2}\exp[i(\delta t + \phi)] \\ -\dfrac{\Omega_R}{2}\exp[-i(\delta t + \phi)] & -\dfrac{\omega_B}{2} - \dfrac{|\Omega_-|^2}{\Delta} \end{pmatrix}, \hfill (3.21)$$

where $\Omega_R = \mu_+ \mu_- E_1 E_2 /(2\hbar^2\Delta)$ is the effective Rabi frequency for the spin-flip Raman transition.

To control this effective two-level system we consider two scenarios. First we consider a single pulse that couples to only one transition, for example $\Omega_+ = \Omega$ and $\Omega_- = 0$. Then we consider a pair of Raman resonant pulses with equal Rabi frequencies $\Omega_+ = \Omega_-$ and identical temporal profiles.

When $\Omega_+ = \Omega$ and $\Omega_- = 0$, the effective Hamiltonian reduces to

$$H_{eff} = \hbar \begin{pmatrix} \dfrac{\omega_B}{2} - \dfrac{|\Omega|^2}{\Delta} & 0 \\ 0 & -\dfrac{\omega_B}{2} \end{pmatrix}, \hfill (3.22)$$

where the effect of the optical pulse is an optical Stark shift of one of the energy eigenstates of the system. This results in control over the phase of coherent superposition states.

In the limit of equal optical Stark shifts, $\Omega_+ = \Omega_- = \Omega$, the resultant effective Hamiltonian is identical to the Rabi problem:

$$H_{eff} = \hbar \begin{pmatrix} \dfrac{\omega_B}{2} & -\dfrac{\Omega_R}{2}\exp[i(\delta t + \phi)] \\ -\dfrac{\Omega_R}{2}\exp[-i(\delta t + \phi)] & -\dfrac{\omega_B}{2} \end{pmatrix}.$$ (3.23)

The Raman resonance condition is met when the frequency difference of two laser fields equal to the ground state energy difference $\delta = \omega_B$, and coherent Rabi oscillations between ground states are possible. With control over the two-photon Rabi frequency Ω_R and the relative phase ϕ of the optical fields, complete control of the lower two states of a Λ-type system is possible. For a system with the initial state $|-\rangle$ the final state is determined by the phase and the time-integrated two-photon Rabi frequency. There is no explicit dependence on the duration of the pulse, only the area. This is not the case for Λ-type systems where both ground states couple to a common excited state with the same polarization selection rule.

3.2.2. Three-Level System with the Same Polarization Selection Rule

The electron-trion three-level system presented in this dissertation demonstrates the same polarization selection rule coupling two electron spin states to a common excited state, a trion. Therefore, a single optical field can couple to both dipole transitions. Figure 3.5a illustrates the three-level system with one coupling field of frequency ω_1. Figure 3.5b illustrates how the Raman resonance condition can be met with two fields with frequencies ω_1 and ω_2.
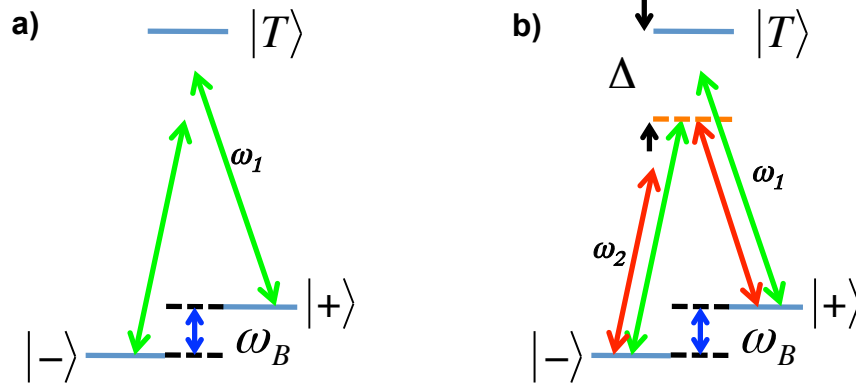
Figure 3.5. (a) Illustrates one field coupling both ground states to a common excited state. (b) Illustrates two fields with frequency difference equal to the ground state energy splitting, meeting the Raman resonance condition.

To meet the Raman resonance condition with two monochromatic fields we introduce a general Raman-resonant pair of fields. We will show that both a single pulse and a pulse pair can result in coherent rotations and can be derived from the same expression. In this case, we define the coupling to have

$$\Omega_+ = -\frac{\mu_+}{2\hbar}[E_1 \exp(-i\frac{\delta t}{2} - i\phi) + E_2 \exp(i\frac{\delta t}{2})] \qquad (3.24)$$

and

$$\Omega_- = -\frac{\mu_-}{2\hbar}[E_1 \exp(-i\frac{\delta t}{2} - i\phi) + E_2 \exp(i\frac{\delta t}{2})]. \qquad (3.25)$$

The effective two-level Hamiltonian is now given by

$$H_{eff} = \hbar \begin{pmatrix} \frac{\omega_B}{2} - \frac{|\Omega_+|^2}{\Delta} & -\Omega_R \cos(\delta t + \phi) \\ -\Omega_R \cos(\delta t + \phi) & -\frac{\omega_B}{2} - \frac{|\Omega_-|^2}{\Delta} \end{pmatrix} + \begin{pmatrix} 0 & -\frac{\mu_+ \mu_-}{4\hbar^2\Delta}(E_1^2 + E_2^2) \\ -\frac{\mu_+ \mu_-}{4\hbar^2\Delta}(E_1^2 + E_2^2) & 0 \end{pmatrix}. \qquad (3.26)$$

The first term in the effective Hamiltonian is identical to the results obtained for orthogonal polarization selection rules (equation 3.21). However, there is a second term in the

42

Hamiltonian, which is responsible for an optical Stark shift of state defined by the optical axis (*15*). We now investigate how this effective Hamiltonian determines the dynamics of the two-level system.

3.2.2.1. Single-Pulse Raman Resonance with Same Polarization Selection Rule

The effective Hamiltonian (equation 3.24) when $E_2=0$ and $\mu_+ \approx \mu_-$ describes the dynamics of the effective two-level system driven by a single optical pulse, which reduces to

$$H_{eff} = \hbar \begin{pmatrix} \dfrac{\omega_B}{2} & -\dfrac{\mu^2}{4\hbar^2\Delta}E_1^2 \\ -\dfrac{\mu^2}{4\hbar^2\Delta}E_1^2 & -\dfrac{\omega_B}{2} \end{pmatrix}. \tag{3.27}$$

In this Hamiltonian, an effective DC field couples the two states. The off-diagonal matrix element acts as an optical Stark shift of the superposition state $|x\rangle=\frac{1}{2}(|-\rangle+|-\rangle)$, which can also be thought of as an effective DC magnetic field coupling the spin states.

The effect of ω_B is to induce precession about the z-axis, the axis of the Bloch sphere defined by the energy eigenstates of the two-level system. The effect of $\dfrac{\mu^2}{4\hbar^2\Delta}E_1^2$ is to induce precession about the x-axis. To use the coupling field to effectively drive Rabi oscillations, the temporal duration of the coupling field must be much faster than the precession about the z-axis. Therefore E_1 should be a pulse with a duration much faster than the precession time about the z-axis.

To understand the limitations of how fast a pulse must be, relative to the precession time, we conducted a numerical simulation of the two-level system. The pulse used in the

simulation had a Gaussian temporal profile

$$E_1(t) \sim \exp[-(t-t_0)^2 / 2\sigma^2], \tag{3.28}$$

where t_0 set the arrival time of the pulse and σ is the standard deviation. The temporal full width half maximum of a Gaussian pulse is $T_{sp} \approx 2.35 \cdot \sigma$. Figure 3.6 plots the probability of transferring population from $|-\rangle$ to $|+\rangle$ for a pulse area of $\pi = \int \frac{\mu^2}{4\hbar^2 \Delta} |E_1(t)|^2 dt$ as a function of the pulse duration in units of the precession time $T_{\omega_B} = 1/\omega_B$. Figure 3.6 illustrates an important limitation to the single pulse rotation technique: the effectiveness of the single-pulse in transferring population degrades with an increase in its pulse duration. In other words, to meet the Raman resonance condition the pulse bandwidth must be far larger than the ground state splitting. Once the pulse duration is comparable to the precession time, the pulse has virtually zero effect on the system, as shown in Figure 3.6.
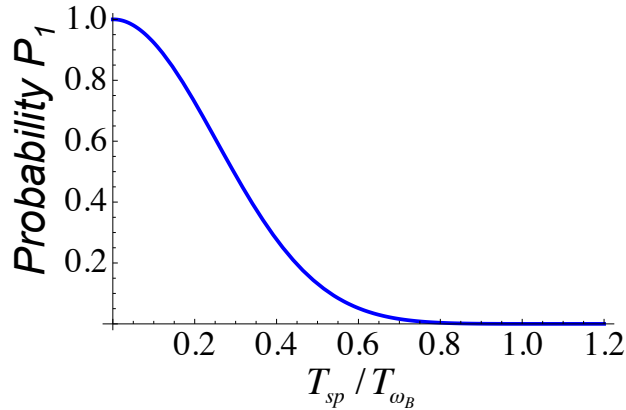
Figure 3.6. Numerical simulation of the probability of population transfer after a pulse of area π but with variable pulse duration. The probability of the excited state is plotted against the pulse duration normalized by the ground state energy splitting.

Given the high accuracy in the short pulse limit $T_{sp}/T_{\omega_B} \ll 1$, it is advantageous to consider how rotations about the optical axis may look. Now we present examples of

44

single pulse rotations for several rotation angles. Figure 3.7 presents the evolution of the

state vector on the Bloch sphere, along with its x-projection of the coherence for varied

rotation angle, set by pulse area. Rotations of $\pi/2$ about the x-axis when the state vector is

aligned with the y-axis result in the state vector being rotated into the z-direction, indicated

by the s_x projection being zero after the rotation. Again, the x-axis is the optic axis, and

this technique only rotates the state vector about the x-axis.

Figure 3.8 presents the effect of a π rotation about the optical axis at different

phases of coherence. A rotation about the x-axis has no effect on the state vector when the

vector points along the x-axis, as indicated by the state vector evolution diagrammed in the

top-most Bloch sphere and x-projection shown in Figure 3.8. A particular feature of this

rotation technique is the symmetry of the oscillations about the arrival time of the rotation

pulse when applied at various phases of coherence. This symmetry is also observed in

experiments presented in Chapter V.
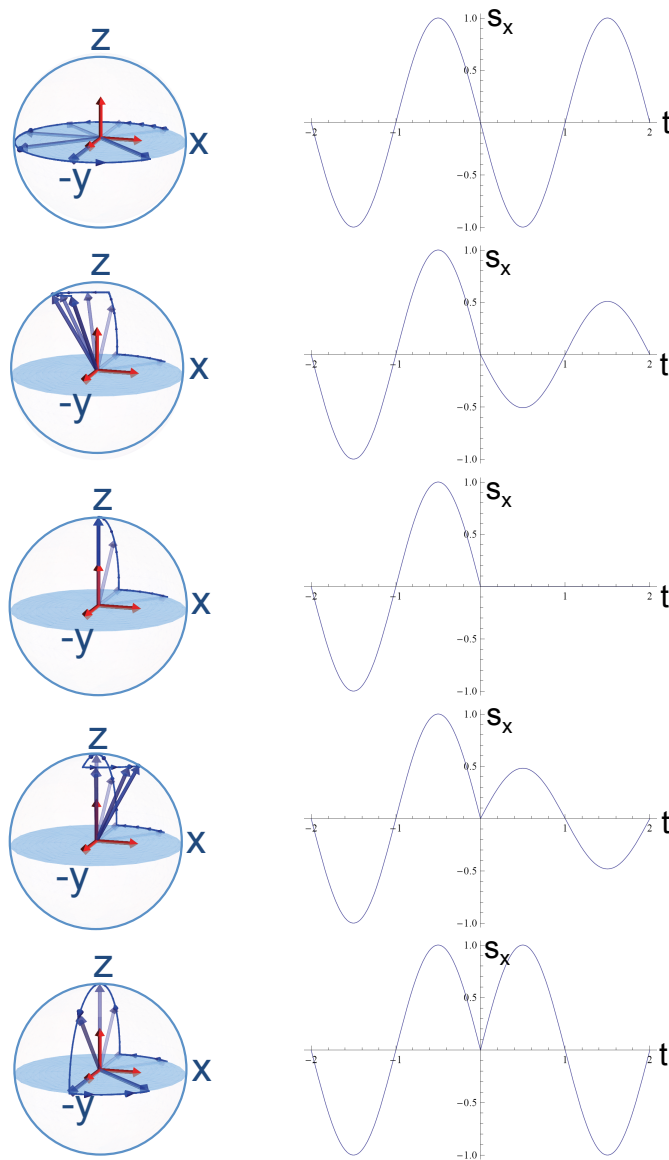
Figure 3.7. Rotations about the x-axis when the state vector is aligned with the y-axis. The paths drawn on the Bloch spheres indicate the path of the state vector before, during, and after the rotation pulse, while the curves represent the projection of the state vector along the x-axis. The rotation pulse areas are, from top to bottom, $0, \pi/4, \pi/2, 3\pi/4$ and π.
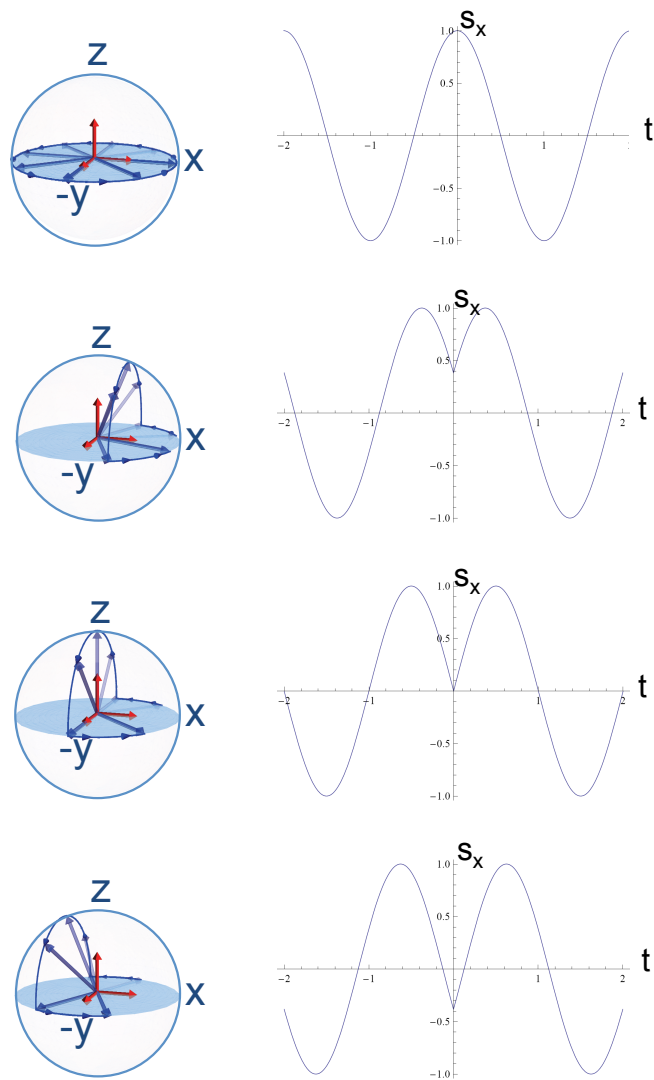
Figure 3.8. Rotations about the x-axis by π for various phases in precession. (Left) Bloch spheres are displayed with the temporal evolution of the state vector drawn. (Right) The x-projections of the π rotations with t=0 the rotation pulse arrival time. Notice the x-projections are symmetric about the arrival time of the rotation pulse. No change is observed for precession when the state vector is aligned with the x-axis at t=0.

3.2.2.2. Pulse-Pair Raman Resonance with Same Polarization Selection Rule

Now we consider a pair of pulses that are Raman resonant with the spin-flip transition. The effective Hamiltonian given in equation 3.26 reduces to

$$H_{eff} = \hbar \begin{pmatrix} \dfrac{\omega_B}{2} & -\Omega_R \cos(\delta t + \phi) - \dfrac{\mu^2 E^2}{2\hbar^2 \Delta} \\ -\Omega_R \cos(\delta t + \phi) - \dfrac{\mu^2 E^2}{2\hbar^2 \Delta} & -\dfrac{\omega_B}{2} \end{pmatrix}. \tag{3.29}$$

with $\mu_+ = \mu_- = \mu$ and $E_2 = E_1 = E$.

One term in the off-diagonal matrix elements represents an oscillating field coupling the two states, while the second term represents a DC component. As explained above, the DC term is responsible for single pulse rotations. The AC coupling term is identical to the off-diagonal matrix element present in the Rabi problem.

To better understand the relative contributions of the two components we performed numerical simulations to test how effective Raman resonant pulses are at transferring population from $|->$ to $|+>$. In our simulations we defined the temporal profile for the pair of pulses to have the same duration and amplitude. The fields were defined as

$$E(t) = E_1(t) = E_2(t) \sim \exp[-(t - t_0)^2 / 2\sigma^2]. \tag{3.30}$$

Figure 3.6 plots the probability of transferring population from $|-\rangle$ to $|+\rangle$ for a Raman resonant pulse-pair $|\delta| \approx \omega_B$ with an area of $\pi = \int \Omega_R(t)dt$ as a function of the pulse duration T_{pp} normalized by the precession time $T_{\omega_B} = 1/\omega_B$. Figure 3.9 illustrates an important feature of the Raman pulse pair rotation technique: when the duration of the pulse pair becomes longer than the precession time the effectiveness of the rotation improves. The poor effectiveness of population transfer with short pulses is due to contributions from the single pulse rotation terms present in the Hamiltonian. As shown in

Figure 3.9, when the duration of the pulses become long compared to the Larmor period the single pulse contributions become negligible.
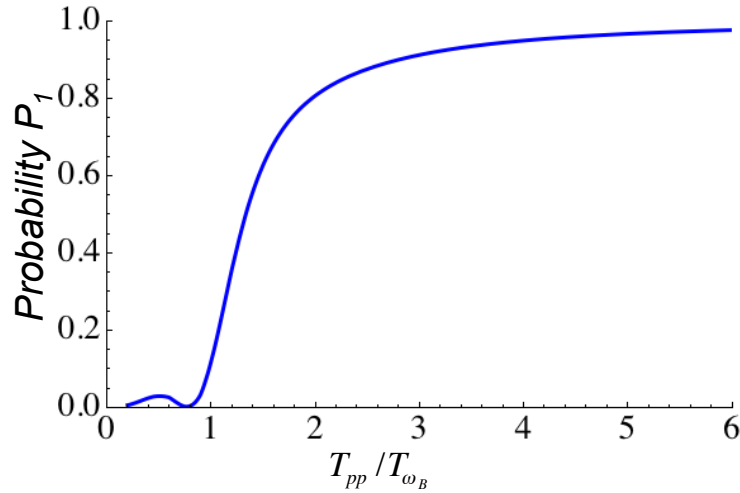
Figure 3.9. Probability of finding the system in the excited state as a function of pulse pair duration compared to the Larmor period.

The Raman pulse pair approach is quite effective in making accurate rotations when $T_{sp}/T_{\omega B}\gg1$. In other words, the effects of the individual laser fields become negligible when the ground state splitting ω_B is large compared to the spectral bandwidth of the individual laser pulses.

3.2.2.2.1. Complete Control with Phase-Locked Pulse Pairs

In the long pulse limit, we can neglect the DC components in equation 3.29 and write the effective Hamiltonian for the two-level system driven by phase-locked pulse pairs as

$$H_{eff} = \hbar \begin{pmatrix} \dfrac{\omega_B}{2} & -\Omega_R \cos(\delta t + \phi) \\ -\Omega_R \cos(\delta t + \phi) & -\dfrac{\omega_B}{2} \end{pmatrix}. \tag{3.29}$$

The reduced Hamiltonian is equivalent to the Rabi problem presented earlier. The relative phase of the pulse pair in the effective two-level system is equivalent to the overall phase of the driving field in the Rabi problem. With control of the relative phase and amplitude of phase-locked Raman pulse pairs, complete quantum control of the ground state dynamics of a Λ-system is possible.

3.3. Numerical Solutions based on the Optical Bloch Equations

Until this point, the discussion of light-matter interactions has centered on solutions to the Schrödinger equation. The intuitive results obtained in this approach do not, however, account for decays and decoherence. To include realistic decay rates for populations and coherences, it is helpful to use the optical Bloch equations (OBEs). Here we develop the set of equations that model the dynamics of our system.

The three-level system on which we model our experiments has the same polarization selection rule for both transitions, as discussed in Section 3.2.2. Therefore, to model the system we use equation 3.14 and coupling fields from equation 3.24 and 3.25. The Bloch equations can be written in the matrix form as,

$$i\hbar \frac{d}{dt}\rho = [H,\rho] + \Gamma(\rho), \tag{3.30}$$

where ρ is the density matrix, H is the Hamiltonian, and $\Gamma(\rho)$ is a matrix containing the phenomenological decay and decoherence terms. The density matrix ρ, written in the $\{|T\rangle, |+\rangle, |-\rangle\}$ basis, is

$$\rho = \begin{pmatrix} \rho_{ee} & \rho_{e+} & \rho_{e-} \\ \rho_{+e} & \rho_{++} & \rho_{+-} \\ \rho_{-e} & \rho_{-+} & \rho_{--} \end{pmatrix}.$$

(3.31)

To incorporate phenomenological decays we define the matrix

$$\Gamma(\rho) = \begin{pmatrix} -\Gamma\rho_{ee} & \gamma_e\rho_{e+} & \gamma_e\rho_{e-} \\ \gamma_e\rho_{+e} & \dfrac{\Gamma}{2}\rho_{++} & \gamma_{+-}\rho_{+-} \\ \gamma_e\rho_{-e} & \gamma_{+-}\rho_{-+} & \dfrac{\Gamma}{2}\rho_{--} \end{pmatrix},$$

(3.32)

where γ_e is the dipole decoherence rate, Γ is the population decay rate of trions to the two

spin states, and γ_{+-} is the spin decoherence rate.

To illustrate the spin dynamics governed by the OBE, with realistic decoherence

and decay rates included, we present two figures: one with experimental parameters for

decoherence and decay, Figure 3.10, and another where decoherence and decay are

ignored, Figure 3.11. The figures plot spin coherence versus time, for the electron-trion

Λ–type three-level system, driven by phase-locked Raman pulse pairs. The initial state of

the system is polarized in the $|-\rangle$ spin state. At time t=0 the pulse pair arrives and drives the

electron spin coherence. For a pulse area of π, the electron spin beats nearly vanish,

corresponding to the spins being rotated near the $|+\rangle$ spin state. The spin beats do not

vanish, however, because the pulse duration was set to $T_{sp}/T_{\omega B}=2$ in the simulation, which,

in Figure 3.9, reveals the maximum probability of transferring to the |+> state is ~0.8.

The effects of decay are represented by decrease in beat amplitude with increased

pulse area (rotation angle), in Figure 3.10, due to radiative coupling to the trion state.

These decays are not represented in Figure 3.11, where the decays are ignored. Further

simulations based on the OBE are incorporated in the experimental sections, and the code

for the simulations is included in appendix A.
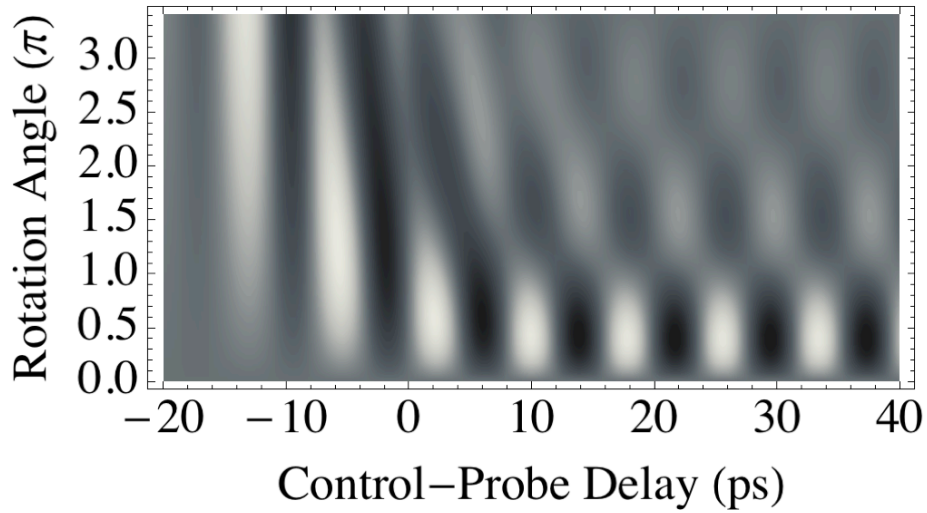
Figure 3.10. Simulation of spin coherence driven by a Raman transition. The pulse duration used is two times the Larmor period $T_{sp}/T_{\omega B}=2$. Dipole decoherence rate is 2 ps. Population decay rate is 1 ns. Spin decoherence time is set to 10 ns. The detuning is set to 1.5nm.
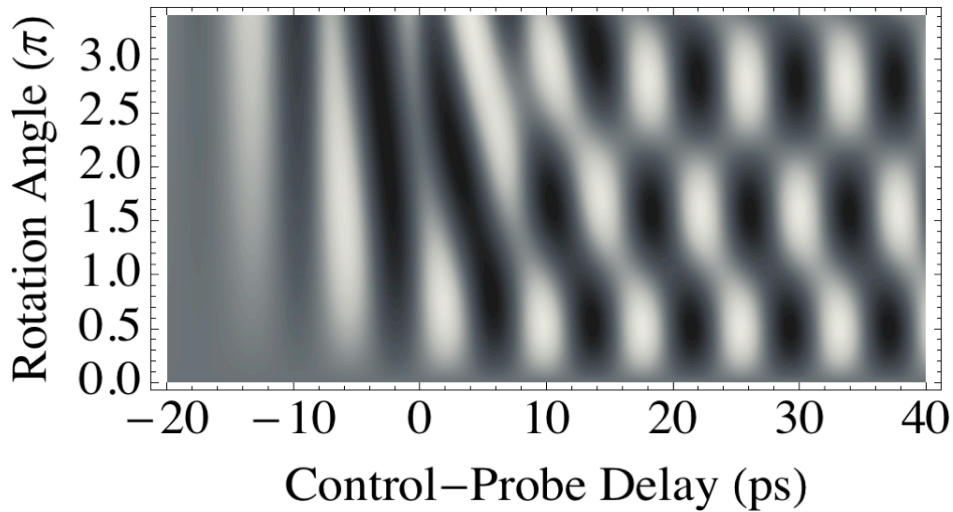
Figure 3.11. Simulation of spin coherence driven by a Raman transition. The pulse duration used is twice the Larmor period $T_{sp}/T_{\omega B}=2$. Decoherence rates are ignored.

3.4. Chapter Summary

We developed the theoretical description of optical control of the ground states in

Λ-type three-level systems via the adiabatic elimination of the excited state. Specific

attention was given to the polarization selection rules present in the electron-trion Λ-type

system. We showed that a single detuned pulse generates rotations about the optic axis,

and it must be short compared to the relative dynamics of the ground states (electron spin

states). We then presented complete control with phase-locked pulse pairs of a Λ-type

system, representative of the electron-spin trion system, and showed it could be reduced to

the Rabi problem. The effectiveness of the phase-locked Raman pulse pairs was shown to

improve in the simulations with longer pulses. We ended the chapter by introducing the

optical Bloch equations, which we used to account for decoherence and decay in modeling

the experimental results presented in Chapters V and VI.

CHAPTER IV

EXPERIMENTAL SETUP

In this chapter we introduce the essential components used in the transient pump-probe experiments presented in this dissertation, and we briefly describe the pulsed laser systems, pulse-shaping techniques, and geometries for two-pulse and three-pulse transient pump-probe experiments.

4.1. Laser Systems

The transient dynamics of the electron spins investigated in this work require ultrafast optical pulses. These optical pulses come from one of two mode-locked Ti:Sapphire lasers, the selection of which is specific to the experiment being performed. A (Spectra-Physics Tsunami) Ti:Sapphire laser that uses prisms for dispersion compensation and is pumped by a 532 nm 7 W diode pumped solid state laser (Coherent Verdi V-10) was employed for experiments that require optical pulses with large spectral bandwidth (7-8 nm). For experiments that required spectrally narrow laser pulses (~0.5 nm) and are tolerant of a slightly longer pulse duration (2 ps), we used a (Spectra-Physics Tsunami) Ti:Sapphire laser that uses a Gires-Tournois Interferometer (GTI) for dispersion control, a birefringent filter for wavelength selection, and is pumped by a 532 nm 5W diode pumped solid state laser (Spectra-Physics Millennia). Both laser systems have repetition rates near 80MHz and an average output power of approximately 1 W at 770 nm.

4.2. Spectral Pulse-Shaping

The temporal and spectral profiles of the optical pulses output by the Ti:Sapphire lasers are not optimal for coherent control experiments. We have used spectral pulse shaping to design laser pulses with spectral and temporal profiles optimized for coherent control. Spectral pulse-shaping is a time-invariant linear filtering process (*49*). A linear filter converts an input pulse, $e_{in}(t)$, to a desired output pulse, $e_{out}(t)$, by convolving the input pulse with an impulse response function, $h(t)$, of the filter. The linear filtering process can be written as

$$e_{out}(t) = \frac{1}{\sqrt{2\pi}} \int_{-\infty}^{\infty} H(\omega) E_{in}(\omega) e^{i\omega t} dt \tag{4.1}$$

where $E_{in}(\omega)$ and $H(\omega)$ are the Fourier transform of $e_{in}(t)$ and $h(t)$, respectively. In the limit that $e_{in}(t)$ is sufficiently short and can be approximated as a delta function, $e_{out}(t)$ is approximately given by the impulse response function, with $e_{out}(t) \propto h(t)$.
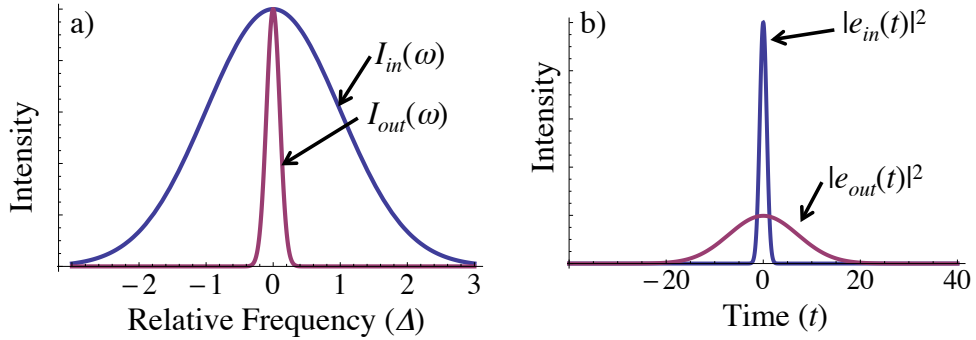
Figure 4.1. (a) Input intensity spectrum, $I_{in}(\omega)$, is plotted along with the output intensity spectrum, $I_{out}(\omega)$. (b) The temporal line-shape of the input and output pulse, $|e_{in}(t)|^2$ and $|e_{out}(t)|^2$.

To generate a single 2 ps optical pulse from a 150 fs pulse we use a single

Gaussian-like linear filter function

$$H(\omega) = \exp[-\frac{(\omega - \delta)^2}{2w^2}],$$
(4.2)

where w is the spectral width of the window, ω is the center frequency of the input pulse, and δ is the center frequency of the shaped pulse relative to ω. The spectra of a short input pulse and the corresponding output pulse are shown in Figure 4.1a. Figure 4.1b plots $|e_{in}(t)|^2$ and $|e_{out}(t)|^2$.

To generate phase-locked pulse pairs, we have used a linear filter with two Gaussian-like windows centered at $\omega \pm \delta/2$:

$$H(\omega) = \exp[-\frac{(\omega - \delta/2)^2}{2w^2} - i\frac{\phi}{2}] + \exp[-\frac{(\omega + \delta/2)^2}{2w^2} + i\frac{\phi}{2}]$$
(4.3)

where w is the spectral width of the window, and ϕ is the phase difference or the relative phase between the two windows. Figure 4.2a plots $H(\omega)$ for $\delta = 1$, $w = 0.1$, and $\phi = 0$. The spectra of a short input pulse and the corresponding output pulse are shown in Figure 4.2b. Figure 4.2c plots $|e_{in}(t)|^2$ and $|e_{out}(t)|^2$. Figure 4.2d shows the dependence of the output pulse on the relative phase of the impulse response function.
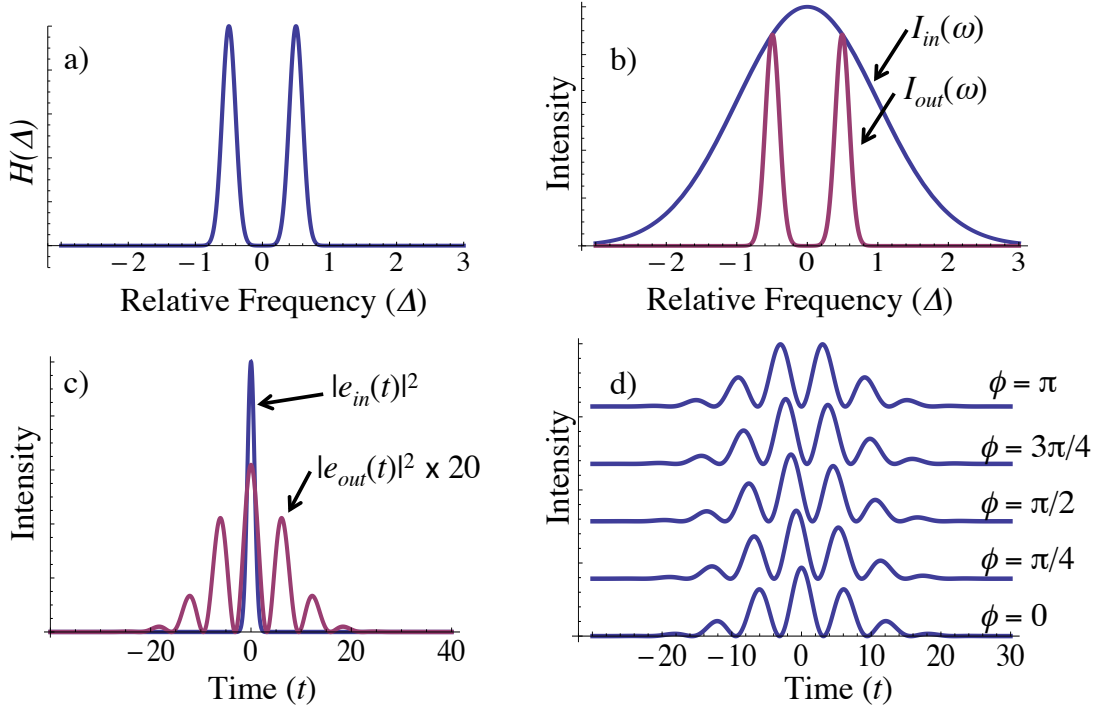
Figure 4.2. (a) $H(\omega)$ for $\delta = 1$, $w = 0.1$, $\phi = 0$. (b) The spectra of a short input pulse and (c) the corresponding output pulse $|e_{in}(t)|^2$ and $|e_{out}(t)|^2$. The same parameters are used for (a) to (c). (d) $|e_{out}(t)|^2$ at various relative phases, ϕ, for the impulse response function.

In order to generate the simple single Gaussian-like pulses involved with single pulse rotations discussed in Chapter V we used a grating based pulse-shaper (*49*) that is diagrammed in Figure 4.3. This pulse-shaper uses a 1200 line/mm blazed diffraction grating, a 30 cm spherical lens, and a mirror. The masking function H(ω) is defined by razor blades at the Fourier plane (directly in front of the mirror). The masking function is the convolution of a Rect function, defined by the razor blades, and a Gaussian-like function resulting from the resolvance of the diffraction grating. The number of diffraction lines addressed by the optical beam determines the resolvance of the diffraction grating,

$$R = \frac{\lambda}{\partial \lambda} \approx mN, \tag{4.4}$$

where λ is wavelength, $\partial \lambda$ is the m is the order of diffraction, and N is the number of lines

addressed on the diffraction grating. It is possible to resolve two wavelengths of separation

$\partial\lambda$ when $\partial\lambda \approx \lambda/mN$. Therefore, to shape spectrally narrow pulses one must address more

of the diffraction.
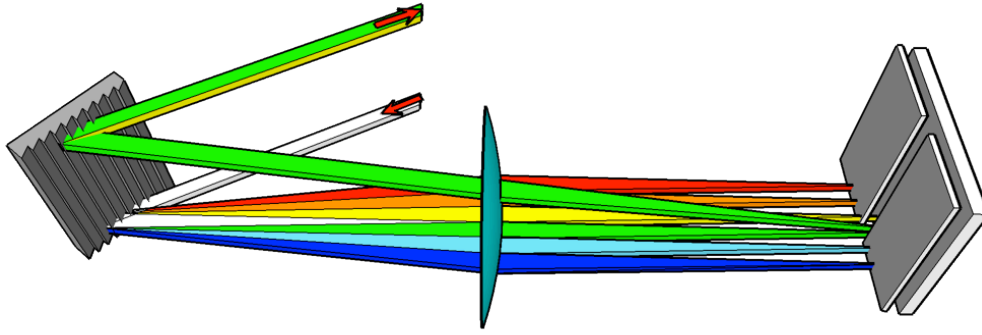
Figure 4.3. Schematic of a razor blade based pulse-shaper, shown with broad input spectra and narrow output spectra.

To generate the more intricate pulse designs required for coherent control with

phase-locked pulse pairs we use a programmable liquid crystal spatial light modulator

(LCSLM) in a grating-based spectral pulse-shaper similar to the one shown in Figure 4.3.

However, the design requires a cylindrical lens and a grating with higher groove density in

order to spread the laser pulse over more of the LCSLM surface. The LCSLM-based

pulse-shaper is shown schematically in Figure 4.4: an input pulse is dispersed by a

diffraction grating into its constituent frequency components, which are then focused to the

filtering plane by a cylindrical lens. The LCSLM, positioned at the filtering plane,

attenuates and phase-shifts each frequency component of the input pulse according to the

response function $H(\omega)$. To generate a phase-locked Raman pulse pair, the LCSLM

diffracts two portions of the input spectra, shown as red and green in Figure 4.4, toward the

top of the diffraction grating. The rest of the input pulse spectra is terminated at a beam

stop (not shown). The relative phase difference of the two pulses in the pulse pair is set by

their optical path length difference. The two diffracted spectral components are collimated

and combined by the lens and diffraction grating into a single output beam, shown as the

color yellow.
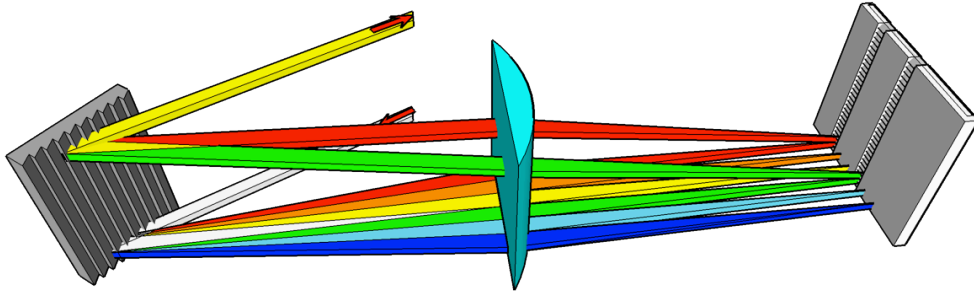
Figure 4.4. Schematic of a spectral pulse-shaper with a liquid crystal spatial light
modulator at the filtering plane.

For our experimental setup, we use a 2200 line/mm blazed grating, a 1 m focal

length cylindrical lens, and a phase-only LCSLM from Holoeye Inc. The transform-limited

input pulse featured is 2 ps in duration and has a central wavelength near 773 nm.

4.3. Cryostat and Magnetic Field

In order to extend the lifetime of the spins and more easily address them optically,

one must freeze out the effects of phonons, which broaden the optical transitions and

increase spin decoherence rates. Freezing out of phonons is possible by cooling the

semiconductor sample to cryogenic temperatures. To achieve this we have used two

cryostats to maintain sample temperatures near 5K. The selection of a cryostat is

dependent on the magnitude of the magnetic field required for a given experiment. One

cryostat is equipped with a liquid-helium cooled superconducting magnet that can be

operated safely up to 5.5T, and is used to generate large Zeeman splittings essential to the

control experiments presented in Chapter VI. A second cryostat was used for experiments that are suited for magnetic fields less than 0.5T, in which a rare earth magnet is sufficient to generate the required magnetic field. For these experiments a neodymium magnet was placed inside the cryostat and directly below the sample.

4.4. Transient Pump-Probe

To monitor the dynamics of the electron spins in the experiments presented in this dissertation we used optical pump-probe techniques that detect spin coherence. In our experiments, the absorption of the probe pulse is highly sensitive to the polarization of the electron spin ensemble. The pump pulse induces a spin polarization that evolves in time, and we use the probe to monitor the polarization of the spin ensemble as it evolves. The sensitivity of the probe to the effects of the pump allows us to conduct transient differential transmission (DT) measurements where the transmission of the probe pulse is monitored as a function of delay relative to the pump pulse. DT compares the transmission of the probe pulse through a sample when the pump pulse is on, to the transmission of the probe when the pump pulse is off. Typically this difference is very small. Therefore, to increase the sensitivity of our measurement we use a lock-in amplifier that monitors the DT signal at the chopping frequency of the pump laser. Figure 4.5 shows a schematic of a two-pulse experiment.
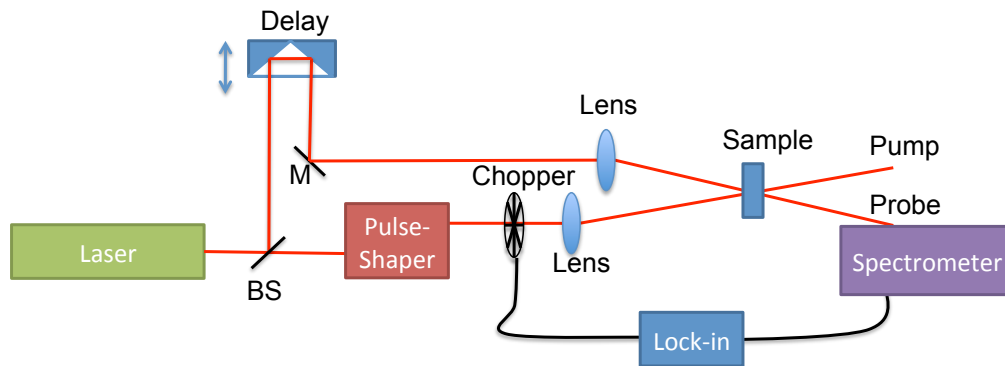
Figure 4.5. A schematic of a pump probe experiment. BS refers to beam splitter and M refers to mirror.

In Figure 4.5, the output pulse from a mode locked Ti:Sapphire laser is sent to a beam splitter where one path defines the probe pulse and the other defines the pump path. The pump path sends the laser through a pulse-shaper and a chopper before a lens focuses the laser on the sample. The probe pulse is retro-reflected from a mechanical delay stage before it is sent through the sample to the spectrometer. The intensity of the probe pulse is measured at a particular wavelength inside the spectrometer by a photo-detector that is connected to a lock-in amplifier. The relative delay between the two optical paths is varied by computer control of the mechanical delay stage.

In the event that a third pulse is required either for state preparation or for control of electron spins, the experimental setup is changed slightly from that in Figure 4.5. The three-pulse schematic diagram is shown in Figure 4.6, where the third beam is labeled control. The control beam path passes the beam through a pulse-shaper. The pump and probe both have delay stages to set the relative arrival times of the three pulses. Again, the pump pulse passes through a chopper, and the probe pulse is sent to the spectrometer where the signal is then measured through lock-in detection.

The probe pulse focused on the sample has a typical beam diameter of 30 μm while

the pump/control pulse has a focused beam diameter of roughly 150 µm. The control of

electron spins is highly dependent on the intensity of the control pulse; therefore, the probe

spot size must be significantly smaller than the control or pump in order to interact with as

uniform an intensity profile as possible. The intensity variation within the pump pulse

sampled by the probe pulse is less than 10%, given the approximate spot sizes for the

pump, control, and probe pulses stated above.

Circular polarized light monitors the electron spin polarization in the propagation

direction of the optical pulse. Therefore, to monitor spin polarization we have used

circularly polarized laser pulses in all our experiments. The output of the laser is linear;

therefore, a quarter wave plate was placed in each of the beam paths between the lens and

the sample to change the polarization of the laser pulses to make them circular. The quarter

wave plates are not shown in Figure 4.5 or Figure 4.6.
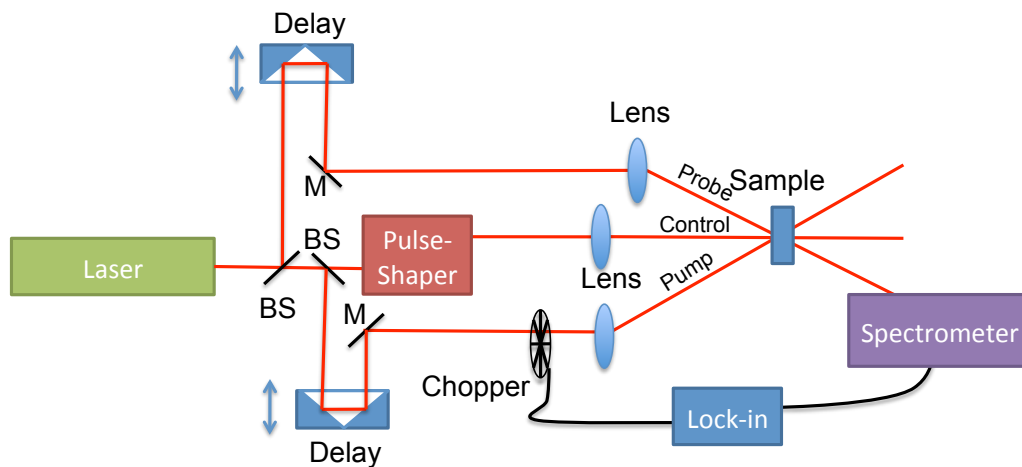
Figure 4.6. A schematic of a three-pulse pump probe experiment. BS refers to beam
splitters and M refers to mirrors.

4.5. *Chapter Summary*

In this chapter we introduced two-pulse and three-pulse transient pump-probe experiments. We discussed the laser systems and the pulse-shaping techniques used to design optical pulses for our experiments, and we briefly described the magnetic and cryogenic systems used.

CHAPTER V

OPTICAL SPIN CONTROL WITH A SINGLE ULTRAFAST PULSE

Some of the work reported in this chapter was co-authored by Carey Phelps. In this chapter, we report the experimental demonstration of complete electron spin flips in a 2D electron gas (2DEG) using a single off-resonant ultrafast optical pulse. The pulse is designed to drive a stimulated Raman transition between Zeeman split electron spin states $s=|\pm 1/2\rangle_z$, while avoiding the excitation of excitons and trions. The pulse may be equivalently understood as inducing an optical Stark shift of the $s=|\pm 1/2\rangle_x$ electron spin states (*31*).

By monitoring electron spin dynamics via differential transmission (DT), we show that the complete spin flip leads to spin precessions that are symmetric with respect to the arrival time of the effective π-pulse, described in Section 3.2.2.1. This symmetry also demonstrates the feasibility of using the ultrafast optical pulse for electron spin echoes (*21, 22, 37*). The experimental results on the electron spin flip agree with separate measurements of optical Stark effects and with theoretical analysis based on optical Bloch equations (OBE).

The experimental studies were carried out at 5 K in the high quality *n*-doped CdTe quantum well (QW) discussed in Chapter II. The linear absorption spectra in Figure 5.1 show well resolved heavy-hole exciton and trion resonances. An in-plane external magnetic field oriented along the z-axis (see Figure 2.6) sets the energy eigenstates for the electron spins where a σ+ (or σ−) polarized optical field couples the two electron spin states with $s=|\pm 1/2\rangle_z$ to a common trion state $|t_+\rangle$ (or $|t_-\rangle$). These optical dipole selection

rules are diagrammed in Figure 2.11.

The chapter begins by introducing the rotation pulse and demonstrates the spin-selective optical Stark shift induced by the rotation pulse. Next, we present the technique used to initialize spin coherence, and then we employ the control pulse to manipulate the spin polarization while monitoring the spin coherence. We end the chapter with numerical simulations based on the OBE for the electron-trion system detailed in Chapter III. The simulations are in strong agreement with the experimental results.

5.1. *Rotation Pulse*

From our theoretical description of single pulse rotations in Section 3.2.2.1, we know the pulse duration needs to be much shorter than the Larmor precession time for the electrons. The pulse also needs to be sufficiently short (compared with the dipole decoherence time) to avoid decoherence during the optical pulse. However, the duration also needs to be long enough that a rotation angle $\theta = \pi$ can be achieved at a relatively small optical Rabi frequency. As described in Chapter III, the optically induced spin rotation is proportional to the pulse area

$$\theta \propto \int |E(t)|^2 dt \; , \tag{5.1}$$

where *E(t)* is the temporal profile of the rotation pulse. For comparable pulse durations, a greater degree of spin rotation can be achieved with larger optical field amplitude.
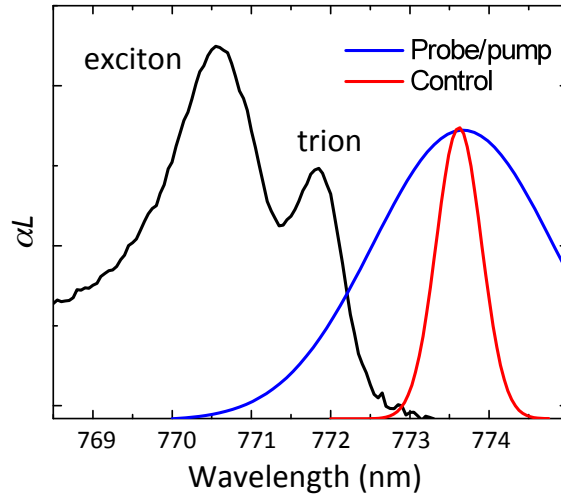
Figure 5.1. Absorption spectrum of the CdTe quantum well and the spectra for the control pulse (in red) and the pump and probe pulses (in blue).

For our experimental studies, we have chosen a spin-rotation pulse, or a control pulse, which features a duration $\tau_c = 2$ ps (bandwidth 0.5 nm) and is detuned 2 nm (4 meV) below the trion resonance. The control, absorption, and pump/probe pulse spectra are shown in Figure 5.1. All laser pulses were derived from the same femtosecond mode-locked Ti:Sapphire laser (repetition rate of 82 MHz). The control pulse was spectrally shaped by a razor blade based linear pulse-shaper discussed in Chapter IV and diagrammed in Figure 4.3.

5.2. Optical Stark Shift

The demonstration of spin-selective optical Stark shifts is an experiment that complements electron spin control with a single-pulse. The off-resonant coupling of the control pulse with polarization set to σ+ generates an optical Stark shift for $|s_x=1/2\rangle$, inducing a frequency separation, $\delta\omega(t)$, between $|s_x=1/2\rangle$ and $|s_x=-1/2\rangle$. The overall phase

66

shift θ between these two spin states is given as

$$\theta \propto \int |E(t)|^2 \, dt \propto \int \delta\omega(t)\, dt \ . \tag{5.2}$$

This phase shift corresponds to a spin rotation of an angle θ around the x-axis of the Bloch sphere. A diagram of the Bloch sphere, in Figure 5.2, shows the initial state vector oriented along the y-axis as it is rotated by an angle of $\theta=\pi$ about the x-axis, landing the state vector pointing in the -y-direction.
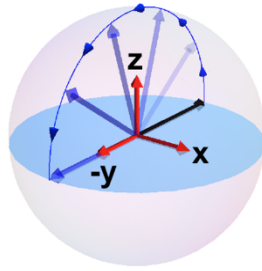
Figure 5.2. A Bloch sphere with a rotation of the state vector from y to −y, about the x-axis.

To demonstrate spin-selective optical Stark shifts with our 2 ps control pulse, we conducted a two-pulse experiment, similar to that diagrammed in Figure 4.5. However, the chopper was positioned in the probe path in order to directly observe the Stark shift in the absorption spectra. Optical Stark shifts are shown in the absorption spectra in Figures 5.3a and 5.3b. The absorption spectra were obtained with a spectrally broad (150 fs) probe that had the same circular polarization as the control pulse, σ+ circular polarization.
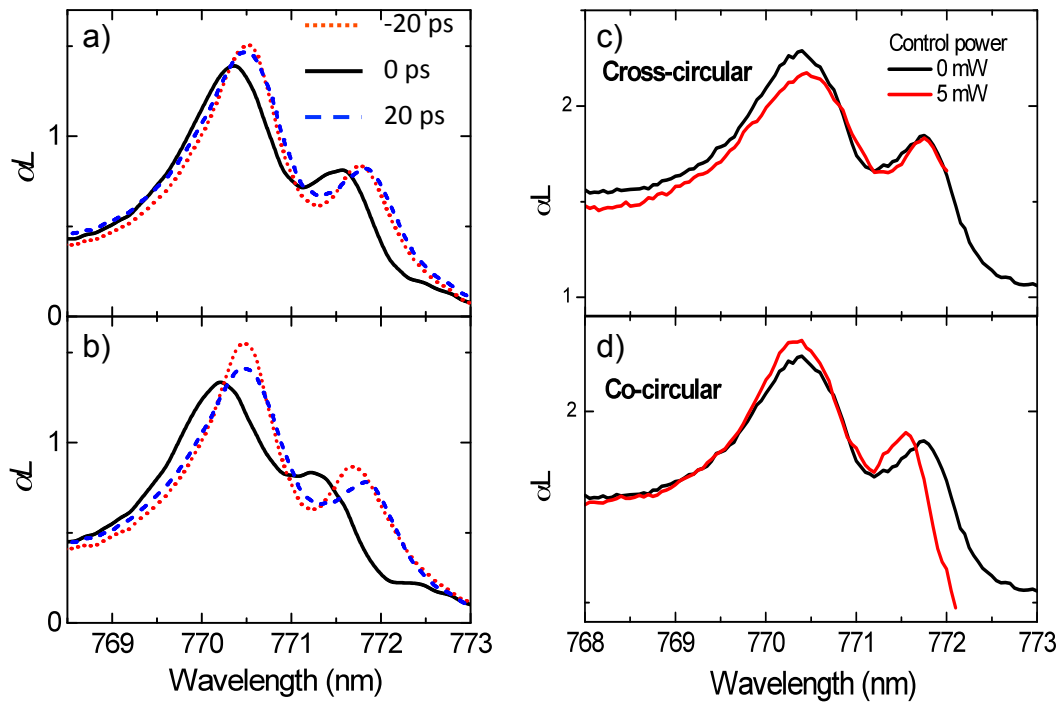
Figure 5.3. Stark shift of trion and exciton by 10 mW (a) and 20 mW (b) rotation pulse is shown with absorption spectra before (-20ps), during (0ps), and after (20ps) the rotation pulse. The absorption spectra during an optical pulse for cross-circular (c) and co-circular (d) is plotted (in red) along with the absorption spectrum without the optical Stark shift pulse.

Figure 5.3a shows three absorption spectra for various delays relative to the control pulse arrival time: -20 ps, 0 ps, and 20 ps. At zero delay the probe overlaps in time with the peak of the control $I_c = 20$ mW, and optical Stark shifts for the trion resonance become nearly comparable to the control pulse linewidth. As expected, the optical Stark shifts vanish when the probe arrives at 20 ps after the control, as shown in blue in Figures 5.3a and 5.3b. It should be noted that the shift in energy, shown in Figures 5.3a and 5.3b, due to the optical Stark shift is linear with rotation pulse intensity, which is consistent with equation 3.27.

Figure 5.3b also reveals minor bleaching for the exciton resonance and a noticeable

amount of bleaching for the trion resonance, indicating an appreciable excitation of trion

population by the control. No significant broadening of either the exciton or trion

resonances is observed in Figures 5.3a and 5.3b. Under these modest intensities, excitonic

excitations and resultant manybody effects remain relatively small. With $I_c = 20$ mW, the

estimated peak optical Rabi frequency is of the order of 2 meV.

Spin-selective optical Stark shifts are demonstrated in Figures 5.3c and 5.3d. This

is indicated by the absence of an optical Stark shift when the control and probe are cross-

circularly polarized (Figure 5.3c) but are revealed when the pulses are co-circularly

polarized (Figure 5.3d). The energy splitting between spin states induces an overall phase

shift between these two spin. This is the phase shift that corresponds to a spin rotation of

angle θ around the x-axis (equation 5.2).

5.3. Optical Spin Initialization

Spins can be initialized through thermal relaxation or optical pumping. Net thermal

polarization is a strong effect when the energy splitting of the spin states is large compared

to the thermal energy; however, at 0.4 T the energy splitting of the electron spin states in

CdTe is small in comparison to $k_B T$. The net thermal electron spin polarization is ~0.05

(where 1 is perfect polarization) in CdTe, given the experimental conditions (0.4 T and at a

temperature of 4.5 K). Therefore, optical pumping was used to initialize a small net spin

polarization.

The s_x electron spin states are energetically degenerate, and the steady state

population distribution of electron spins in the x-basis is equal. As shown in earlier studies

(*50, 51*), the excitation of $|T_+\rangle$ by a σ+ polarized pump leaves a net electron spin population

in the −x-direction $s=|-1/2\rangle_x$. The creation of $|T_+\rangle$ trions depletes the $s=|1/2\rangle_x$ electron

population, which is diagrammed in Figure 5.4. This results in a maximum initial net spin

polarization of ~0.5; however, the radiative decay of a trion results in the reintroduction of

an electron back into the net spin population, degrading the spin polarization induced by

the pump pulse.
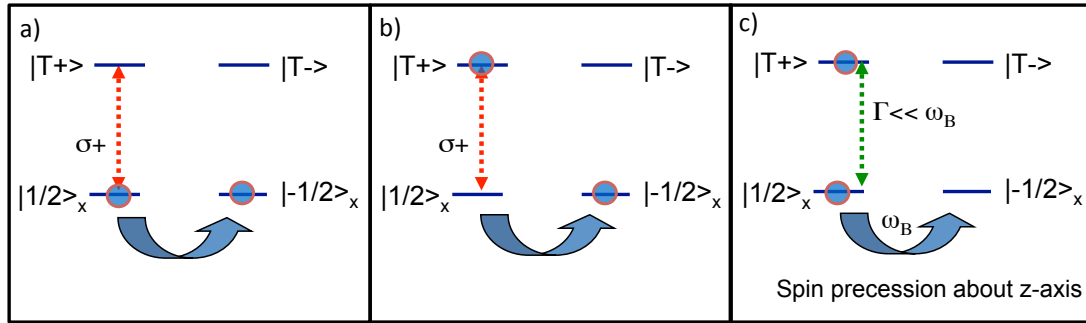
Figure 5.4. Polarization of spins by optically pumping. In (a) an optical pulse arrives that is
resonant with the trion $|T+\rangle$ and has σ+ polarization. Population is transferred to the trion
state in (b) because of the optical pulse, leaving a spin polarization in the −x direction. The
population decay rate (Γ) from $|T+\rangle$, shown in (c), is much slower than the Larmor
precession frequency (ω_B).

Our experiments were performed in the Voigt geometry (Figure 2.6c). Therefore,

when the pump initializes an electron spin polarization along the x-axis via the trion

creation (50-52), a transverse magnetic field applied along the z-axis induces precession of

the polarized spins around the external magnetic field axis. The precession about the z-axis

has a frequency ω_B and is known as Larmor precession. In the event the Larmor period is

much shorter than the population decay rate, the population decay from $|T+\rangle$ will contribute

electron spins throughout the precession process, resulting in a maximum net polarization

of ~0.25, ignoring spin decoherence.

5.4. Electron Spin Beats

The precession of electron spins about the magnetic field axis results in population oscillation between the $s=|\pm 1/2\rangle_x$ spin states. The absorption of $\sigma+$ polarized light at the trion resonance is dependent on the population of $s=|1/2\rangle_x$ spins. As a result, the absorption of a $\sigma+$ laser pulse at the trion transition is greater when the spin population is in the $s=|1/2\rangle_x$, than when the spins are in the $s=|-1/2\rangle_x$. Therefore, monitoring the transmitted intensity of a $\sigma+$ polarized laser pulse tuned to the trion resonance will detect spin beats that correspond to spin precession about the z-axis.

To observe spin precession we derived an initialization laser pulse (pump) and the detection laser pulses (probe) from a femtosecond mode-locked Ti:Sapphire laser (repetition rate of 82 MHz). The probe was spectrally resolved in a spectrometer after propagating through the sample. The change in the probe transmission, as a result of spin precession initiated by the pump, was measured at the trion resonance with lock-in detection. This two-pulse experiment is diagrammed in Figure 4.5.

In the presence of a transverse external magnetic field (B=0.4 T), periodic oscillations, or spin beats, with $2\pi/\omega_B$=116 ps were observed at the trion resonance when monitored in transient differential transmission (DT) (*52*), as shown in Figure 5.5. The phase of the oscillation also indicates the direction of the spin polarization in the x-y plane.

The probe monitors the spin polarization along the x-axis. Thus, the maximums in Figure 5.5 correspond to population in $s=|-1/2\rangle_x$ (-x direction), and the troughs correspond to population in $s=|1/2\rangle_x$ (+x direction). The polarization along the y-axis is inferred as the midpoints between the peaks and troughs, as shown in the inset of Figure 5.5.
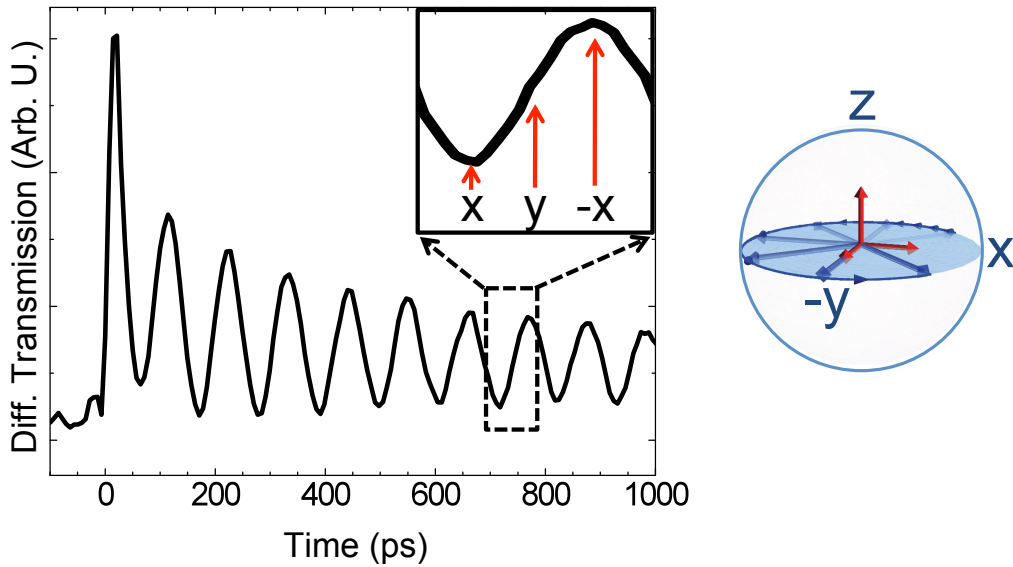
Figure 5.5. Quantum beats observed for σ+ polarization of pump and probe in a magnetic field of 0.4T. The beats correspond to the x-projection of the spin in the Bloch sphere, pictured to the right. The inset indicates the orientation of the spins in the Bloch sphere picture as it relates to the phase of the beats.

5.5. Electron Spin Flip: Intensity Dependence

To demonstrate coherent rotations of the electron spin ensemble we include the control pulse used in the optical Stark shift experiments in the spin beats pump-probe experiment. This three-pulse experiment is diagrammed in Figure 4.6. The control, applied at a fixed delay after the pump, induces an electron spin rotation about the x-axis. Therefore, timing of the control pulse is crucial to observe rotations. A rotation about the x-axis for a spin polarization along the x-axis should not result in a rotation of the spin state. However, when the spin polarization is along the y-axis, as shown in the Bloch sphere in Figure 5.2, a rotation is possible.

We set the arrival time of the control pulse to $5\pi/2\omega_B$ after the pump pulse, which corresponds to the spin polarization along the y-axis. We set the pulse duration to 2 ps and varied the intensity of the control pulse, and monitored the amplitude of the spin beats to

infer the degree of rotation obtained for a given pulse power.

For the experimental results presented here, the pump and probe have the opposite circular polarization, and the control and probe have the same circular polarization. The trion density excited by the pump is kept below $\sim 2 \times 10^9 /\text{cm}^2$. The spot sizes for the pump, probe, and control are estimated at 3×10^{-5}, 1×10^{-6}, 2×10^{-5} cm^2, respectively. An average control power, $I_c = 1$ mW, corresponds to an energy flux per pulse of 0.6 $\mu \text{J}/\text{cm}^2$.
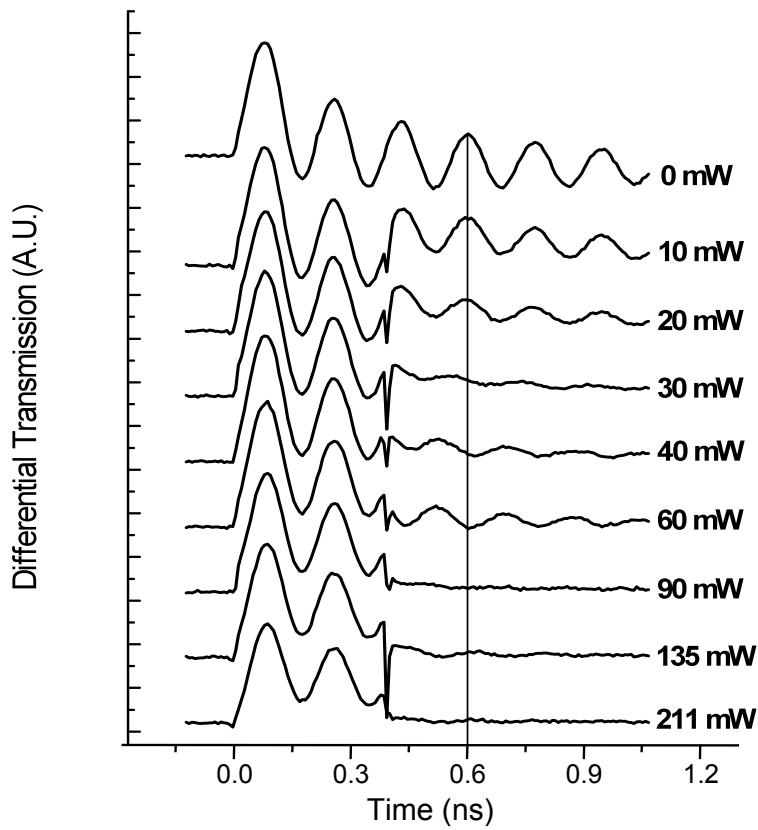
Figure 5.6. Dependence on the intensity of the control pulse for pulse arrival set to $5\pi/2\omega_B$. The vertical line positioned at 0.6 ns is meant as a guide to the eye.

As shown in Figure 5.6, the rotation of the spin polarization about the x-axis by a 30 mW rotation pulse results in a near absence of spin beats and corresponds to the spin polarization along the magnetic field axis, the z-axis, and a rotation of $\pi/2$. As the rotation

pulse power is increased from 30 mW to 60 mW we observe a revival of the spin beats; in this case, the beats are out of phase by π, which corresponds to a rotation greater than π/2. The pulse area corresponding to 60 mW is considered a π-pulse. Increasing the power to 90 mW the beats vanish once again, which corresponds to a rotation of 3π/2.

Because of the increasing control power, the spin-beat amplitude after the control pulse exhibits an oscillatory behavior, corresponding to the Rabi oscillation of the spin population. With the exception of the DT response obtained with the highest control intensity in Figure 5.6, the phase of the spin beats remains either unchanged or changed by π, as we expect from the spin rotations about the x-axis when spin is initially polarized along the y-axis.

The spin rotations observed in Figure 5.6 are in general agreement with the separate measurement of optical Stark shifts shown in Figure 5.3. The fidelity of the spin rotation and the non-π phase shift in the spin precession will be discussed in detail later. It should be noted that optical Stark effects, and thus the degree of spin rotation, are no longer proportional to the control intensity when the optical Rabi frequency for the control becomes comparable to the control detuning.

5.6. Timing of the Control Pulse

As explained above, the arrival time of the control pulse relative to the pump pulse plays a significant role in observing coherent rotations. Figure 5.7 shows the temporal evolution of the spin polarization when the control pulse, with pulse area π, arrives at four different delays, which correspond to a control pulse arrival time when the spin polarization is in +x (Figure 5.7a), -x (b), +y (c), and –y (d). Clearly shown in Figures 5.7a and b, the

beat phase remains unchanged when the control is applied at a delay of $3\pi/\omega_B$ and $4\pi/\omega_B$ after the pump, when the spins are aligned along the x-axis. In contrast, as shown in Figures 5.7c and 5.7d, when the control pulse is applied at a delay of $7\pi/2\omega_B$ and $5\pi/2\omega_B$ after the pump (when the polarization is along the y-axis) the control induces a π rotation, changing the beat phase by π.
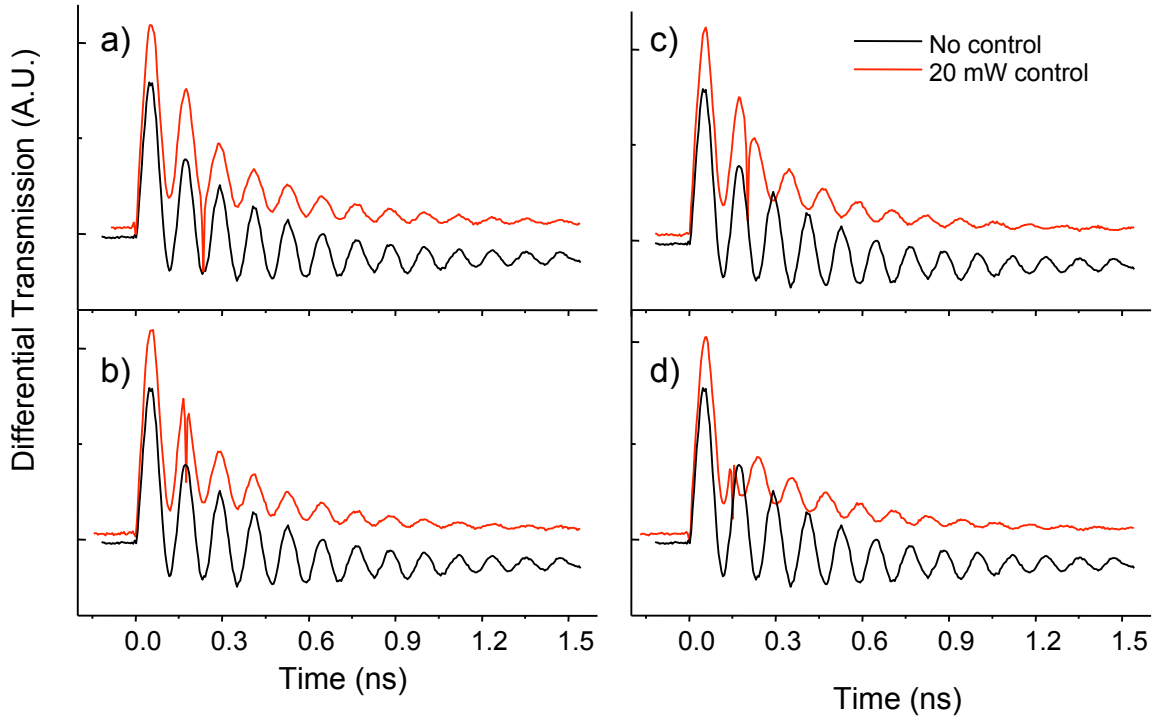
Figure 5.7. The beats with the control pulse (red) and with out (black) are plotted for four different control pulse arrival times. Control pulse arrival time when spins are in +x (a), -x (b), +y (c), and −y (d). The beat phase remains unchanged when the control arrives when the spins are aligned along the x axis (a and b), while the phase of the beats changes by π when the control pulse arrives when the spins are aligned along the y axis (c and d).

A unique signature of a complete electron spin flip is that the spin precession is symmetric with respect to the arrival time of the spin-flip pulse, as illustrated in Figure 5.8a. It is this symmetric spin evolution that leads to the formation of spin echoes. Figure 5.8a shows transient DT responses obtained with a control pulse, with a pulse area of π, at

various fixed pump-control delays. For clarity, the DT responses are plotted as a function of the control-probe delay instead of the pump-probe delay. As shown in the figure, the phase of the spin precession is symmetric with respect to the control-probe delay, regardless of the arrival time of the control. This symmetric spin dynamic induced by the control pulse not only represents a direct and remarkable manifestation of the complete spin flip, it also demonstrates the feasibility of using an ultrafast optical pulse for electron spin echoes (22, 37).
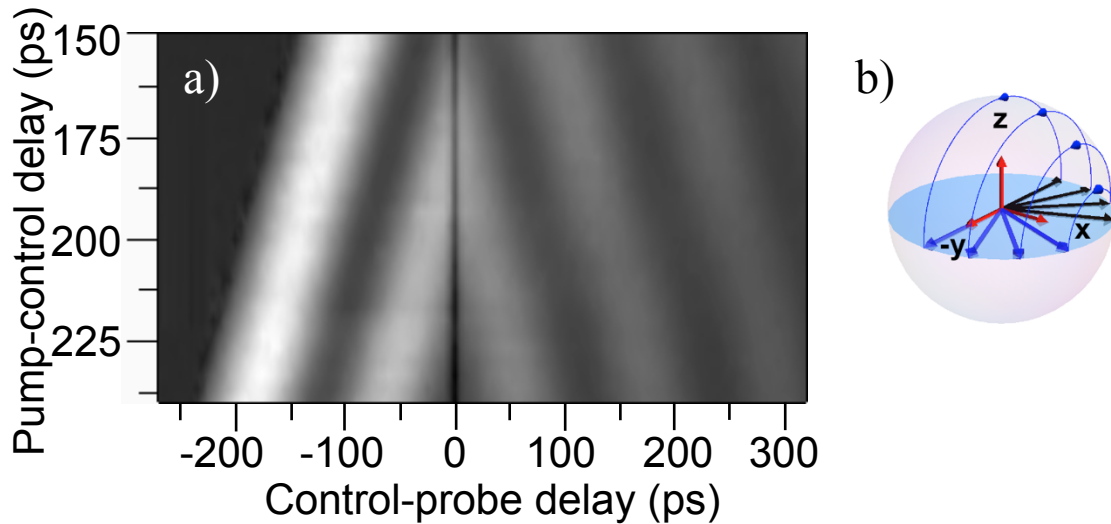
Figure 5.8. (a) Transient differential transmission as a function of the control-probe delay, obtained at various fixed delays between the pump and a π-control pulse. The phase of the spin precession is symmetric with respect to the arrival time of the control, demonstrating that the control pulse induces a complete spin flip with respect to the x-axis. (b) A Bloch sphere representing rotations about the x-axis for various vectors in the x-y plane.

5.7. Comparison with Theory

We have theoretically analyzed the electron spin rotation via an off-resonant control pulse by using the OBE associated with the energy level structure shown in Figure 2.11 (53). For the calculation, the system is initialized such that the spin population at t=0 is at s=$|-1/2\rangle_y$. A control pulse with a temporal Gaussian line shape and a duration of 2 ps

is then applied at a detuning of 4 meV below the trion resonance. For simplicity, we have ignored inhomogeneous broadening. Other parameters include dipole decoherence rate $\gamma = 2$ ps^{-1}, spin decoherence rate $\gamma_s = 0.005$ ps^{-1}, and excited state population decay rate $\Gamma = 0.001$ ps^{-1}.

Figure 5.9 shows the calculated temporal evolution of the population difference between the $s = |\pm 1/2\rangle_x$ spin states. The calculation describes well all the important features of the experiment results presented in Figure 5.6. Figure 5.9 plots the dependence of the spin dynamics on the intensity of a control applied at $t_{control} = 9\pi/2\omega_B$. Because dipole decoherence is enhanced during the optical interaction, the control not only induces a spin rotation via optical Stark effects, but it also excites a residual trion population that persists after the passage of the control. It is this residual trion population that leads to the reduction in the fidelity of the spin rotation in Figure 5.6 and Figure 5.7 and also to the small bleaching of the trion absorption in Figure 5.3. The excitation of the residual trion population also initializes an additional spin-polarization, which precesses in the x-y plane with a phase determined by $\omega_B(t - t_{control})$. A control with a relatively high intensity can thus induce a pronounced phase shift (other than π) in the spin precession, as shown in Figure 5.6.
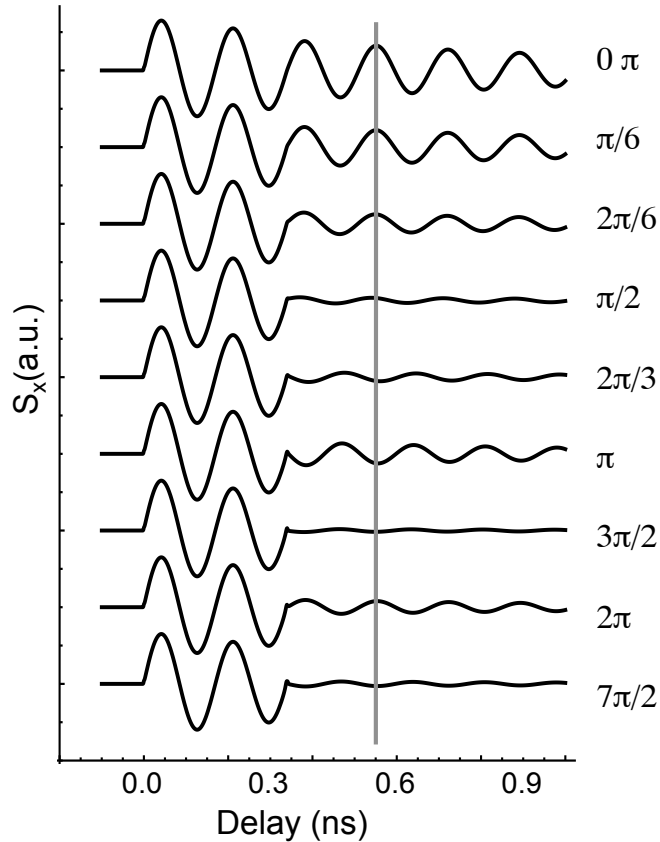
Figure 5.9. Theoretical calculation of intensity dependence of rotation pulse for single pulse rotations. Vertical line is a guide for your eye which helps show that beats nearly vanish for rotations of π/2 and 3 π /2.

Figure 5.10 plots the dependence of the spin dynamics on the timing of the spin-flip control pulse. In contrast to Figure 5.8, it shows a slight asymmetry with respect to the arrival time of the control. This asymmetry arises from the phase shift in the spin precession induced by the control-initialized spin polarization, as discussed above. The phase shift depends on the timing of the control, leading to the slightly curved pattern in Figure 4b. Note that the asymmetry is more pronounced in the theory than in the experiment, since, to underscore the effects of the residual trion population, we have used a dipole decoherence rate in the calculation that significantly exceeds the actual decoherence rate (near 1 ps^{-1}). The asymmetry of the spin evolution provides a sensitive measurement of the fidelity of the spin flip.
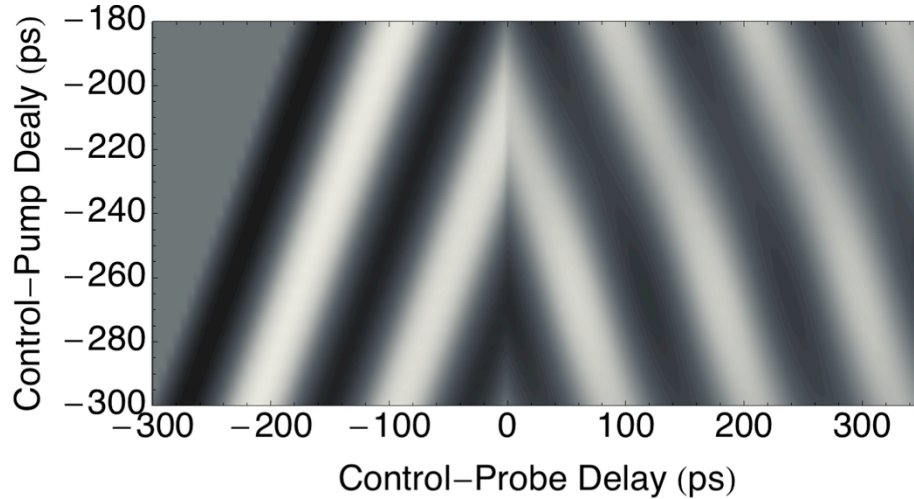
Figure 5.10. Numerical simulations of spin coherence based on the OBEs. The arrival time of the pump pulse is linearly varied relative to the control pulse, which arrives at zero delay. The spin beats after the control pulse show decreased amplitude, as a result of coupling to the excited state and are mirrored about the control arrival time.

5.8. Magnetic Field Dependence

In order to observe the effectiveness of a control pulse as a function of Zeeman splitting, we conducted a series of pump-probe experiments on the CdTe QW in a superconducting magnet cryostat. The transient differential transmission experiments were designed to monitor spin beats induced by a single control pulse, which was designed to tip the spin polarization away from the magnetic field axis (z-axis) into the x-y plane.

The steady state polarization of the spin ensemble was assumed to have a net thermal polarization, as derived from Boltzmann statistics, and plotted in Figure 6.2. The temperature of the sample was kept at 4.5 K, and the magnetic field magnitude was stepped from 1 T to 5 T. The rotation pulse used was detuned by 2 nm, had a duration of 3 ps, and a pulse area of $\pi/2$. Figure 5.11a shows two transient differential transmission traces. The spin beat frequency and amplitude at 5 T is measurably larger than at 1 T. The frequency of the spin beats is proportional to the Zeeman splitting, where $E_{Zeeman} = h\nu$, and ν is the beat frequency. Figure 5.11b plots the Zeeman splitting versus the applied magnetic field,

obtained from analyzing the spin beat period at 5 different magnetic field strengths. We

see the Zeeman splitting increases linearly with the magnetic field strength, which is

expected from equation 2.27.
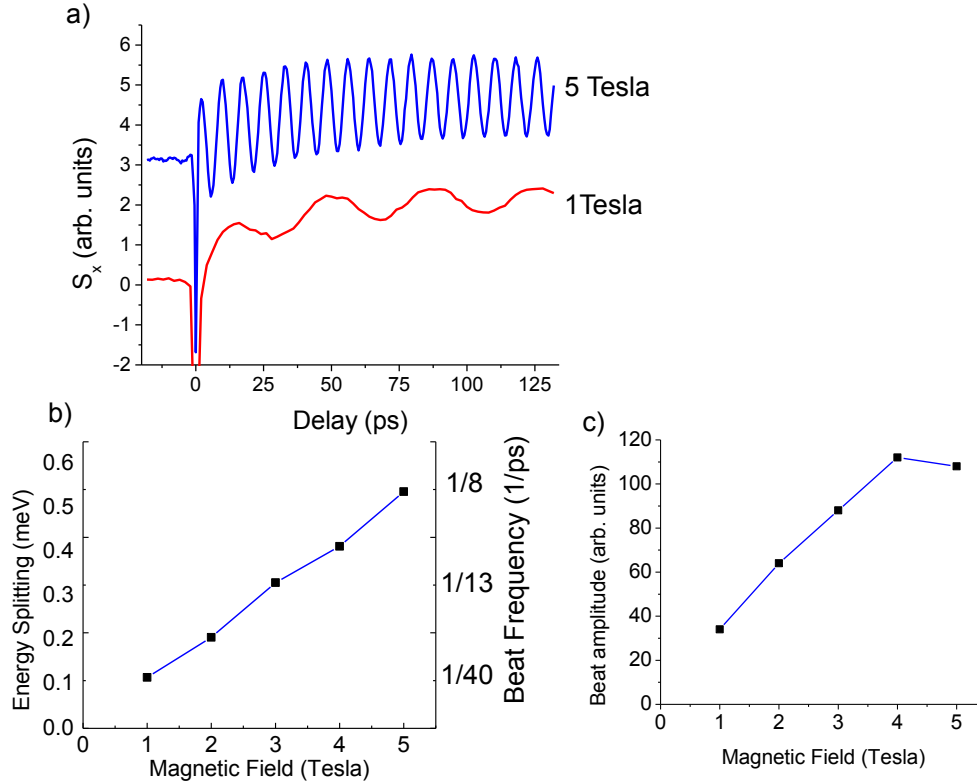
Figure 5.11. The spin beat dependence on magnetic field strength for a rotation pulse of 3ps duration, detuned from the trion state by 2nm, and a pulse area of $\pi/2$. (a) The transient DT signal in a magnetic field of 1T and 5T. (b) The frequency of the beats in units of energy versus magnetic field strength. (c) The beat amplitude as a function of energy splitting.

The second important feature observed in the spin beat data is the amplitude of the

beats. Figure 5.12c plots the average amplitude of the spin beats, measured between a delay

of 50 ps and 125 ps after the rotation pulse. The spin beat amplitude at 5 T is lower than

the spin beat amplitude at 4 T, which is counterintuitive when one assumes that the spin

beat amplitude should follow Boltzmann statistics. This assumption is flawed; it does not

consider the effectiveness of the rotation pulse when the pulse duration becomes

80

comparable to the Larmor precession time. From Figure 3.6, we know that when the pulse

duration becomes comparable to the precession time the effectiveness of the rotation is

degraded.
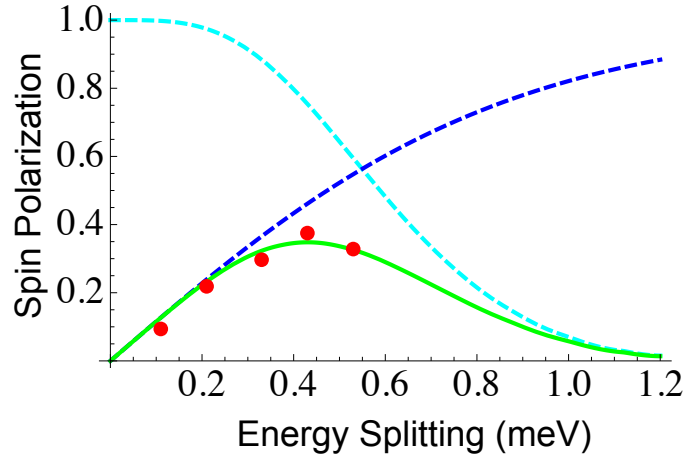
Figure 5.12. Theoretical model of spin beat amplitude as a function of Zeeman splitting for a rotation pulse of 3ps duration, detuned from the trion state by 2nm, and a pulse area of $\pi/2$. The blue dashed trace is theoretical thermal polarization. The dashed cyan curve is the theoretical amplitude of the spin beats for the given pulse. The green curve is the maximum polarization in x-y plane given the initial polarization and rotation pulse. The red dots are the experimentally measured beat amplitude at various Zeeman splittings, scaled to overlap with the green curve.

In order to account for the effectiveness of a pulse rotation into the x-y plane, we

modeled the spin beat amplitude for a pulse with area $\pi/2$ and a duration of 3ps, as a

function of Zeeman splitting. The red dots are the spin beat amplitudes taken from Figure

5.11c and plotted in units of the Zeeman splitting instead of the magnetic field strength.

Shown in Figure 5.12, the cyan dashed line plots the theoretical amplitude of the

spin beats for the 3 ps rotation pulse as a function of Zeeman splitting, assuming all spins

are initially polarized along the z-axis and neglecting decoherence. The effectiveness of the

spin polarization after the tipping pulse is theoretically high at small energy splittings $E<$

0.1 meV, because polarization in the x-y plane is near unity. However, the effectiveness of

81

the rotation pulse degrades when the Zeeman splitting becomes greater than the spectral bandwidth of the 3 ps pulse, which is ~0.6 meV. The dashed blue curve is the assumed initial thermal polarization of the spins based on Boltzmann statistics. The product of the initial polarization (blue) with the effectiveness of the rotation (cyan) results in the maximum spin polarization in the x-y plane as a function of Zeeman splitting and is plotted in green in Figure 5.12.

The measured x-y polarization (red dots) follows the theoretical prediction for polarization (green curve), when scaled appropriately. Based on the theoretical model, the green curve in Figure 5.11c shows that the spin beat amplitude at an energy splitting of 0.5 meV (or 5 T) should be smaller than the beat amplitude at 0.4 meV (or 4 T).

We clearly observe a dependence on the effectiveness of a rotation pulse when the period becomes comparable to the Larmor precession time. The decrease in the beat amplitude at 5T is a result of a 3ps pulse attempting to rotate the spin population away from the z-axis. The Larmor period at 5 T is ~8 ps; with this precession period a 3 ps pulse is too slow to effectively rotate the spin population about the x-axis because the spin precession during the pulse is non-negligible. However, the 3 ps rotation pulse is able to rotate the spin polarization quite effectively at the lower magnetic field strength of 1 T, where the Larmor period is ~40 ps.

5.9. Summary

By employing an off-resonant control pulse that induces an optical Stark shift for the trion resonance but avoids the excitation of excitons, we have successfully realized the complete spin flip of electrons in a 2D electron gas. The spin flip experiments are well

described by a theoretical analysis based on the OBE. We showed that the effectiveness of the single pulse rotation degrades when the pulse duration becomes comparable to the Larmor precession time. The complete spin flip leads to spin precessions that are symmetric with respect to the arrival time of the control, demonstrating the feasibility of using the ultrafast optical pulse for electron spin.

CHAPTER VI

OPTICAL SPIN CONTROL WITH PHASE-LOCKED

RAMAN PULSE PAIRS

Some of the work reported in this chapter has been peer reviewed and will be

published in a *Physical Review B,* and was co-authored by Carey Phelps. In this chapter,

we report the experimental demonstration of complete control of electron spins in a 2D

electron gas (2DEG) using a pair of detuned, phase-locked Raman resonant pulses. With

full control of the intensity and the relative phase of the pulse-pair, we are able to drive a

spin-flip Raman transition and completely control the electron spin polarization

Monitoring electron spin dynamics via differential transmission (DT), we show that

the phases of the spin beats are determined by the relative phase of the phase-locked

Raman pulse pairs. Also, we show coherent Rabi oscillations of the electron spins, which

result from the phase-locked Raman pulse pairs acting like an effective RF field driving the

electrons resonantly.

Complete control of electrons was performed in a 2DEG in a modulation-doped

CdTe quantum well (QW), which is discussed in Chapter II. The experimental studies were

carried out in a liquid helium superconducting magnet cryostat, and the CdTe QW sample

was kept at 5 K. The linear absorption spectra in Figure 6.1 shows well resolved heavy-

hole exciton and trion resonances. The field of the superconducting magnet was applied in

the Voigt configuration to generate an in-plane magnetic field oriented along the z-axis.

The magnetic field thus sets the energy eigenstates for the electron spins in the field

direction, where a σ+ (or σ−) polarized optical field couples the two electron spin states with $s=|\pm1/2\rangle_z$ to a common trion state $|T_+\rangle$ (or $|T_-\rangle$). These optical dipole selection rules are diagrammed in Figure 2.11.

For our experimental studies, σ+ circularly-polarized Raman pulse pairs were used to drive two $s=|\pm1/2\rangle_z$ electron spin states by coupling to a virtual excited state detuned from the trion resonance $|T_+\rangle$, as shown schematically in Figure 3.5(b). At low temperature, the trion resonance in the CdTe QW sample is characterized by an inhomogeneously broadened linewidth of 1.6 meV (0.8 nm) and a trion binding energy of 2.5 meV (1.25 nm), as shown in Figure 6.1. Experimental studies presented here were all carried out at a temperature of T= 5 K and a magnetic field strength of B=5 T, unless otherwise specified. Under these conditions, $k_B T /(\hbar\omega_B)= 0.8$, a net spin polarization along the magnetic field axis is present at thermal equilibrium.

The chapter begins by introducing the phase-locked Raman pulse pairs, followed by a description of thermal polarization of the electron spins at modest magnetic fields. We then demonstrate the mapping of the relative optical phase onto the phase of the electron spin coherence. We end the chapter with the demonstration of coherent Rabi oscillations between spin states driven by phase-locked Raman pulse pairs, which act like an effective RF field driving the spins directly. The experimental results of coherent control of the electron spins are in good agreement with theoretical analysis based on optical Bloch equations (OBE).

6.1. Phase-Locked Raman Pulse Pairs

We have used a grating-based optical pulse-shaper to generate phased-locked

Raman pulse pairs, which is diagrammed in Figure 4.4. A programmable spatial light

modulator controls the spectral bandwidth, spectral separation, and relative phase of the

two optical pulses. In principle, the intensity of the pulse pairs may be controlled with the

spatial light modulator; however, the intensity of the pulse pair was controlled with an

attenuator positioned on the input of the pulse-shaper. Figure 6.1 shows a typical spectrum

of a Raman pulse pair used in the spin rotation experiments. The two pulses feature nearly

the same intensity and spectral width (0.1 nm), and the spectral separation of the two pulses

(0.25 nm or 0.5 meV) is set to match the spin splitting at 5T.
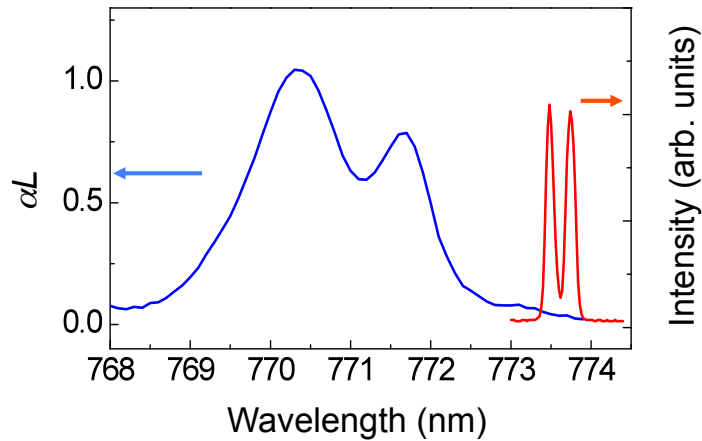
Figure 6.1. Absorption spectrum of the CdTe quantum well (in blue) and the spectra for
the phase-locked Raman pulse pair (in red).

6.2. Thermal Spin Initialization

A net thermal polarization of the electron spins is possible if the Zeeman splitting is

sufficiently large compared to the thermal energy. The spin polarization of a 2DEG in

CdTe at 4.5 K was calculated based on Boltzmann statistics and is plotted in Figure 6.2.

The relatively large electron g-factor for CdTe, which is roughly three times larger than

that of GaAs, results in the energy splitting of the electron spins of 0.5meV for a magnetic

field strength of 5T. At 5T the net thermal spin polarization is ~0.6, where a polarization of

1 corresponds to complete spin polarization, as indicated by a red arrow in Figure 6.2.
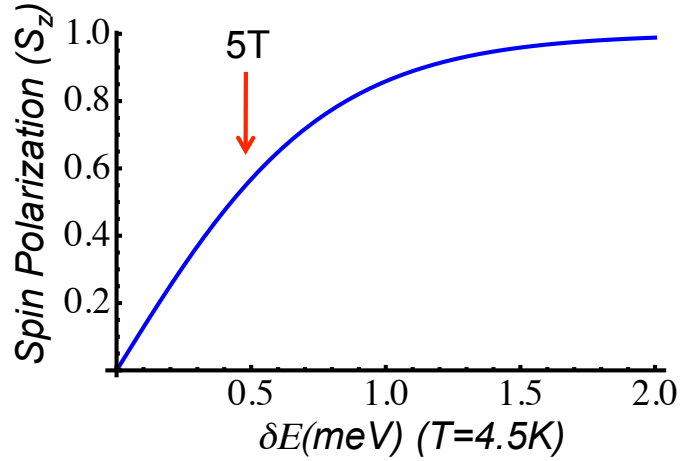
Figure 6.2. Calculated polarization of electron spins from Boltzmann statistics.

6.3. Driven Electron Spin Coherence

With the spin polarization thermally initialized along the z-axis, the phase-locked

Raman pulse pairs (control pulse) were used to coherently rotate the spin ensemble away

from the z-axis. As in the two-pulse experiments discussed in Chapter V, we use the

absorption of $\sigma+$ polarized light at the trion resonance to detect the population of spins in

the $s=|1/2\rangle_x$ state. When the spin population is polarized in the $s=|-1/2\rangle_x$ direction, the

$\sigma+$ laser pulse is absorbed less than when the spin polarization is in the $s=|1/2\rangle_x$. Therefore,

oscillations in the transient differential transmission (DT) signal monitored at trion

resonance will correspond to spin precession about the magnetic field axis, the z-axis. The

control and detection laser pulses (probe) are derived from a 2 ps mode-locked Ti:Sapphire

laser (repetition rate of 82 MHz). After propagating through the sample, the probe is

spectrally resolved in a spectrometer. The change in the probe transmission induced by the

phase-locked Raman pulse pair is measured at the trion resonance with lock-in detection, as

diagrammed in the two-pulse experiment in Figure 4.5.
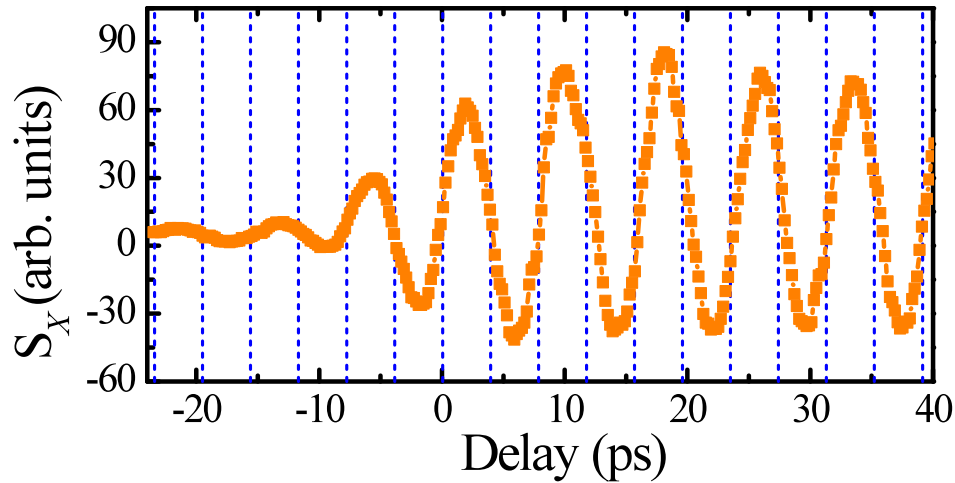
Figure 6.3. Spin beats measured in transient Differential Transmission at the trion resonance. The beats are measured as a function of delay between a phase-locked Raman pulse pair and a probe pulse.

A pair of phase-locked Raman pulses set to generate a rotation of $\theta = \pi/2$, with a detuning 1 nm below the trion resonance, resulted in the spin beats shown in Figure 6.3. The Larmor precession of the electron spin polarization around the external magnetic field (B=5 T) resulted in periodic oscillations, or spin beats, with a period of $2\pi/\omega_B$=8 ps in the transient DT response monitored at the trion resonance, as shown in Figure 6.3. The phase of the oscillation is directly related to the relative phase of the Raman pulse pair.

6.4. Mapping Optical Phase onto Spin Polarization

An important feature of resonantly driving any two-level system is that the phase of the coherence is determined by the phase of the driving field. In a Raman transition, the relative phase of the optical fields sets the phase for the effective driving field. Here we demonstrate the mapping of the relative phase of the optical pulses onto the phase of the electron spin coherence. First in Figure 6.4, we show the results for two different sets of

pulses pairs: one with the relative phase of the optical pulses set to zero, and the second

with a relative phase set to π. When the phase difference between the two pulses is set to π,

the spin beats generated are π out of phase with the beats generated by a effective driving

field with relative phase equal to zero. This is consistent with the Rabi problem, as

discussed in Chapter III.
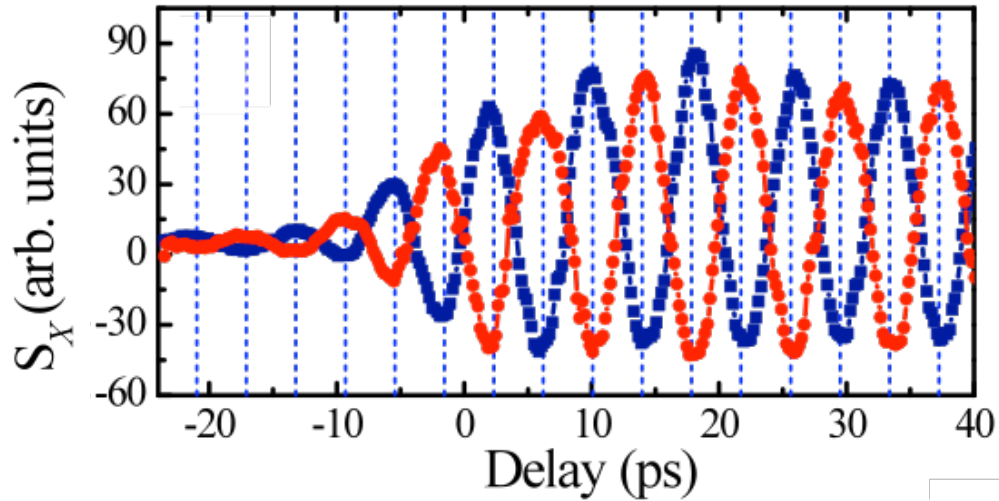
Figure 6.4. Transient DT measurement shows spin precession about z-axis (magnetic field axis) induced by spin rotations from phase-locked Raman pulse pairs with relative phase equal to 0 (blue) and π (red).

Figure 6.5 shows the dynamics of S_x, the electron spin polarization projected along

the x-axis, as the relative phase of the pulse pair ϕ is stepped incrementally from -2π to 2π.

The area of the Raman pulse pairs was set to generate a rotation of $\theta = \pi/2$, with the pulse

detuned 1 nm below the trion resonance. Figure 6.5 shows a clear linear dependence of the

phase of the spin coherence on the relative phase ϕ of the phase-locked Raman pulse pairs,

while the amplitude of the spin beats remains independent of ϕ. Also shown in Figure 6.5,

the spin beats driven by pulse pairs with relative phase -2π , 0, and 2π, present the phase

and amplitude, as is expected.
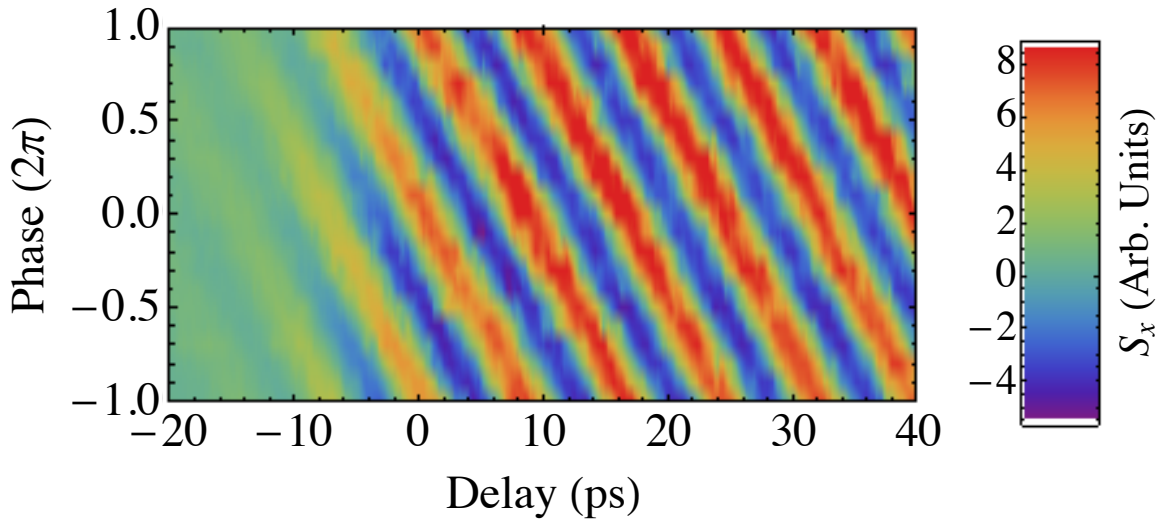
Figure 6.6. Theoretical model of spin coherence induced by spin rotations from phase-locked Raman pulse pairs with relative phase stepped from -2 π to 2 π.

Figure 6.6 shows the result of a theoretical calculation using the optical Bloch

equations for the three-level system without the adiabatic approximation, where

experimentally determined dipole and spin decoherence times, spin splitting, and pulse

duration were used. The experimental results are in excellent agreement with the theory and demonstrate that the phase-locked Raman pulse pair maps the relative optical phase directly onto the phase of the electron spin polarization. This, in essence, is equivalent to an optical spin rotation about an axis in the *x-y* plane in the precessing frame with the axis set by the initial relative phase of the Raman pulse pair.

6.5. *Rabi Oscillations with Raman Pulse Pairs*

Figure 6.7 shows the dynamics of S_x as a function of the average power of the Raman pulse pairs with a fixed initial relative phase of zero and an average detuning of $\Delta=0.75$ nm. The x-projection of the spin polarization is measured, resulting in characteristic spin beats when the net polarization is away from the z-axis. The spin beat amplitude vanishes at ~20 mW control power, which corresponds to a rotation of the spin polarization from –z to +z, a rotation angle of π. For a rotation greater than π, the phase of the spin beats change phase by π but then shift linearly as the pulse power increases from 20 mW to 90 mW.

At a relatively small detuning compared with the linewidth of the trion absorption resonance, the high power of the rotation pulse results in the excitation of excitons and trions. As a result, new spin beats are created and the new carrier population increases the decoherence rate of the electron spins (*51*). The simulation of the electron spin dynamics presented in Figure 6.8 is based on the OBE and does not include manybody effects. Therefore, the theoretical model does not accurately simulate the dynamics of the spins at high pulse power. However, for powers less than 25 mW, when excitation of trions and excitons is relatively small, the theoretical model is in good agreement with the experiment.

Figure 6.7. Spin polarization projected along the x-axis as a function of the delay between the probe and the Raman pulse pair, with increasing average power for the Raman pulse pair with Δ=0.75 nm.
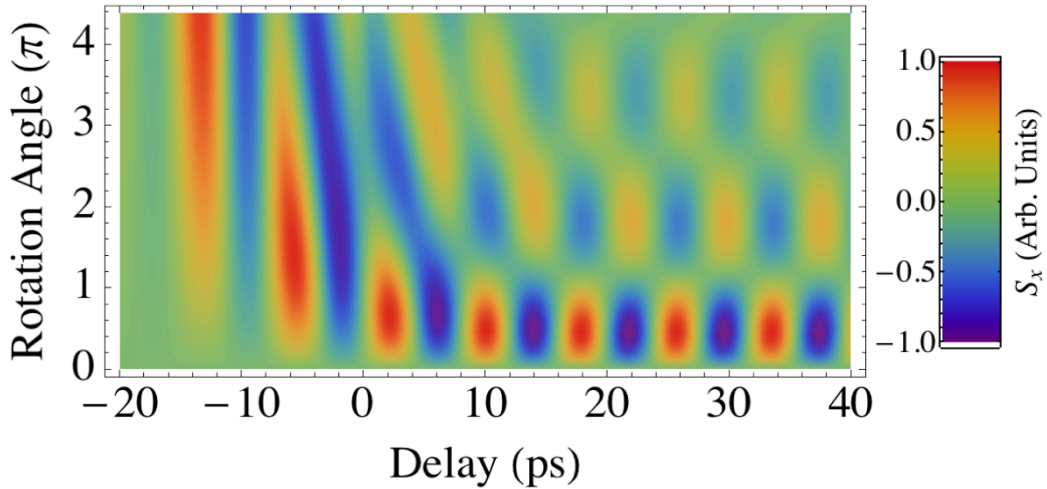
Figure 6.8. Theoretically calculated spin polarization at Δ=0.75 nm detuning, for various pulse areas, given sample parameters.

To avoid exciting populations of excitons and trions we performed experiments with larger detunings. Figure 6.9 shows the dynamics of S_x as a function of the average power of the Raman pulse pairs, obtained at an average detuning of Δ=1.05 nm. The spin beat amplitude vanishes at 35 mW (70 mW) control power, which corresponds to a rotation of the spin polarization from −z to +z (-z), a rotation angle of π (2π). Not only is the coherent transfer of population indicative of coherent Rabi oscillations, so is the phase of

the beats. The π phase difference in the beats shown in Figure 6.9 for the pulses with

power of ~17 mW and ~50 mW, indicates rotations of π/2 and at 3π/2.

Figure 6.9. Spin polarization projected along the *x*-axis as a function of the delay between the probe and the Raman pulse pair, with increasing average power (from 0 to 85 mW) for the Raman pulse pair with Δ=1.05nm.
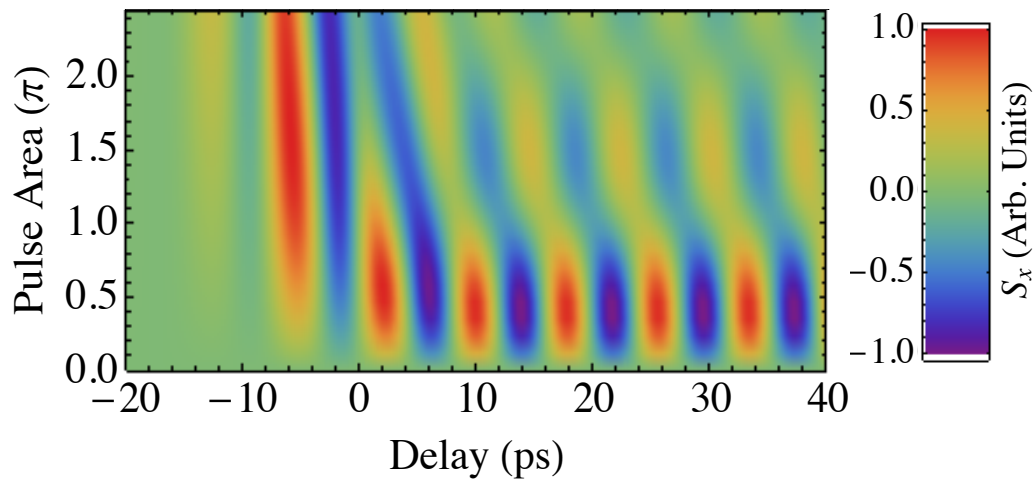
Figure 6.10. Theoretically calculated spin polarization at Δ=1.05 nm detuning, for various pulse areas, given sample parameters.

Several key features of spin rotations at Δ=1.05nm detuning are reproduced in the

numerical simulation shown in Figure 6.10. We observe a π change in the spin beats

between pulses with pulse areas of π/2 and 3π/2 and an overall decrease in the beat

93

amplitude for increased pulse area. However, the spin beats for rotations of π and 2π do not vanish in the theoretical model. In Figure 6.10, near π and 2π, the simulated amplitude of the spin beats decreases while the phase of the beats gradually shifts. The jog in the phase clearly visible at π and 2π in the model is not present in the experimental data and is believed to be obscured by the weak signal resulting from the increased decoherence from coupling to the excited state.
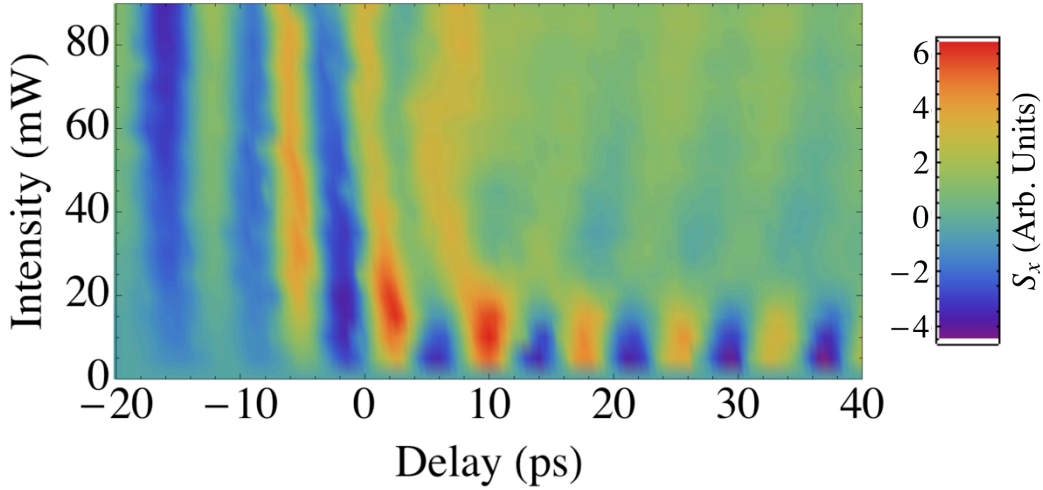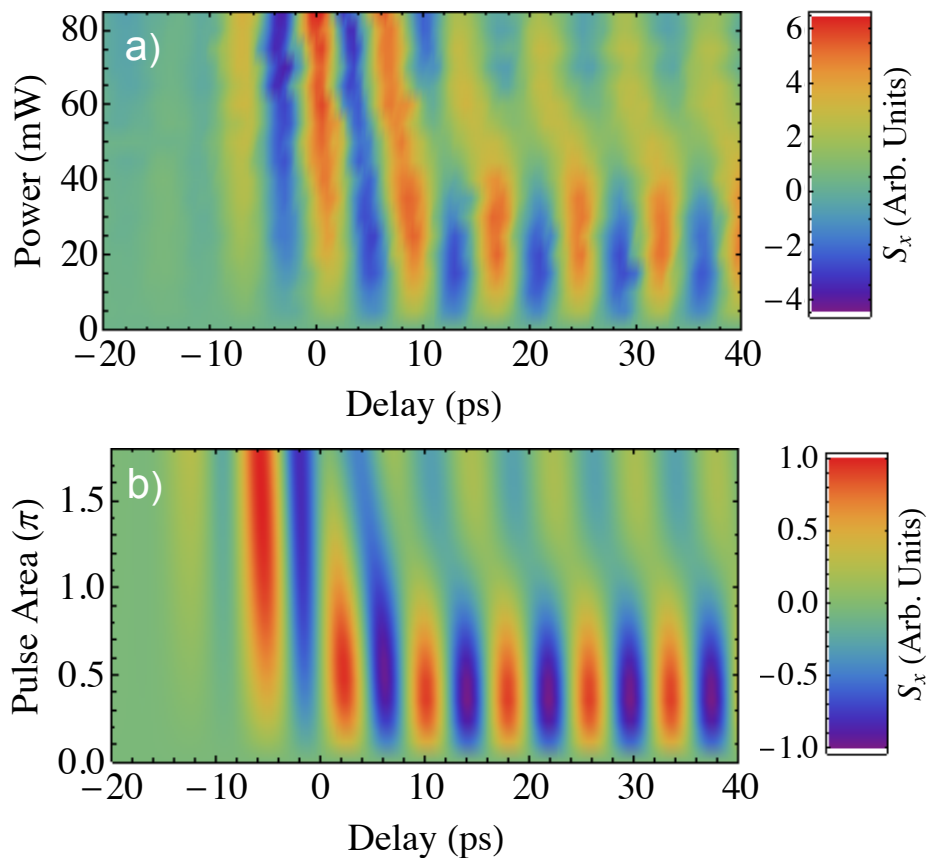

Figure 6.11. (a) Spin polarization projected along the x-axis as a function of the delay between the probe and the Raman pulse pair, with incr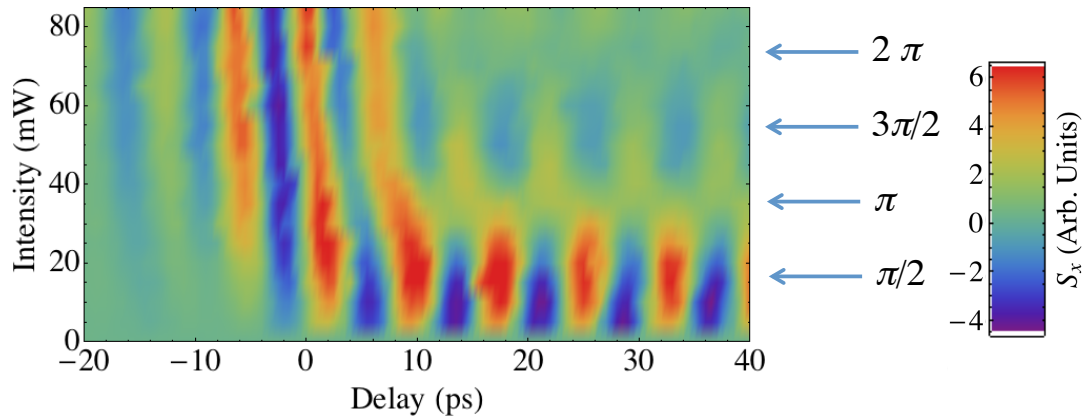easing average power for the Raman pulse pair with Δ=1.7 nm. (b) Theoretically calculated spin polarization as discussed in the text.

At a detuning of 1.7 nm, excitation of excitons and trions is greatly minimized

when compared to detunings of 0.75nm and 1.05nm. Figure 6.11a shows a jog in the phase

at a rotation angle of π, which is clearly reproduced in the theoretical model shown in

Figure 6.11b. The only tunable variable used in the theoretical model of the spin dynamics

presented in Figure 6.8, 6.10 and 6.11b is the detuning. Our model ignores manybody

interactions, and uses a fixed spin decoherence time, while in the experiments, the spin

decoherence time also depends on the level of optical excitation.
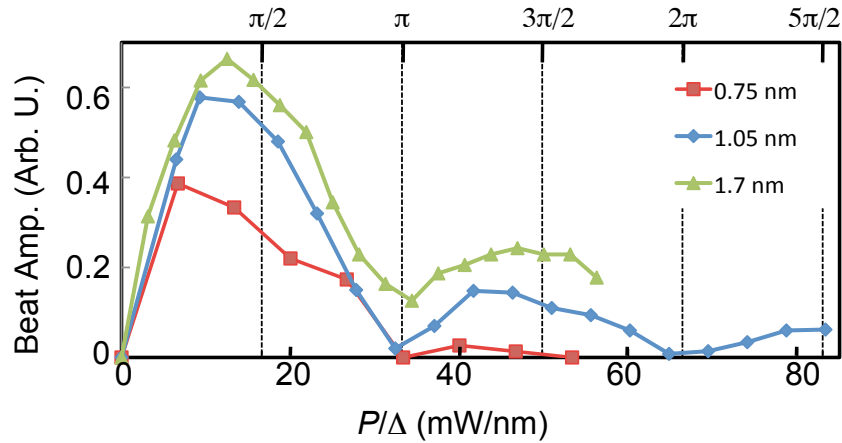
Figure 6.12. Damped Rabi oscillations of electron spins driven by phase-locked Raman pulse pairs. The amplitude of the spin beats for the fourth period as a function of the average power of the Raman pulse pair normalized to the detuning, with the detuning indicated in the figure. The inferred rotation angle is indicated on the top horizontal axis.

Figure 6.12 plots the amplitude of the spin beats after the rotation pulse. The

amplitude of the spin beats is obtained from the fourth period of the spin beats (from the

center of the Raman pulse pair) as a function of the average power obtained at three

different detunings. The power dependence of the beat amplitude shows clearly damped

Rabi oscillations of the electron spins. In Figure 6.12, the average power is normalized to

the detuning, demonstrating that the effective pulse area is inversely proportional to the

detuning, which is consistent with the effective Rabi frequency defined in equation 3.21.

Optical excitations of trions or excitons in a 2DEG can lead to a large increase in the spin

and dipole decoherence rates (*51*). As shown in Figure 6.12, the fidelity of the optical spin rotation deteriorates with increasing optical power, especially when the Raman pulse pair is tuned close to the trion resonance. Nevertheless, with phase-locked Raman pulse pairs, optical spin rotations with a pulse area as large as 2.5π are still clearly observable, as shown in Figure 6.9.

6.5.1. *Contributions from Single Pulse Rotation*

Spin beats that do not go to zero for a pulse area of π (P/Δ=34 mW/nm) are show in Figure 6.11a and reproduced in the theoretical model (Figure 6.11b). These residual beats are a result of the contributions from a single pulse rotation, which act like an effective DC magnetic field. Single pulse contributions can significantly affect the optical spin rotation driven by a Raman pulse pair. Experiments in which the polarization selection rules for the two dipole transitions are orthogonal, a Raman pulse pair with $\theta = \pi$ is expected to rotate the spin polarization from the $-z$ to the $+z$ axis, at which no spin precession would be observed. Figure 6.11a, however, shows prominently that the spin beat amplitude does not vanish; furthermore, the phase of the spin beats varies gradually, instead of flipping by π, as the effective pulse area goes through π. These behaviors are not as prominent in Figure 6.9 due to the degradation in the fidelity of spin rotation at the relatively small detuning. The non-vanishing spin beats and the gradual phase variation of the spin beats near $\theta = \pi$ are a direct result of the effective DC magnetic field, which is induced in a single-pulse spin rotation about the x-axis in the non-precessing frame.

To illustrate the contribution of the single-pulse spin rotation, Figure 6.13 shows the calculated trajectory of a spin Bloch vector due to a Raman-pulse pair with $\theta = \pi$. The

trajectory of the Bloch vector in the right sphere includes both the effective DC and AC fields, as discussed in Chapter III, but does not include effects of spin decoherence. For comparison, the trajectory shown on the left in Figure 6.13 excludes effects of single-pulse spin rotation induced by the effective DC magnetic field.

$$H_{eff} = \frac{\hbar\omega_B}{2}\sigma_z - \hbar\Omega_R \cos(\delta t + \phi)\sigma_x - \frac{\mu^2(E_1^2 + E_2^2)}{4\hbar\Delta}\sigma_x$$
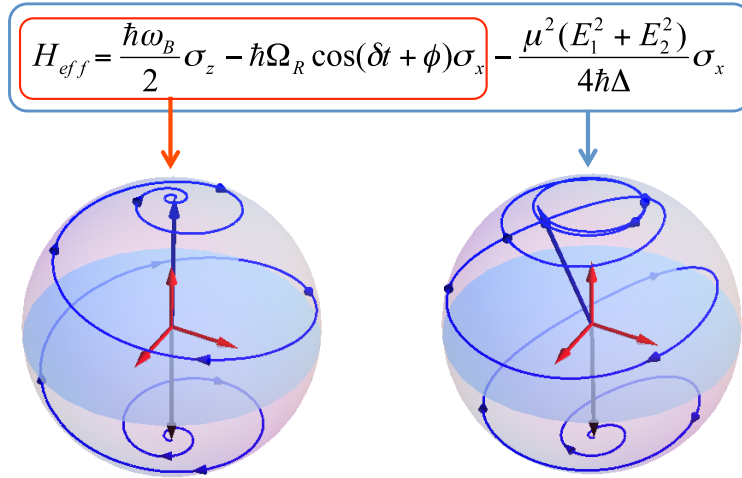
Figure 6.13. Trajectory of a Bloch spin vector initially along the $-z$ axis driven by a Raman pulse pair with $\theta = \pi$ and $\phi = 0$. The trajectory is calculated with the effective two-level Hamiltonian discussed in Chapter III, and is in shown in the figure. Effects of the effective DC magnetic field are included in the Bloch sphere to the right but not in the sphere to the left.

It should be pointed out that the effective DC magnetic field does not lead to decoherence and therefore does not degrade the fidelity of the spin rotation. In the limit that the electron spin splitting far exceeds the spectral width of individual pulses in the pulse pair, as well as the spin decoherence rate, effects of the single-pulse spin rotation become negligible. Also, the effects of single-pulse rotation can, in principle, be compensated with a proper choice of a second set of Raman pulse pairs.

6.6. Pulse Pair Rotations During Spin Precession

A unique signature of a Raman spin-flip is that the flip of precessing spins should

then be symmetric with respect to the arrival time of the Raman spin-flip pulse, as illustrated in Figure 6.11. It is this symmetric spin evolution that leads to the formation of spin echoes. Figure 5.8 shows transient DT responses obtained with a control pulse, with a pulse area of π, at various fixed pump-control delays. For clarity, the DT responses are plotted as a function of the control-probe delay instead of the pump-probe delay. As shown in the figure, the phase of the spin precession is symmetric with respect to the control-probe delay, regardless of the arrival time of the control. This symmetric spin dynamic not only represents a direct and remarkable manifestation of the complete spin flip induced by the control pulse, it also demonstrates the feasibility of using an ultrafast optical pulse for electron spin echoes (*22, 37*).

6.7. Summary

We have successfully demonstrated the quantum control of electron spins in semiconductors with phase-locked Raman pulse pairs. The phase-locked Raman pulse pairs behave effectively like an RF pulse with a phase determined by the relative optical phase. This all-optical spin control takes advantage of well-developed laser technologies, especially optical pulse-shaping techniques, for fast and full quantum control of spins in semiconductors. This technique avoids direct on-chip applications of microwave pulses and provides a nearly ideal and highly versatile approach for universal single-qubit operations in spin-based quantum information processing.

CHAPTER VII

CONCLUSIONS

The spin states of conduction band electrons in direct band gap semiconductors exhibit strong radiative coupling to negatively charged exciton (trion) states, and this radiative coupling makes coherent optical control of spin states possible. This dissertation has presented the experimental demonstration of coherent control of an electron spin ensemble in a two-dimensional electron gas (2DEG), in a CdTe quantum well. We have presented two optical techniques and described the theoretical constraints of both.

The first optical control technique presented used a single off-resonant ultrafast laser pulse. The control pulse was designed to induce an optical Stark shift for the trion resonance and avoid the excitation of excitons. This ultrafast pulse acts like an effective DC magnetic field applied in the propagation direction of the optical pulse. With this pulse, we have successfully realized complete spin flips of electrons in a 2DEG. The spin-flip experiments are well described by a theoretical analysis based on the OBE. The complete spin flip leads to spin precessions that are symmetric with respect to the arrival time of the control, which paved the way for this technique to be used for electron spin echoes (*22, 37*).

The second experiment utilized phase-locked Raman resonant pulse pairs to coherently rotate the electron spin state, where the relative phase of the pulse pair sets the axis of rotation. The Raman pulse pair acts like a RF field driving the spins resonantly. The Raman pulse pair approach enables spin rotation about two orthogonal axes, with

control of pulse area, and relative phase of the pulse pairs, which is essential for arbitrary spin rotation.

Optical spin rotations with phased-locked Raman pulse pairs overcomes inherent limitations of single-pulse optical spin rotations. The single pulse technique only rotates the spins about the optic axis and must rely on other mechanisms for complete control, while full quantum control of electron spins with the Raman pulse pair technique is obtained though the control of the optical field. Also, the effective operation of the single-pulse approach generally requires the use of an ultrafast pulse with a short duration compared with the Larmor precession period. The large spectral bandwidth and peak power of the rotation pulse can lead to undesired excitations and increased decoherence. In contrast, the longer pulses in the Raman pulse pair approach have an overall lower peak power and are spectrally narrow, thus avoiding decoherence associated with the spectrally broad ultra-fast pulses.

The research presented in this dissertation demonstrates two significant contributions to the field of coherent optical interactions with semiconductors. First, through our demonstration of coherent spin flips and complete coherent control we have advanced the potential use of electron spin ensembles in semiconductors for optics based quantum information processing hardware. Second, our work represents the first experimental demonstration of optical spin control with phase-locked Raman pulse pairs. The Raman pulse pair technique overcomes inherent limitations of the single-pulse optical rotation technique, which is the current standard technique used in coherent control.

7.1. Future Work

The immediate continuation of this research involves two separate projects that are related to coherent optical interactions with electron spins exploiting Raman transitions in semiconductors. Work in Hailin Wang's lab at the University of Oregon will seek to improve the fidelity of coherent rotations of electron spins by expanding upon the Raman pulse pair technique. Research at the Naval Research Lab, in partnership with Dan Gammon, will investigate the coherent transfer of a single electron spin state to a photon state in a cavity-coupled quantum dot system.

7.1.1. Chirped Raman Pulse Pairs

In Hailin Wang's lab, we plan to increase the fidelity of electron spin control by exploiting advanced pulse-shaping techniques. To improve the fidelity we plan to generate a pair of Raman resonant pulses that are much longer than were experimentally feasible in prior studies, where longer pulses increase the effectiveness of the rotation pulse, as shown in Figure 3.9. We also plan to exploit further detunings, which will decrease the excitation of trions and excitons. To fulfill the requirements of long pulses and large detuning, we plan to generate a pair of chirped phase-locked pulses.

By chirping a pulse we can make arbitrarily long pulses with out any loss of power, which is in stark contrast to the pulse-shaping technique used in our prior work. In the phase-locked Raman pulse pair experiments, the design of temporally long pulses resulted in decreased pulse power. Using chirped pulses, we should be able to generate temporally long control pulses without loss in power. With greater power we can move to greater detunings, thus limiting the excitation of excitons and trions.

Figure 7.1 diagrams two identical linearly chirped pulses. The intensity of the pulses is plotted against time and frequency, and both exhibit a linear chirp of $\Delta\omega/\Delta t$. At any given moment in time the chirped pulses show a narrow spectral bandwidth, while the time integrated spectral bandwidth of the pulse is broad.
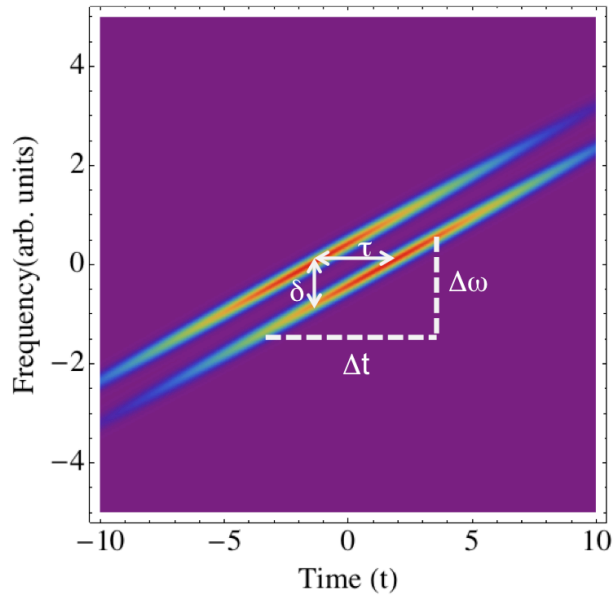
Figure 7.1. A computer generated plot of two identical chirped Gaussian pulses that delayed relative to one another. The two pulses with a linear chirp $\Delta\omega/\Delta t$ delayed by a time τ resulting in a relative frequency difference of δ.

The frequency difference of the two linearly chirped pulses, delayed in time by τ, can be Raman-resonant with the ground state of a Λ-type system. That is, if the frequency difference of the chirped pulses,

$\delta = \tau(\Delta\omega/\Delta t)$,

matches the energy splitting of the ground state. As this pulse pair propagates through a sample, the relative frequency difference of the pair remains constant, even as the instantaneous frequency of each pulse shifts by $\Delta\omega/\Delta t$.

In order to meet the Raman-resonance condition, the spectral bandwidth of the laser

pulse must exceed the energy splitting of the two ground states of interest. This condition is met in our system where the Zeeman splitting for the electrons in CdTe in a magnetic field of 5T is ~0.5meV, and the bandwidth of the 2 ps laser is ~1 meV. The chirped pulse technique will allow for large detuning and long pulses, resulting in further decoupling from the trion state and the minimization of single pulse effects present in temporally short Raman pulses. Therefore, this technique should result in an increased fidelity for rotations in the 2DEG system.

7.1.2. Solid-State Light-Matter Quantum Interface

Proposed research activities at the Naval Research Lab involve the exploitation of a stimulated Raman transition to development a solid-state light-matter quantum interface that should coherently and reversibly map quantum information between light and matter. We plan to develop a waveguide-coupled, photonic crystal optical resonator with an embedded, charged Indium Arsenide (InAs) quantum dot. Coherent operations resulting in a change of the electron spin trapped in the quantum dot should result in a single photon emitted into the cavity.

The Λ-type system investigated in this dissertation is nearly identical to what has been observed for a single electron trapped within an InAs quantum dot. In the Voigt configuration, the two ground states radiatively couple to a common excited state, forming a Λ-type system. We plan to drive a spin-flip Raman transition with two fields: one field defined by a laser with specific bandwidth and center frequency, and a second field defined by the vacuum field of a photonic crystal cavity. Figure 7.2 schematically steps through how this device should work. A laser at frequency $\omega_{initialize}$ pumps the spin into the state

103

$|\uparrow\rangle$, at which point a laser pulse and the cavity field will drive the spin-flip transition. The laser pulse is labeled ω_{pump}, and the vacuum field is labeled ω_{cavity}. The resultant flip of the spin correlates with the scattering of a photon into the cavity mode, thus resulting in the coherent transfer of a matter state (the spin) to a photon state.
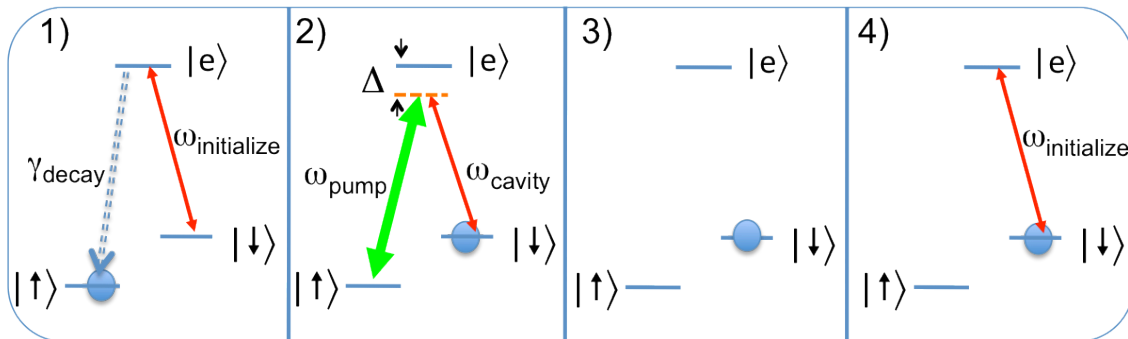
Figure 7.2. Optical pumping scheme in steps. Step 1) Spin polarization by optical pumping. Step 2) Drive the Raman transition with a pump field and the vacuum field of the cavity. Step 3) The population after adiabatic passage is now in the spin down state. Step 4) Reinitialize the state by the optical pumping.

The demonstration of coherent transfer of quantum information from a matter state to a photon state by generating a single photon as a result of a cavity assisted spin flip will be an important milestone on the road to a solid-state quantum network. The success of this work could open the door to experimental studies of entanglement between light and matter. Since the photon emitted into the cavity is primarily determined by the optical cavity, which can be controlled, this will allow for the establishment of entanglement between distant matter qubits by single photons paving the way to a scalable quantum network.

APPENDIX

MATHEMATICA CODE

```
ClearAll
ClearAll

ClearAll[H, G, Δ, ρgg, ρ, Γρ, ω, a, b, c, d, e, f, g1, g2, h, i, j, k, Ω, t, efield]


Y = {{1/√2 , 1/√2 , 0}, {1/√2 , -1/√2 , 0}, {0, 0, 1}};

Hf := I {{0, 0,   (Ωa[t] ) / 2},
        { 0, 0, Ωb[t] / 2},
        {Conjugate[Ωa[t]] / 2, Conjugate[Ωb[t]] / 2,  0 }};
Ha := I {{wb / 2, 0 ,  0},
        { 0, -wb / 2,  0},
        { 0,   0,  Δ }};
H := Ha + Hf;


Γρ := {{G / 2 ρgg[t], -g2 ρud[t], -g1 ρug[t]},
      {-g2 ρdu[t], G / 2 ρgg[t], -g1 ρdg[t]},
      {-g1 ρgu[t], -g1 ρgd[t], -G ρgg[t]}};

ρ := {{ρuu[t], ρud[t], ρug[t]},
      {ρdu[t], ρdd[t], ρdg[t]},
      {ρgu[t], ρgd[t], ρgg[t]}};

Dtρ := ∂_t ρ

Δ := (1.5) 4 wb; (*nm detuning*)
per = 1;
A := per 2 π Δ / 1.2231404787462234`;

NormO[c_] := .5 (e^(-1/4 c² δ²-i φ) (1 + 2 e^(c² δ²/4 +i φ) + e^(2 i φ)))

Ωa[t_] := 1/√NormO[c] √(A / (c √2)) Exp[-(t)²/(2 c²)] (Exp[-i δ t / 2 - i φ/2] + Exp[i δ t / 2 + i φ/2]);
Ωb[t_] := Ωa[t];
G := 1 / 1000;
g1 := 1 / 1000 ;
g2 := .00001;
eid := .00
wb := 2 π / 7.8;
c := √2 FWHM / 2.355
FWHM = 20;
φ = 0 π ;
```

```
δ = wb;
end = 40;

list5 = Table[0, {i, 1, end}];
list4 = Table[0, {i, 1, end}];
list3 = Table[0, {i, 1, end}];
list2 = Table[0, {i, 1, end}];
list1 = Table[0, {i, 1, end}];
Do[{b = per = 3.5 (i - .999) / (end);
  s = NDSolve[{
     Dtρ[[1, 1]] ⩵ (ρ.H - H.ρ + Γρ)[[1, 1]],
     Dtρ[[1, 2]] ⩵ (ρ.H - H.ρ + Γρ)[[1, 2]],
     Dtρ[[1, 3]] ⩵ (ρ.H - H.ρ + Γρ)[[1, 3]],
     Dtρ[[2, 1]] ⩵ (ρ.H - H.ρ + Γρ)[[2, 1]],
     Dtρ[[2, 2]] ⩵ (ρ.H - H.ρ + Γρ)[[2, 2]],
     Dtρ[[2, 3]] ⩵ (ρ.H - H.ρ + Γρ)[[2, 3]],
     Dtρ[[3, 1]] ⩵ (ρ.H - H.ρ + Γρ)[[3, 1]],
     Dtρ[[3, 2]] ⩵ (ρ.H - H.ρ + Γρ)[[3, 2]],
     Dtρ[[3, 3]] ⩵ (ρ.H - H.ρ + Γρ)[[3, 3]],
     ρuu[-1000] ⩵ 0, ρud[-1000] ⩵ 0, ρug[-1000] ⩵ 0,
     ρdu[-1000] ⩵ 0, ρdd[-1000] ⩵ 1, ρdg[-1000] ⩵ 0,
     ρgu[-1000] ⩵ 0, ρgd[-1000] ⩵ 0, ρgg[-1000] ⩵ 0},
    {ρuu[t], ρud[t], ρug[t],
     ρdu[t], ρdd[t], ρdg[t],
     ρgu[t], ρgd[t], ρgg[t]},
    {t, -1000, 100},
    Method -> {"StiffnessSwitching"}, MaxStepSize → .1, MaxSteps → Infinity],
  list1[[i]] = Table[{t, b, Re[Evaluate[ρ[[1]][[1]] /. s][[1]] /. s[[1]]]}, {t, -20, 40, .2}];
  list2[[i]] = Table[{t, b, Re[Evaluate[ρ[[2]][[2]] /. s][[1]] /. s[[1]]]}, {t, -20, 40, .2}];
  list3[[i]] = Table[{t, b, Re[Evaluate[ρ[[1]][[2]] /. s][[1]] /. s[[1]]]}, {t, -20, 40, .2}];
  list5[[i]] = Table[{t, b, Ωa[t] Conjugate[Ωa[t]] / Ωa[0]^2}, {t, -20, 40, .2}];
  list4[[i]] =
   Table[{t, b, Im[Evaluate[ρ[[1]][[2]] /. s][[1]] /. s[[1]]]}, {t, -20, 40, .2}];},
 {i, 1, end}]
theory1 = Flatten[Table[list1[[i]], {i, 1, end}], 1];
theory2 = Flatten[Table[list2[[i]], {i, 1, end}], 1];
theory3 = Flatten[Table[list3[[i]], {i, 1, end}], 1];
theory4 = Flatten[Table[list4[[i]], {i, 1, end}], 1];
theory5 = Flatten[Table[list5[[i]], {i, 1, end}], 1];

Theory1 = ListDensityPlot[theory5, AspectRatio → 1 / 2, InterpolationOrder → 2,
   FrameLabel → {"Control-Probe Delay (ps)", "Control Intensity (arb.)"},
   ColorFunction → "GrayTones", FrameStyle → Directive[Black, 16]]
Theory2 = ListDensityPlot[theory4, AspectRatio → 1 / 2, InterpolationOrder → 2,
   FrameLabel → {"Control-Probe Delay (ps)", "Control Intensity (arb.)"},
   ColorFunction → "GrayTones", FrameStyle → Directive[Black, 16]]
Theory3 = ListDensityPlot[theory3, AspectRatio → 1 / 2, InterpolationOrder → 2,
   FrameLabel → {"Control-Probe Delay (ps)", "Rotation Angle (π)"},
   ColorFunction → "GrayTones", FrameStyle → Directive[Black, 16]]
```
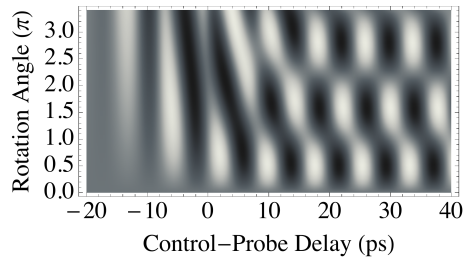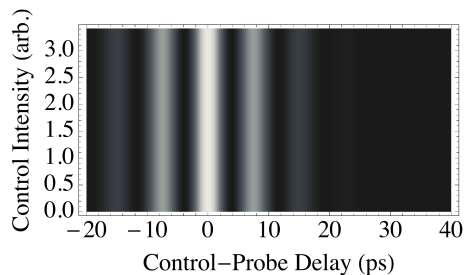
REFERENCES CITED

1. A. Zumbusch, G. R. Holtom, X. S. Xie, Three-Dimensional Vibrational Imaging By Coherent Anti-Stokes Raman Scattering. *Physical Review Letters* **82**, 4142 (May, 1999).

2. C. W. Freudiger *Et Al.*, Label-Free Biomedical Imaging With High Sensitivity By Stimulated Raman Scattering Microscopy. *Science* **322**, 1857 (Dec, 2008).

3. K. Kneipp, H. Kneipp, I. Itzkan, R. R. Dasari, M. S. Feld, Ultrasensitive Chemical Analysis By Raman Spectroscopy. *Chemical Reviews* **99**, 2957 (Oct, 1999).

4. D. J. Gardiner, *Practical Raman Spectroscopy*. P. R. Graves, Ed., (Springer, 1989).

5. S. E. Harris, Electromagnetically Induced Transparency. *Physics Today* **50**, 36 (Jul, 1997).

6. S. E. Harris, Lasers Without Inversion - Interference Of Lifetime-Broadened Resonances. *Physical Review Letters* **62**, 1033 (Feb, 1989).

7. A. Imamoglu, S. E. Harris, Lasers Without Inversion - Interference Of Dressed Lifetime-Broadened States. *Optics Letters* **14**, 1344 (Dec, 1989).

8. J. Oreg, F. T. Hioe, J. H. Eberly, Adiabatic Following In Multilevel Systems. *Physical Review A* **29**, 690 (1984).

9. K. Bergmann, H. Theuer, B. W. Shore, Coherent Population Transfer Among Quantum States Of Atoms And Molecules. *Reviews Of Modern Physics* **70**, 1003 (Jul, 1998).

10. C. V. Raman, A New Type Of Secondary Radiation. *Nature*, 2 (Mar,1928).

11. D. Deutsch, Quantum Computational Networks. *Proceedings Of The Royal Society Of London Series A-Mathematical Physical And Engineering Sciences* **425**, 73 (Sep, 1989).

12. J. I. Cirac, P. Zoller, H. J. Kimble, H. Mabuchi, Quantum State Transfer And Entanglement Distribution Among Distant Nodes In A Quantum Network. *Physical Review Letters* **78**, 3221 (Apr, 1997).

13. L. M. Duan, M. D. Lukin, J. I. Cirac, P. Zoller, Long-Distance Quantum Communication With Atomic Ensembles And Linear Optics. *Nature* **414**, 413 (Nov, 2001).

14. D. P. Divincenzo, The Physical Implementation Of Quantum Computation. *Fortschritte Der Physik-Progress Of Physics* **48**, 771 (2000).

15. S. E. Economou, L. J. Sham, Y. W. Wu, D. G. Steel, Proposal For Optical U(1) Rotations Of Electron Spin Trapped In A Quantum Dot. *Physical Review B* **74**, 205415 (Nov, 2006).

16. P. C. Chen, C. Piermarocchi, L. J. Sham, D. Gammon, D. G. Steel, Theory Of Quantum Optical Control Of A Single Spin In A Quantum Dot. *Physical Review B* **69**, 075320 (Feb, 2004).

17. C. Emary, L. J. Sham, Optically Controlled Single-Qubit Rotations In Self-Assembled Inas Quantum Dots. *Journal Of Physics-Condensed Matter* **19**, 10 (Feb, 2007).

18. C. Langer *Et Al.*, Long-Lived Qubit Memory Using Atomic Ions. *Physical Review Letters* **95**, 060502 (Aug, 2005).

19. A. P. Heberle, W. W. Ruhle, K. Ploog, Quantum Beats Of Electron Larmor Precession In Gaas Wells. *Physical Review Letters* **72**, 3887 (Jun, 1994).

20. J. M. Kikkawa, D. D. Awschalom, Resonant Spin Amplification In N-Type Gaas. *Physical Review Letters* **80**, 4313 (May, 1998).

21. A. Greilich *Et Al.*, Ultrafast Optical Rotations Of Electron Spins In Quantum Dots. *Nature Physics* **5**, 262 (Apr, 2009).

22. D. Press *Et Al.*, Ultrafast Optical Spin Echo In A Single Quantum Dot. *Nature Photonics* **4**, 367 (Jun, 2010).

23. R. Oulton *Et Al.*, Subsecond Spin Relaxation Times In Quantum Dots At Zero Applied Magnetic Field Due To A Strong Electron-Nuclear Interaction. *Physical Review Letters* **98**, 107401 (Mar, 2007).

24. *Semiconductor Spintronics And Quantum Computation*. D. L. D. D. Awschalom, And N. Samarth, Ed., (Springer-Verlag, Berlin, 2002).

25. Y. W. Wu, X. Q. Li, D. Steel, D. Gammon, L. J. Sham, Coherent Optical Control Of Semiconductor Quantum Dots For Quantum Information Processing. *Physica E-Low-Dimensional Systems & Nanostructures* **25**, 242 (Nov, 2004).

26. I. Zutic, J. Fabian, S. D. Sarma, Proposal For All-Electrical Measurement Of T-1 In Semiconductors. *Applied Physics Letters* **82**, 221 (Jan, 2003).

27. D. Loss, D. P. Divincenzo, Quantum Computation With Quantum Dots. *Physical Review A* **57**, 120 (Jan, 1998).

28. M. Zwierz, P. Kok, Applications Of Atomic Ensembles In Distributed Quantum Computing. *International Journal Of Quantum Information* **8**, 181 (Feb-Mar, 2010).

29. H. J. Kimble, The Quantum Internet. *Nature* **453**, 1023 (Jun, 2008).

30. X. D. Xu *Et Al.*, Fast Spin State Initialization In A Singly Charged Inas-Gaas Quantum Dot By Optical Cooling. *Physical Review Letters* **99**, 097401 (Aug, 2007).

31. J. A. Gupta, R. Knobel, N. Samarth, D. D. Awschalom, Ultrafast Manipulation Of Electron Spin Coherence. *Science* **292**, 2458 (Jun, 2001).

32. J. R. Petta *Et Al.*, Coherent Manipulation Of Coupled Electron Spins In Semiconductor Quantum Dots. *Science* **309**, 2180 (Sep, 2005).

33. F. H. L. Koppens *Et Al.*, Driven Coherent Oscillations Of A Single Electron Spin In A Quantum Dot. *Nature* **442**, 766 (Aug, 2006).

34. K. C. Nowack, F. H. L. Koppens, Y. V. Nazarov, L. M. K. Vandersypen, Coherent Control Of A Single Electron Spin With Electric Fields. *Science* **318**, 1430 (Nov, 2007).

35. D. Kielpinski, C. Monroe, D. J. Wineland, Architecture For A Large-Scale Ion-Trap Quantum Computer. *Nature* **417**, 709 (Jun, 2002).

36. D. Press, T. D. Ladd, B. Y. Zhang, Y. Yamamoto, Complete Quantum Control Of A Single Quantum Dot Spin Using Ultrafast Optical Pulses. *Nature* **456**, 218 (Nov, 2008).

37. S. M. Clark *Et Al.*, Ultrafast Optical Spin Echo For Electron Spins In Semiconductors. *Physical Review Letters* **102**, 247601 (Jun, 2009).

38. D. Kim, S. G. Carter, A. Greilich, A. S. Bracker, D. Gammon, Ultrafast Optical Control Of Entanglement Between Two Quantum-Dot Spins. *Nature Physics* **7**, 223 (Mar, 2011).

39. C. Phelps, T. Sweeney, R. T. Cox, H. L. Wang, Ultrafast Coherent Electron Spin Flip In A Modulation-Doped Cdte Quantum Well. *Physical Review Letters* **102**, 237402 (Jun, 2009).

40. B. Kuhnheirich, W. Ossau, T. Litz, A. Waag, G. Landerwehr, Determination Of The Band-Offset In Semimagnetic Cdte Cd1-Xmnxte Quantum-Wells A Comparison Of 2 Methods. *Journal Of Applied Physics* **75**, 8046 (Jun 15 1994, 1994).

41. S. A. Crooker, D. D. Awschalom, J. J. Baumberg, F. Flack, N. Samarth, Optical Spin Resonance And Transverse Spin Relaxation In Magnetic Semiconductor Quantum Wells. *Physical Review B* **56**, 7574 (Sep, 1997).

42. J. G. Tischler, A. S. Bracker, D. Gammon, D. Park, Fine Structure Of Trions And Excitons In Single Gaas Quantum Dots. *Physical Review B* **66**, 081310 (Aug, 2002).

43. R. W. Martin *Et Al.*, 2-Dimensional Spin Confinement In Strained-Layer Quantum-Wells. *Physical Review B* **42**, 9237 (Nov, 1990).

44. E. Blackwood, M. J. Snelling, R. T. Harley, S. R. Andrews, C. T. B. Foxon, Exchange Interaction Of Excitons In Gaas Heterostructures. *Physical Review B* **50**, 14246 (Nov, 1994).

45. M. A. Lampert, Mobile And Immobile Effective-Mass-Particle Complexes In Nonmetallic Solids. *Physical Review Letters* **1**, 450 (Dec, 1958).

46. R. A. Sergeev, R. A. Suris, Ground-State Energy Of X- And X+ Trions In A Two-Dimensional Quantum Well At An Arbitrary Mass Ratio. *Physics Of The Solid State* **43**, 746 (Apr, 2001).

47. R. A. Sergeev, R. A. Suris, G. V. Astakhov, W. Ossau, D. R. Yakovlev, Universal Estimation Of X- Trion Binding Energy In Semiconductor Quantum Wells. *European Physical Journal B* **47**, 541 (Oct, 2005).

48. K. Kheng *Et Al.*, Observation Of Negatively Charged Excitons X- In Semiconductor Quantum-Wells. *Physical Review Letters* **71**, 1752 (Sep, 1993).

49. A. M. Weiner, Femtosecond Pulse Shaping Using Spatial Light Modulators. *Review Of Scientific Instruments* **71**, 1929 (May, 2000).

50. Z. Chen *Et Al.*, Electron Spin Polarization Through Interactions Between Excitons, Trions, And The Two-Dimensional Electron Gas. *Physical Review B* **75**, 115320 (Mar, 2007).

51. E. A. Zhukov *Et Al.*, Spin Coherence Of A Two-Dimensional Electron Gas Induced By Resonant Excitation Of Trions And Excitons In Cdte/(Cd,Mg)Te Quantum Wells. *Physical Review B* **76**, 205310 (Nov, 2007).

52. S. O'Leary, H. L. Wang, Manipulating Nonlinear Optical Responses From Spin-Polarized Electrons In A Two-Dimensional Electron Gas Via Exciton Injection. *Physical Review B* **77**, 165309 (Apr, 2008).

53. S. G. Carter, Z. Chen, S. T. Cundiff, Ultrafast Below-Resonance Raman Rotation Of Electron Spins In Gaas Quantum Wells. *Physical Review B* **76**, 201308 (Nov, 2007).